

ABSTRACT

EAKER, COLLIN BRITTAIN. Electrohydrodynamic Phenomena on a Liquid Metal. (Under the direction of Dr. Michael D. Dickey).

Liquid metals are a class of materials that are being studied for use in a variety of emerging applications, particularly as conductive components in soft robotics and reconfigurable electronics. Historically, a wide array of devices have employed liquid metal mercury; however, the toxicity and large interfacial tension of mercury make it largely impractical as a reconfigurable conductor. Here, we explore the use of gallium and gallium-based alloys, particularly a eutectic mixture of gallium and indium (EGaIn) as liquid metals of choice. These materials have the advantage of being non-toxic and, perhaps most interestingly, develop a passivating surface oxide layer that allows them to remain stable in non-spherical shapes. We focus particularly on several phenomena that result from applying an electrical or electrochemical potential to the metal in contact with an aqueous solution.

First, we review the previous literature regarding the actuation of liquid metals under applied electrical fields. This will primarily examine four major mechanisms that have been used in past studies: electrocapillarity, continuous electrowetting, electrowetting-on-dielectric, and electrochemistry. We give an overview of the advantages and drawbacks of each of these techniques.

We present the effects of anodization and reduction of the EGaIn oxide film in a solution of sodium hydroxide. By controlling the electrochemical potential, we can reversibly and drastically tune the interfacial tension of the liquid metal. This allows for voltage-controlled injection and withdrawal from microfluidic channels, asymmetric dewetting from a substrate, and stable liquid metal fibers.

At excessive oxidative potentials, the liquid metal changes its shape drastically, displaying several characteristic behaviors depending on the time, droplet volume, and magnitude of the potential. Here, we describe the conditions that give rise to this behavior, and the various forces involved. Furthermore, we show that the oxide layer can both stabilize and destabilize the shape, depending on the conditions, and we characterize a new class of fingering instabilities that occur around the perimeter of the metal.

Finally, we show a novel use of the liquid metal as a paint-on electrode for electrowetting-on-dielectric. Most electrowetting systems rely on vacuum deposition of a thin dielectric that requires large voltages for operation and can be ruined upon dielectric breakdown. The electrowetting system that relies on the oxide layer of EGaIn is simple to fabricate, low voltage, compatible with flexible and stretchable substrates, and can self-heal upon dielectric breakdown. Additionally, by utilizing the potential of zero charge offset, we demonstrate electrowetting without an applied external voltage.

© Copyright 2016 Collin Brittain Eaker

All Rights Reserved

Electrohydrodynamic Phenomena on a Liquid Metal

by
Collin Brittain Eaker

A dissertation submitted to the Graduate Faculty of
North Carolina State University
in partial fulfillment of the
requirements for the degree of
Doctor of Philosophy

Chemical Engineering

Raleigh, North Carolina

2016

APPROVED BY:

Dr. Michael Dickey
Committee Chair

Dr. Karen Daniels

Dr. Jan Genzer

Dr. Edmond Bowden

BIOGRAPHY

Collin Brittain Eaker was born in Forest City, North Carolina on December 23, 1987. After graduating from East Rutherford High School in 2006, he entered into the University of South Carolina. He graduated with a Bachelor of Science in Chemical Engineering and a minor in Chemistry in 2010. In the Fall of 2010, he joined the Department of Chemical and Biomolecular Engineering at North Carolina State University as a graduate student, and received a Master of Science in 2012 under the direction of Michael Dickey.

ACKNOWLEDGMENTS

First, I would like to thank the members of my committee: Dr. Michael Dickey, Dr. Jan Genzer, Dr. Karen Daniels, and Dr. Edmond Bowden. All of you have, in one way or another, been a positive influence on my graduate school career. You have been great teachers and mentors, and have set an example to which I aspire.

I am grateful to all of the members of the Dickey Group, past and present, with whom I have had the great pleasure of working; from Sharvil Desai and Rashed Khan, who helped me find my way around the lab as a clueless new graduate student, to those with whom I'm currently collaborating, particularly Dishit Parekh, Ishan Joshipura, and Collin Ladd. I have, at some point, sought advice or guidance from all of the members of our group, and your help has always been appreciated. I also want to thank all of the undergraduates, high school students, and exchange students whom I've had the great pleasure of mentoring.

To my Class of 2010 friends, especially Daniel Morales, Mike Heller, Garrett Wheaton, and Jeff Zurawski: had it not been for your constant distraction, I would likely have graduated years ago! But there wouldn't have been nearly as much fun, not as many laughs, and none of the great memories that I will carry with me for a lifetime. Much the same can be said for my undergraduate friends, and all of the friends that I have made here in Raleigh.

To my family (particularly my parents, David and Ronda Eaker): Thank you all for the years of constant support and encouragement. You've always been there to listen, advise, and occasionally, console. I love you all dearly.

And finally, because once is not enough, I would like to thank Michael Dickey. When I stepped into your office searching for an advisor (and any sort of direction in graduate

school), I was met with boundless enthusiasm and a host of ideas. Since then, I've known that I can always count on you for wisdom and guidance. You've opened the door for opportunities that I would never have imagined, and have shown endless patience for my less admirable study and work habits. You have been a role model, a mentor, and a friend. Thank you.

TABLE OF CONTENTS

LIST OF TABLES	vii
LIST OF FIGURES	viii
Chapter 1	1
Liquid Metal Actuation by Electrical Control of Interfacial Tension.....	1
1.1 Introduction.....	1
1.2 Applications of Liquid Metal.....	3
1.3 Electrocapillarity.....	6
1.4 Continuous Electrowetting.....	10
1.5 Electrowetting-on-dielectric	18
1.6 Electrochemically Controlled Capillarity	25
1.7 Outlook and Conclusions.....	31
1.10 References.....	32
Chapter 2	45
Giant and Switchable Surface Activity of Liquid Metal via Surface Oxidation	45
2.1 Introduction.....	45
2.2 Results.....	46
2.3 Materials and Methods.....	59
2.3.1 Electrochemical Experiments	59
2.3.2 Area Measurements	60
2.3.2 Interfacial Tension Measurements.....	61
2.3.4 Capacitance Measurements.....	62
2.3.5 Reversibility Measurements.....	64
2.3.6 Capillary Length	65
2.4 Acknowledgements.....	66
2.5 References.....	66
Chapter 3	71
Oxide-Mediated Fingering Instabilities in Liquid Metals	71
3.1 Introduction.....	71
3.2 Methods and Materials.....	72
3.3 Results.....	76

3.3.1 Droplet Morphology	76
3.3.2 Spreading and Restoring Forces	81
3.3.3 Oxide Growth and Dissolution	85
3.4 Conclusions.....	90
3.5 References.....	90
Chapter 4	93
Electrowetting Without Applied Potential Using Paint-on Electrodes.....	93
4.1 Introduction.....	93
4.2 Results.....	96
4.3 Conclusions.....	105
4.4 Methods and Materials.....	105
4.5 References.....	108
Conclusions and Outlook	111

LIST OF TABLES

Table 1.1: Comparison of liquid metal actuation techniques.....	30
--	----

LIST OF FIGURES

- Figure 1.1:** Summary of primary methods for liquid metal actuation. a) Electrocapillarity utilizes charges in the electrical double layer to realize modest changes in surface tension. b) Continuous electrowetting creates surface tension gradients to actuate liquid metal within channels. c) Electrowetting-on-dielectric uses large voltages to achieve modest changes in wetting behavior on a substrate. d) Electrochemically controlled capillarity utilizes interfacial reactions to achieve enormous changes in surface tension. 3
- Figure 1.2:** Emerging applications for liquid metals. a) Ultra-stretchable wire made by injecting liquid metal into a hollow elastomeric fiber²⁶. Copyright John Wiley and Sons. b) Liquid metal stretchable RFID tag placed on skin⁴¹. Reproduced with permission from the Royal Society of Chemistry. c) A nitrile glove functionalized by inkjet-printed liquid metal nanoparticles²⁷. Copyright John Wiley and Sons. d) LED integrated into a stretchable polymer with liquid metal interconnects²⁴. Reprinted with permission from AIP Publishing. e) Liquid metal RF sensor under strain³⁵. Reproduced with permission from the Royal Society of Chemistry..... 5
- Figure 1.3:** Electrocapillary behavior of liquid metals in electrolyte. a) Electrocapillary curve showing the surface tension of a liquid metal drop as a function of voltage. The apex of the curve represents the potential of zero charge; any change in voltage, whether positive or negative, results in a decrease in interfacial tension and a relative flattening of the drop due to gravity. The lowered interfacial tension is caused by the capacitance at the electrical double layer. Data reproduced from Frumkin et. al⁵⁵, with permission from Elsevier. b-c) The lowering of interfacial tension by electrocapillarity can induce the capillary rise of the metal through a small tube. 8

Figure 1.4:	Mercury confined to a 500 μm wide microfluidic channel ⁶⁶ . Electrodes are present on both ends of the microchannel. a) In the absence of an applied voltage, the mercury plug remains stable in the channel. b) An applied potential between the electrodes causes actuation of the metal plug.	11
Figure 1.5:	Devices based on continuous electrowetting. a) Simulation and experimental results of a plug of liquid metal moving to the right by continuous electrowetting (electrodes not shown) ⁷¹ . b) Schematic for a micromotor based on continuous electrowetting of a slug of Hg ⁶⁶ . c) Liquid metal micromotor. 14 μm ‘filters’ connect the main track to the electrode while preventing the liquid metal from exiting.	14
Figure 1.6:	Continuous electrowetting of liquid metal marbles in an open solution ⁷² . a) Force balance of the Galinstan drop in a solution of NaOH. The surface tension gradient overcomes the viscous drag and substrate friction to drive movement of the drop. b) Time lapse of a Galinstan marble traversing between electrodes. Reproduced with permission from the Royal Society of Chemistry.	16
Figure 1.7:	a) Design of a liquid metal pump in an open channel ⁷⁴ . b) Galinstan drop in confined channel. Polarity of graphite electrodes drives liquid metal in one direction, inducing electrolyte flow in the opposite direction. c) Time lapse of the dyed solution pumped completely through the channel. Copyright PNAS.	17
Figure 1.8:	Electrowetting-on-dielectric ⁷⁷ . a) A conductive electrode is coated with a thin dielectric and hydrophobic coating, with a water droplet placed on top. The water reaches an equilibrium contact angle. b) A voltage is applied between the electrode and the droplet, causing charges to migrate to the interface and thereby decrease the effective contact angle. Reproduced with permission from the Royal Society of Chemistry.	20

Figure 1.9:	Electrowetting curve of a mercury drop. At larger voltages, the contact angle begins to saturate and deviate from the theoretical curve. Dielectric layer is a 600 nm parylene film ⁸⁸ . Reproduced with permission from ASME.	22
Figure 1.10:	A liquid metal-based MEMS switch ⁹⁸ . a) A mercury droplet on an EWOD substrate for switching. b) The liquid metal droplet was placed in a microframe to ensure accurate positioning.	23
Figure 1.11:	Electrochemically driven spreading of gallium-based alloys. a) A drop of liquid gallium sits on a conductor over a backlight. b) Applying a voltage to the drop causes spreading that blocks the back light ¹⁰⁴ . Reprinted with permission of AIP Publishing. c) A drop of liquid metal being oxidized at 2 V in 1 M NaOH. d) Surface tension of a eutectic gallium indium drop in 1 M NaOH. The vertical dotted line represents formation of the oxide layer ¹⁰⁵ . Copyright PNAS.	26
Figure 1.12:	Electrochemical injection (ECC) and withdrawal (recapillarity) of a liquid metal. a) Galinstan is injected into a NaOH-filled microchannel by ECC (interfacial oxidation) ¹⁰⁶ . b) Reduction of the oxide layer at the interface of the channel creates an increase in the liquid metal surface tension, causing rapid withdrawal. c) The same mechanism allows the liquid metal to withdraw from the shortest path of a maze ¹⁰⁷ . Copyright John Wiley and Sons.	29
Figure 2.1:	Spreading enabled by a surface oxide. (A) Oxidative spreading of a bead of liquid metal in 1M NaOH solution. A needle serves as a top electrical contact to the droplet in the left column, whereas a wire serves as a bottom electrical contact to the droplet in the right column. (i) The drop assumes a spherical shape initially due to its large surface tension; (ii) upon application of an oxidative potential, the metal assumes a new equilibrium shape; (iii) above a critical potential, the metal flattens and spreads without bound and ultimately forms	

fingering patterns that further increase its surface area and destabilize the metal; (B-D) The unshaded region denotes oxidative potentials; (B) The areal footprint of a drop of EGaIn as a function of time and potential identifies the critical potential above which spreading occurs without bound (solid circles) and below which the droplet adopts equilibrium shapes (hashed symbols). (C) An electrocapillary curve of EGaIn measured by sessile drop profile in 1 M NaOH; (D) A cyclic voltammogram of EGaIn. (E) The measured capacitance and calculated capacitive energy of EGaIn from impedance spectroscopy. 47

Figure 2.2: The interfacial tension of the metal may be tuned dramatically, rapidly, and reversibly in response to small changes in potential, as shown using multi-step chronoamperometry of a sessile EGaIn drop in 1 M NaOH. Increasing the electrochemical potential results in a corresponding decrease of the interfacial tension, consistent with the values in Figure 2.1C. 51

Figure 2.3: (A) Inducing liquid metal into an upward-tilted capillary channel (~0.9 mm ID) by application of a voltage in the presence of 1 M NaOH; (B) Controlling the shape and direction of a metal drop into an open T-shaped Plexiglas® channel submerged in 1 M NaOH solution using only voltage. Switching the position of the counter electrode at different points (ii-iv), guides the direction of the metal droplet; (C) Side view of a small droplet of EGaIn pumped out of a 0.5 mm ID polymer tube at 20 mL/hr in 1 M NaOH. The metal forms droplets in the absence of potential; (D) Formation of an oxide coated liquid metal fiber coming out of the tube at 5 V. 54

Figure 2.4: ‘Recapillarity’ can manipulate the shape and local contact angle of droplets placed on dry substrates. (A) Electrochemical reduction of the oxide on a droplet of liquid metal supported by a glass slide causes the metal to bead up. Removal of the electrode prior to imaging creates

the lobe on the top of the drop; (B) Three sequential side views (i-iii) of an EGaIn drop that asymmetrically dewets a glass slide in DI water upon application of reductive potentials relative to a counter electrode placed on the right side of the drop. Recapillarity causes the metal to move away from the anode, which is outside the frame of the image. The cathode gently touches the top of the drop to minimize perturbation of the shape of the metal..... 56

Figure 2.5: Recapillarity-induced withdrawal of liquid metal from microchannels. (A) The electrochemical reduction of gallium oxide in pH-neutral electrolyte induces retreat of the metal from the channel by applying a reductive potential; (B) Top-down photograph of a T-shaped microfluidic channel. (1 mm wide, 100 μm tall, 65 mm long horizontally) The surface oxide stabilizes the liquid metal in the channel; (C) A reductive bias (-1 V) applied to the metal relative to a drop of electrolyte (0.01 M NaF) at the anode removes the oxide and the liquid metal retreats toward the cathode; (D) The metal continues to withdraw until the applied voltage ceases. Metal that is not in the electrical pathway remains stable. 58

Figure 2.6: (A) Photograph of the bottom of a drop of EGaIn taken before applying a potential; (B) Photograph of the bottom of the same drop of EGaIn several seconds after applying 900 mV relative to the open circuit potential; (C-D), ImageJ outlines of the EGaIn drop used to estimate the area..... 61

Figure 2.7: Schematic depicting the acrylic sheet used to secure a copper wire. (A) A 1 mm diameter hole was cut in the acrylic using a Universal VLS3.50 laser cutter. An insulated copper wire was secured using a photocurable resin; (B) Drops of EGaIn were placed on top of the hole with the wire extended $\approx 100 \mu\text{m}$ beyond the plane of the surface to avoid distorting the shape of the drop..... 62

Figure 2.8:	(A) Nyquist plot of EGaln drop at -1.2 V vs. Ag/AgCl and (B) -1.9 V vs. Ag/AgCl.	64
Figure 3.1:	(a) Schematic of apparatus, and experimental images showing evaluation of fingering instability of liquid metal. (b) Box-counting plot for a 30 μL droplet of EGaln spreading with -0.2 V vs Ag/AgCl applied potential (shown in (a)). (c) Box-counting plot of droplets with $V = 10 \mu\text{L}$, 30 μL , and 100 μL , analyzed immediately before first branch break-off.....	75
Figure 3.2:	(a) Representative images taken at the maximum area for all four regimes, and their dynamics characterized by (b) area $A(t)$ and (c) the electrical resistance measured from from $(\varepsilon + 1.5 \text{ V})/I(t)$. The star indicates the time at maximum area. All panels show data from the same 4 trials with $V = 30 \mu\text{L}$ and $\varepsilon = -0.7 \text{ V}$ (regime A); $\varepsilon = 0.3 \text{ V}$ (regime B); $\varepsilon = 1.3 \text{ V}$ (regime C); $\varepsilon = 2.5 \text{ V}$. All potentials relative to a Ag/AgCl reference electrode.....	79
Figure 3.3:	Phase diagrams for droplets of volume V subject to an applied electric potential ε . The solid black line corresponds to the peak \tilde{A} in Figure 3.4. The inset represents the potential ε_{max} at which the maximum in Figure 3.4a occurs, as a function of droplet volume (on a logarithmic scale). Error bars represent the width ε_w of Figure 3.4a at half \tilde{A}_{max}	80
Figure 3.4:	(a) Scaled area \tilde{A} as a function of applied electric potential ε . (b) The data from (a) with a rescaled horizontal axis to show similarity of results, with $(\varepsilon_{\text{max}}, \varepsilon_w)$ measured from (a) for each droplet volume.....	81
Figure 3.5:	Average center of mass displacement created by tilting the apparatus in Figure 3.1a. 2.5 volts were applied to a 30 μL droplet with no reference electrode present in the system.	83
Figure 3.6:	Oxide growth during anodic oxidation. a) Modeled growth rate of the oxide layer, estimated from the measured surface area and current profile of a 30 μL droplet at -0.2 V, 0.3 V, and 1 V. b) Modeled average	

	oxide thickness under the same conditions. c) Steady-state growth rate and maximum oxide thickness.....	89
Figure 4.1:	Preparation of the ‘paint on’ liquid metal electrodes for low-voltage electrowetting. (a,b,c) 100 μ L drop of EGaIn is placed on a glass substrate and spread as a film across the surface. (d,e) A DI H ₂ O/1 wt% SDS drop is submerged in dodecane/0.2 wt% sorbitan trioleate solution and voltage is applied across a top electrode (a stainless steel dispensing needle) and the EGaIn layer. (f) DC electrowetting curve of DI H ₂ O and H ₂ O/1 wt% SDS, including theoretical curves. Error bars represent s.d.....	97
Figure 4.2:	Electrowetting on a stretchable substrate. (a) AC electrowetting curve on EGaIn, with both no strain and 100% strain of the underlying substrate. (b) Minimum reversible contact angle achieved (7°) with AC electrowetting at -800 mV RMS applied. (c) Photographs of i) EGaIn film on a substrate made of silicone elastomer. ii) Liquid metal conforms to the elastomer and elongates when the substrate is stretched.	99
Figure 4.3:	Electrowetting on metal with various fabrication techniques. a) “Painted” EGaIn film that was brushed roughly across substrate. b) Solid gallium film prepared by spreading liquid Ga with a slot-die and then frozen. c) Electrowetting curve that shows similar behavior between these films and “pristine” liquid metal surface.....	101
Figure 4.4:	Wetting of a droplet on EGaIn without externally applied potentials. (a) At open circuit, the droplet maintains a large contact angle with the substrate. (b) When the circuit is closed, the drop rapidly (and reversibly) wets the substrate due to the offset from the V_{pzc}	103
Figure 4.5:	The point of zero charge varies with materials of construction. (a) Electrowetting curve of DI water with platinum, stainless steel, copper, gallium, and EGaIn top electrodes. EGaIn film serves as the	

substrate electrode for electrowetting. (b) Linear sweep voltammogram of two-electrode system at 1 mV/s. (c) Electrowetting curve of DI water with varied top electrodes and Ag/AgCl reference electrode. (d) Linear sweep voltammogram of three-electrode system at 1 mV/s. 104

Chapter 1

Liquid Metal Actuation by Electrical Control of Interfacial Tension

1.1 Introduction

Liquid metals combine uniquely the low viscosity of liquids with the desirable properties of metals (e.g., high thermal and electrical conductivity), making them suitable for use in soft, stretchable devices such as soft robotics^{1,2}, e-skin³, wearables⁴, and stretchable electronics⁵. Furthermore, they can be patterned at room temperature in unique ways⁶ and incorporate readily into microfluidic networks as pumps, electrodes, and valves. Perhaps the most promising and distinct property of liquid metals is their ability to be reversibly shape-reconfigured at room temperature; this opens up the possibility for devices that can change their function based on the switchable shape or position of their liquid metal components. This review focuses on methods to control the shape, position, and flow of liquid metals by manipulating interfacial tension utilizing voltage.

There are five known metallic elements that are in the liquid state at or near room temperature: francium, cesium, rubidium, mercury, and gallium. However, francium and cesium are radioactive, while rubidium is explosively reactive when contacted with air, rendering these materials unsuitable for practical applications. Mercury, on the other hand, has been used in a wide variety of applications such as measurement equipment (e.g. barometers, thermometers), lamps, diffusion pumps, dental amalgams, and as the working electrode in its own field of electrochemistry (polarography). In spite of its long history of use, mercury is limited by its toxicity to humans⁷. A safer alternative to mercury is gallium⁸. Although gallium

itself melts just above room temperature (30 °C), it can be combined with various other metals (e.g. indium and tin) to form alloys that will melt at lower temperatures⁹. Unlike mercury, gallium also forms spontaneously a thin (1-3 nm)¹⁰, passivating oxide layer on its surface. This oxide layer has traditionally restricted the use of gallium; the formation of the oxide complicates its use as an electrode in electrochemical experiments¹¹, and its tendency to stick to many surfaces makes it difficult to actuate droplets¹². The oxide, however, does provide gallium with many unique advantages. Although the interfacial tension of liquid metals is very large (> 400 mN/m)¹³, the oxide skin allows the liquid metal to maintain shapes that are otherwise prohibited by surface tension¹⁴. This property enables simple methods of patterning gallium^{6,15-18}; it also allows gallium to remain stable after injection into microfluidic channels, providing an effective means of incorporating these metals into soft devices¹⁴.

This review focuses on ways to move and manipulate liquid metals into new shapes and positions using voltage. In regard to the organization, content, and focus, we offer four clarifying comments. First, we focus primarily on gallium and its alloys. However, we also include mercury—despite its toxicity—in this review because it has been utilized in numerous applications and it offers a way of introducing several phenomena without the complications associated with the oxide layer that forms on gallium and its alloys. Second, we limit discussion primarily to methods to manipulate interfacial tension because these forces dominate on sub-mm length scales. Third, we focus primarily on methods that offer reversible actuation such that the metal can cycle back to its original shape or position (e.g., conventional surfactants can lower interfacial tension, but not in a way that is useful for actuation). Fourth, we recognize

mechanical manipulation (e.g., pumping, physical prodding) as a method for moving metals, but choose to focus on voltage-driven phenomena.

Voltage-driven actuation has the appeal of being easy to implement, control, and miniaturize. It does not require bulky pumps, nor does it necessarily require direct contact with the liquid metal. We review electrocapillarity, electrowetting, continuous electrowetting, and electrochemistry as methods to move and manipulate liquid metals (as summarized in **Figure 1.1**). We detail the underlying physical mechanisms of these techniques, the ways in which they have been used, and their advantages and challenges after first briefly motivating applications of liquid metals.

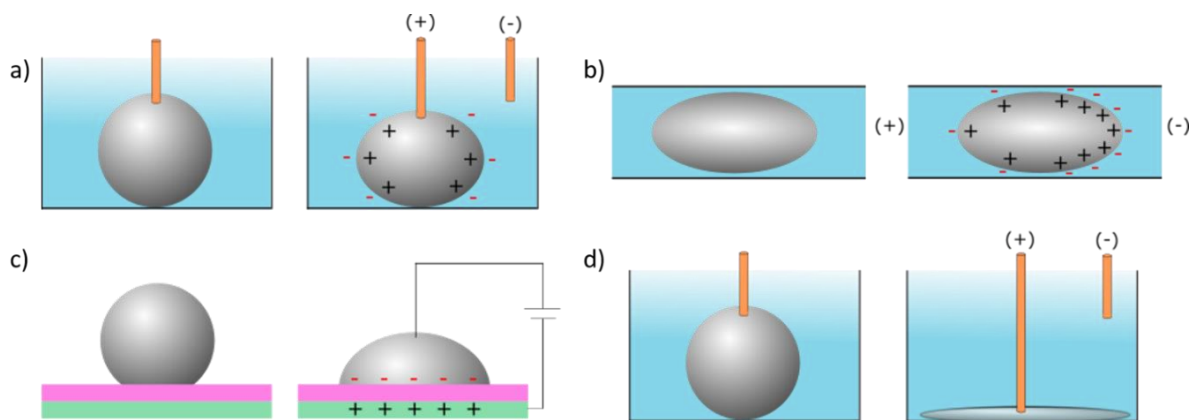


Figure 1.1: Summary of primary methods for liquid metal actuation. a) Electrocapillarity utilizes charges in the electrical double layer to realize modest changes in surface tension. b) Continuous electrowetting creates surface tension gradients to actuate liquid metal within channels. c) Electrowetting-on-dielectric uses large voltages to achieve modest changes in wetting behavior on a substrate. d) Electrochemically controlled capillarity utilizes interfacial reactions to achieve enormous changes in surface tension.

1.2 Applications of Liquid Metal

In addition to the aforementioned historical applications of mercury, liquid metals are being investigated for use in a variety of other technologies¹⁹. These applications help motivate

the use of voltage to manipulate the shape and position of liquid metals.

Many of the recent advances in liquid metals have been enabled by microfluidics, a field designed to study and manipulate fluids at sub-mm length scales. Microfluidic channels can be easily fabricated (e.g. through soft lithography^{20,21}) from a wide variety of materials. The low viscosity of liquid metals allows them to be injected into these microchannels at relatively low pressures and temperatures. While mercury adopts shapes in microchannels that minimize surface energy (including spontaneous withdrawal), the surface oxide allows gallium to remain stable within microchannels after injection¹⁴. This property offers many key benefits.

Unlike their solid counterparts, liquid metals are able to withstand significant bending, stretching, and deformation of the polymer in which they are embedded, without significant loss of electrical conductivity. This feature has been utilized to create stretchable circuitry and interconnects for artificial skin^{22,23}, stretchable conductors²⁴⁻²⁷, inherently aligned microfluidic electrodes²⁸, compliant MEMS components^{29,30}, microfluidic heat sinks³¹, and antennas³²⁻⁴⁰ (**Figure 1.2**).

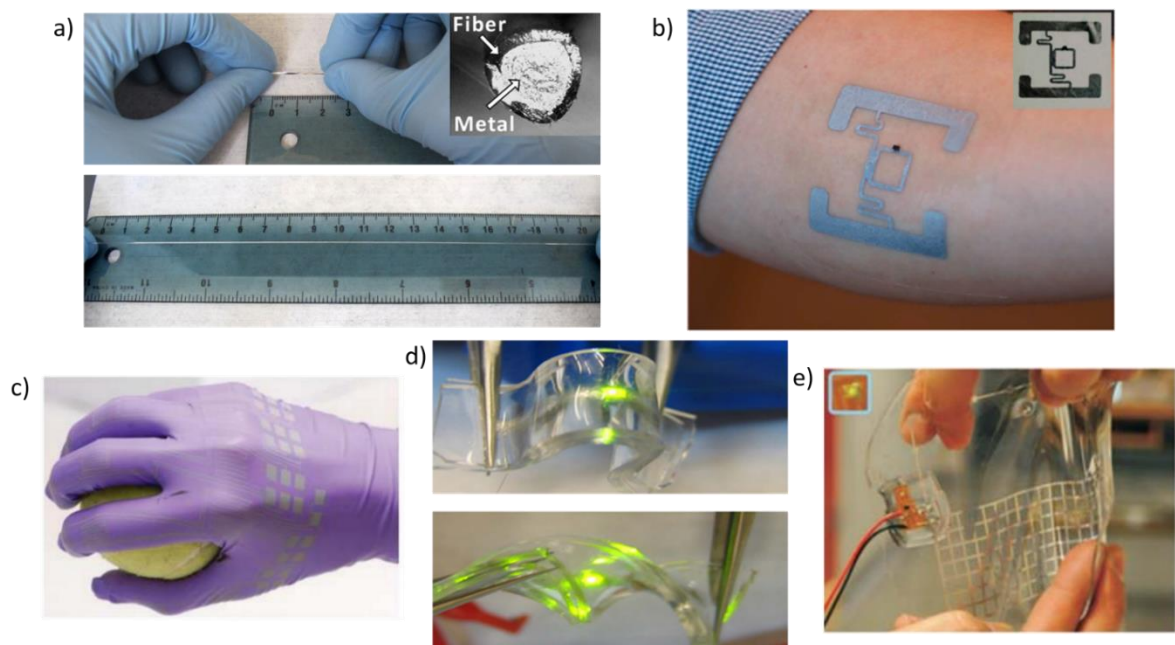


Figure 1.2: Emerging applications for liquid metals. a) Ultra-stretchable wire made by injecting liquid metal into a hollow elastomeric fiber²⁶. Copyright John Wiley and Sons. b) Liquid metal stretchable RFID tag placed on skin⁴¹. Reproduced with permission from the Royal Society of Chemistry. c) A nitrile glove functionalized by inkjet-printed liquid metal nanoparticles²⁷. Copyright John Wiley and Sons. d) LED integrated into a stretchable polymer with liquid metal interconnects²⁴. Reprinted with permission from AIP Publishing. e) Liquid metal RF sensor under strain³⁵. Reproduced with permission from the Royal Society of Chemistry.

Liquid metals offer the unique opportunity for creating shape reconfigurable conductors for reconfigurable circuits, switches, antennas, and optofluidic devices. Antennas are a particularly compelling application of liquid metals because the spectral properties (frequency, bandwidth, etc.) depend on the shape of the conductors that comprise them. Thus, the ability to change the shape of liquid metals offers the opportunity to create reconfigurable antennas. Liquid metal antennas that change shape (and thus, function) via external stretching have been demonstrated^{33,36,42}, but mechanical tuning of antennas offers limited utility due to the reliance on mechanical mechanisms.

An array of techniques have been developed to actuate liquid metals in-situ, but none of these techniques are without drawbacks. Pneumatic pressure has been used previously to dynamically move liquid metals, both to eject liquid metal droplets onto surfaces^{16,43,44} and to inject them into microfluidic channels⁴⁵. However, pneumatic pressure requires bulky and rigid mechanical components. Furthermore, microfluidic injection of gallium and its alloys is effectively irreversible; while the pneumatic pressure can be reversed, the oxide layer tends to stick to the walls and leave behind a residue⁴⁶, though the use of acids or fluid slip layers helps prevent this issue^{40,46-48}. Chemical driving forces have also successfully moved liquid metal drops, but these sources are quickly exhausted^{49,50}. Though some recent work has focused on electromagnetic⁵¹ and photochemical⁵² methods for actuation, these are outside the scope of this review.

Utilizing electrical signals to manipulate liquid metal provides key advantage over other techniques. Electrical approaches do not require moving parts or large power consumption, they are scalable to microsystems, and they offer control over both position and magnitude. Recent advances in the field have been achieved through an electrical technique that has existed for over a century: electrocapillarity.

1.3 Electrocapillarity

Electrocapillarity is one of the earliest reported methods for tuning the interfacial tension of liquid metals. Initially discovered by Lippmann in the 1870's⁵³, electrocapillarity is the change in the effective interfacial tension of a liquid metal in an inert electrolyte upon application of an electrical potential to the metal relative to a counter electrode. The density of

charge in the electrical double layer at the metal-solution interface changes in response to voltage. The double layer is effectively a capacitor; in order to lower the capacitive energy at the surface, the surface area of the metal increases, thereby changing the effective interfacial tension. For an ideally polarized electrode at constant composition, this change is described by the Lippmann equation, (Equation 1.1)⁵⁴.

$$-q = \frac{d\gamma}{dV} \quad (1.1)$$

where γ is the interfacial tension of the liquid metal, V is the electrode potential, and q is the charge density at the interface. One of the implications of this equation is that any increase in charge density –whether positive or negative – will result in a decrease in the interfacial tension of the liquid metal. This change can be characterized by an electrocapillary curve (**Figure 1.3**), which shows the change in interfacial tension as a function of potential⁵⁵. The peak of the electrocapillary curve represents the maximum interfacial tension of the metal, which occurs at the so-called ‘potential of zero charge’. The potential of zero charge depends on the metal and the electrolyte. Integration of the Lippmann equation yields Equation 1.2:

$$\gamma(V) = \gamma_0 - \frac{1}{2}C(V - V_0)^2 \quad (1.2)$$

where γ_0 is the interfacial tension at the potential of zero charge, C is the capacitance at the double layer, and V_0 is the potential of zero charge. These curves can be used to characterize the interfacial properties of mercury^{56,57} and oxide-free liquid gallium⁵⁸ in solution. Because of adsorption at the interface and the nature of the double layer, these curves are dependent on the concentration and type of electrolyte chosen⁵⁴.

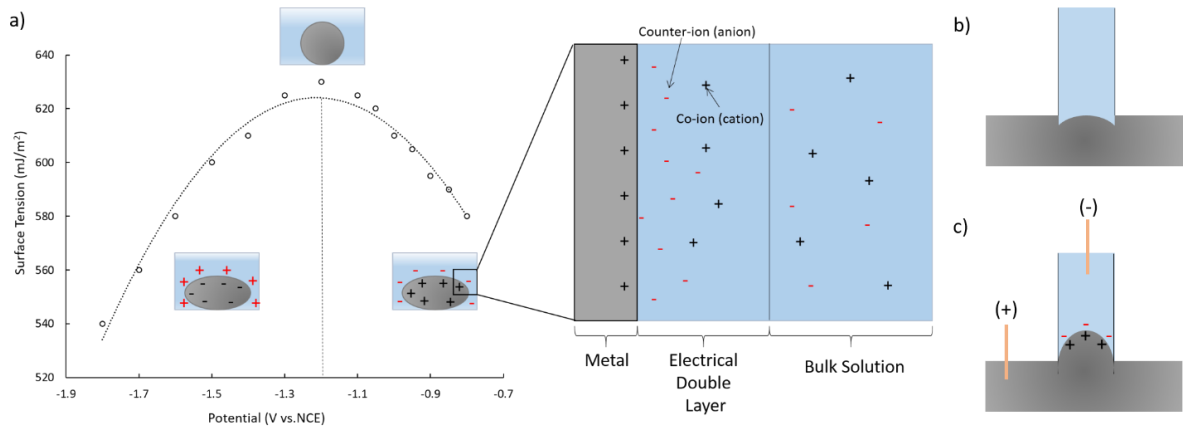


Figure 1.3: Electrocapillary behavior of liquid metals in electrolyte. a) Electrocapillary curve showing the surface tension of a liquid metal drop as a function of voltage. The apex of the curve represents the potential of zero charge; any change in voltage, whether positive or negative, results in a decrease in interfacial tension and a relative flattening of the drop due to gravity. The lowered interfacial tension is caused by the capacitance at the electrical double layer. Data reproduced from Frumkin et. al⁵⁵, with permission from Elsevier. b-c) The lowering of interfacial tension by electrocapillarity can induce the capillary rise of the metal through a small tube.

The mercury ‘beating heart’ experiment is a classic example of the effects of electrocapillarity⁵⁹. A drop of mercury in solution, when contacted from above by an iron or aluminum wire, develops an electrochemical potential that causes the interfacial tension of the mercury to decrease (and a corrosion reaction at the surface of the wire). Gravity causes the drop to flatten out, detaching the mercury from the wire, at which point the surface tension increases, causing the drop to bead up and once again contact the wire. This cycle repeats itself such that the mercury ‘beats’ at a certain frequency.

Electrocapillarity can create large changes (> 100 mN/m) to the interfacial tension of a liquid metal drop at relatively small potentials (~ 1 V). The ability to affect the liquid metal pressure with voltage has made electrocapillarity an effective tool for pumping at the

microscale⁶⁰⁻⁶², including capillary rise (Figure 1.3b). For example, electrocapillarity can create a microfluidic pump for aqueous electrolytes. Mercury confined to a vertically-oriented microchannel involves two primary forces: gravity and surface tension. An alternating potential changes the surface tension, causing the height of the mercury column to oscillate continuously⁶⁰. A similar method was also utilized to create a microfluidic check valve with the liquid metal⁶³. This technique has also been applied to the nanoscale to pump mercury into single-walled carbon nanotubes at less than 2.5 V, a technique that could lead to fabrication of continuous, uni-directional nanowires of liquid metal⁶¹. A similar method was recently used to steer the flow of liquid metals into select pathways through complex microchannels by electrically controlling the interfacial tension of the leading interface of the metal⁶⁴.

The terms “electrocapillarity” and “electrowetting” are often used interchangeably in the literature, but the two terms are distinct. Here, we differentiate the two phrases following the distinction offered by Jackel et al⁶⁵. While electrocapillarity specifically refers to the change in interfacial tension induced by an electrical potential at the boundary between two fluids, electrowetting refers to the change in wetting properties between a fluid and a separate material caused by electrocapillarity. This material can be a fluid, causing a continuous change in the wetting properties (as in continuous electrowetting) or a solid (as in electrowetting-on-dielectric).

1.4 Continuous Electrowetting

Applying an external electric field to discrete drops of the liquid metal in aqueous solution can create a surface tension gradient across the liquid metal surface. This gradient is caused by a potential drop through the electrolyte surrounding the metal (in the case of a plug of metal in a capillary, the thin layer of electrolyte between the metal and capillary walls) and, according to the principles of electrocapillarity, can drive fluid motion inside of the channel without directly contacting the liquid metal with an electrode. **Figure 1.4** shows an example of a mercury plug placed in a microfluidic channel filled with electrolyte⁶⁶. In the absence of an applied potential, the electrical double layer is distributed equally across both sides of the drop. However, the application of a potential across the ends of the microchannel results in a potential drop through the thin layer of liquid between the metal and the capillary walls. This potential drop induces an asymmetry in the electrical double layer across the drop, which causes a differential in surface tension that forces the drop to move.

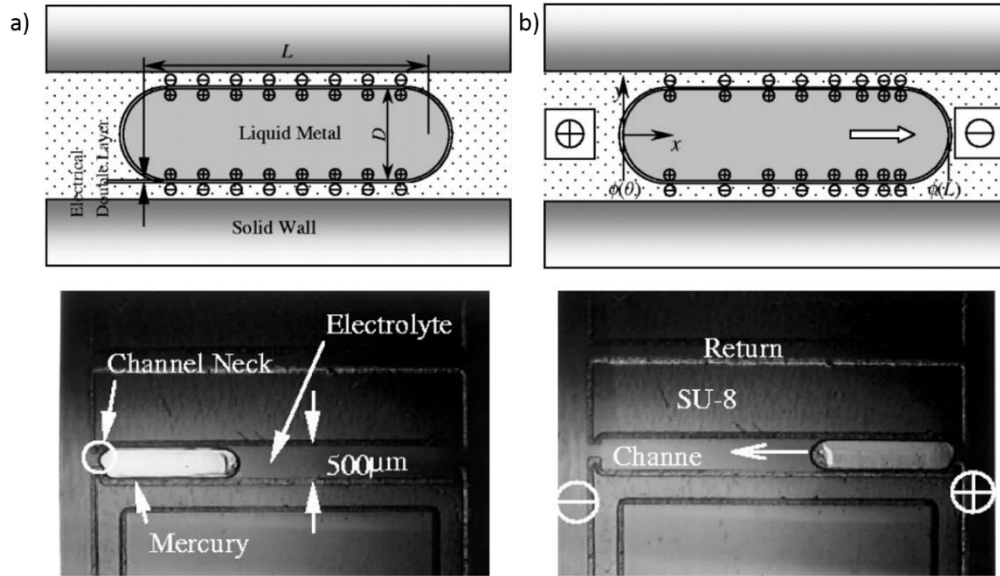


Figure 1.4: Mercury confined to a 500 μm wide microfluidic channel⁶⁶. Electrodes are present on both ends of the microchannel. a) In the absence of an applied voltage, the mercury plug remains stable in the channel. b) An applied potential between the electrodes causes actuation of the metal plug.

This effect is known as continuous electrowetting (CEW), and it is a direct result of electrocapillarity. To model CEW for an incompressible Newtonian fluid confined to a capillary, the Navier-Stokes equation for interfacial forces reduces to Equation 1.3:

$$\frac{dp}{dx} = \frac{2}{D} \frac{d\gamma}{dx} \quad (1.3)$$

where p is pressure, x is the dimension along the length of the capillary, and D is the inner diameter. Solving for the average velocity yields Equation 1.4:

$$v = -\frac{D}{6\mu} \left\{ \frac{d\gamma}{dx} \right\} \quad (1.4)$$

where v is the average velocity of the fluid, μ is the viscosity of the liquid metal, and $\{d\gamma/dx\}$ represents the average interfacial tension change normalized over the length of the drop. The voltage drop across the liquid metal from the applied potential difference dictates the average interfacial tension difference. Substituting the potential gradient yields Equation 1.5, an estimate for the average velocity:

$$v = -\frac{qD}{6\mu L}\Delta\phi \quad (1.5)$$

where L is the length of the drop, q is the charge in the electrical double layer at the interface between the electrolyte and liquid metal, and $\Delta\phi$ is the potential difference across it. This equation implies that the velocity – and the direction of the velocity – is dictated by the external applied potential, which can be easily controlled. In the absence of a potential, there is no gradient across the drop to drive the fluid flow. Substituting typical values for a liquid metal in aqueous solution indicates that the droplet velocity can exceed 100 mm/s. A more detailed derivation can be found in Beni et al⁶⁷.

CEW makes it relatively easy to move plugs of mercury inside of a channel filled with an electrolyte; the same is true for gallium-based alloys as long as precautions are taken to avoid adhesion of the oxide layer. There are at least two options to avoid adhesion in the presence of electrolyte: utilize channels filled with acid or base to chemically remove the oxide or pre-fill the channels with electrolyte (prior to injecting the metal plug) so that a slip layer of electrolyte forms between the metal plug and capillary walls^{46,48}.

CEW has been utilized to create a wide array of devices including pumps⁶⁸, optical components⁶⁹, valves⁷⁰, and RF devices⁷¹. However, the low friction environment found during CEW makes it difficult to control the final position of the liquid metal plug. A microfluidic channel with a variable diameter, as shown in **Figure 1.5a**, was designed to overcome this issue. The gallium alloy settled into local energy minima in the absence of a voltage, thereby preventing drift⁷¹.

The principles of CEW have been applied in ways that ensure a continuous flow of the liquid metal for various applications. One method for achieving continuous flow is the use of a microchannel loop to enable liquid metal micromotors⁶⁶ (Figure 1.5b and 1.5c). A sequential voltage was applied to electrodes placed in regular intervals around the perimeter of the channel; when the liquid metal reached an electrode, the polarity switched and an electrode was activated further along the channel, causing uninterrupted actuation of the drop. This method can move metal droplets with a velocity of 44 mm/s, with low voltage and low current.

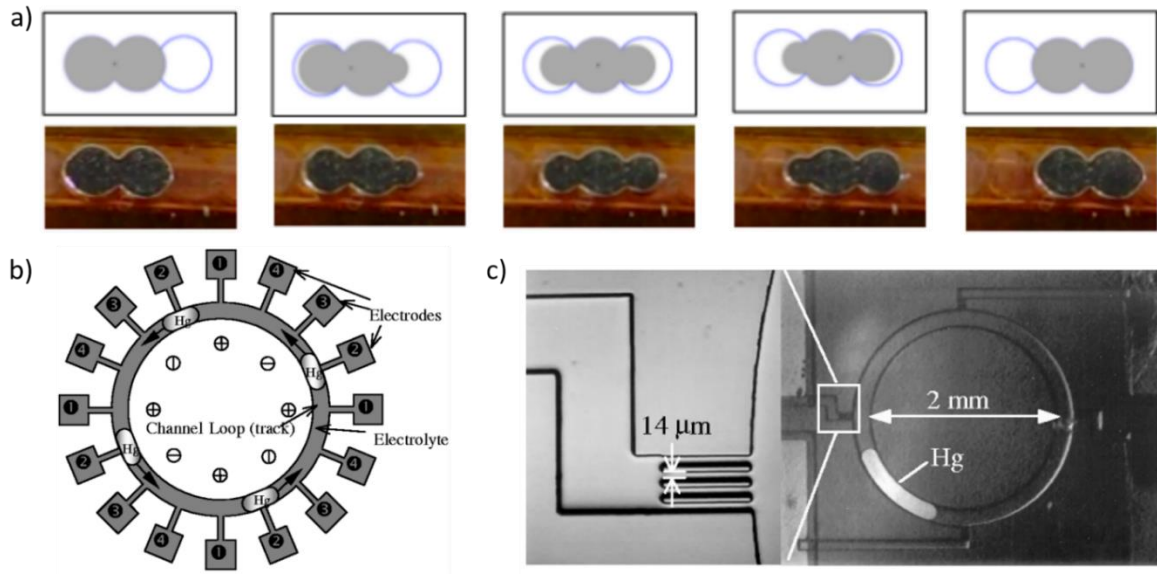


Figure 1.5: Devices based on continuous electrowetting. a) Simulation and experimental results of a plug of liquid metal moving to the right by continuous electrowetting (electrodes not shown)⁷¹. b) Schematic for a micromotor based on continuous electrowetting of a slug of Hg⁶⁶. c) Liquid metal micromotor. 14 μm ‘filters’ connect the main track to the electrode while preventing the liquid metal from exiting.

The optical properties of liquid metals make them ideal candidates to prevent light transmission or serve as fluidic mirrors. These properties were utilized to create an optical switch based on CEW⁶⁵. Low voltages were applied (from -1 V to 1 V) to a mercury plug in a rectangular capillary. Without an applied potential, light entering through a fiber refracts through the solution in the microchannel and is guided to a fiber; applying a voltage causes the drop to move, thereby reflecting the light back into a secondary fiber above the drop. This method for optical switching is advantageous, due to the low voltage and power consumption ($\sim 1 \mu\text{W}$) and reasonable switching times ($\sim 20 \mu\text{s}$).

CEW can also be applied to droplets outside of microchannels. When a droplet of a liquid metal is placed in a conductive electrolyte solution between two electrodes, a sufficient

electrical potential applied between the electrodes can cause actuation of the drop in the fluid. **Figure 1.6** shows an example of liquid metal “marbles” comprised of Galinstan (an alloy of gallium, indium, and tin) placed in a solution of NaOH with a pH of 13.5. Applying a DC potential between 2-15 V between the electrodes develops an asymmetry in the electrical double layer across the drop; this potential gradient leads to a differential surface tension that causes the drop to move toward the anode (due to the negative charge in basic solution)⁵⁹. The effect has also been demonstrated in a pure water solution, though larger voltages were necessary⁷³.

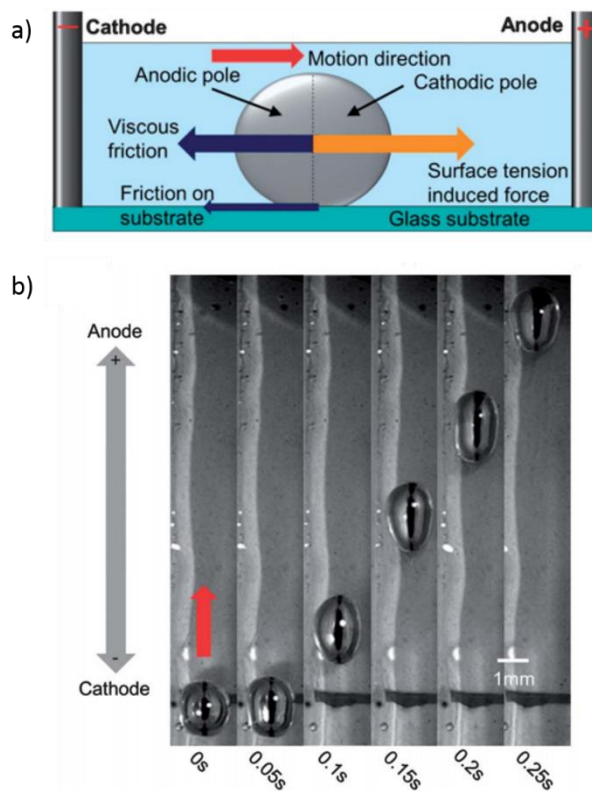


Figure 1.6: Continuous electrowetting of liquid metal marbles in an open solution⁷². a) Force balance of the Galinstan drop in a solution of NaOH. The surface tension gradient overcomes the viscous drag and substrate friction to drive movement of the drop. b) Time lapse of a Galinstan marble traversing between electrodes. Reproduced with permission from the Royal Society of Chemistry.

CEW can also be utilized for pumping electrolyte⁷⁴. Confining a drop of liquid metal in solution and constantly switching the polarity of the electrodes causes pumping, as seen in **Figure 1.7**. Confining the droplet prevents it from moving. Instead, the electrolyte moves. This type of pump is simple to fabricate, and creates large flow rates (5 mL/min) with limited power consumption (< 15 mW). A similar AC approach was used to create a micromixer, where the liquid metal was fixed to the substrate. Rather than moving the drop itself, AC

potentials caused undulations on the drop surface that leads to rapid mixing of oil droplets in the immersion solution due to Marangoni flow (i.e. flow due to gradients in surface tension)⁷⁵.

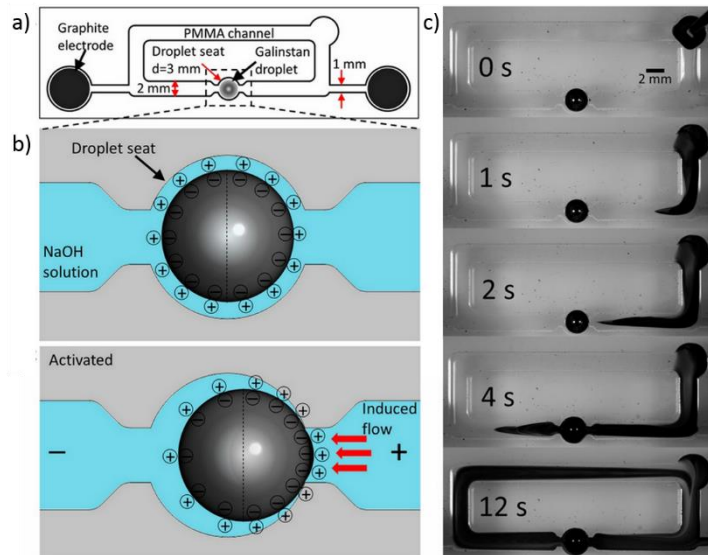


Figure 1.7: a) Design of a liquid metal pump in an open channel⁷⁴. b) Galinstan drop in confined channel. Polarity of graphite electrodes drives liquid metal in one direction, inducing electrolyte flow in the opposite direction. c) Time lapse of the dyed solution pumped completely through the channel. Copyright PNAS.

In spite of its ability to create liquid metal actuation with low power consumption, there are several drawbacks associated with CEW. Excessive voltages can lead to the formation of hydrogen at the surface of the cathode via electrolysis; while this is a negligible issue in open channels, the hydrogen bubbles can electrically isolate the electrode from the solution in microchannels, permanently interfering with the operation of continuous electrowetting. The use of AC voltages at higher frequencies can mitigate bubbles, but typically some DC bias is necessary to achieve asymmetric motion of fluid. Excessive potentials can also cause the liquid

metal to split up inside of the microchannel. To avoid these shortfalls, another method for liquid actuation can also be used: electrowetting-on-dielectric.

1.5 Electrowetting-on-dielectric

The ability to modulate and actuate fluids is not solely restricted to liquid metals immersed in electrolyte solutions. Charges at interfaces can overcome the interfacial tension of any conductive solution, including organics materials with dissolved electrolytes⁷⁶. This principle can be best illustrated by a droplet of water sitting on a conductive metal electrode. If a second electrode is inserted into the water, and a potential is applied between the electrode in the water and the metal substrate, charge rearrangement at the surface of the droplet will cause the droplet to change its apparent contact angle at the surface of the electrode. Mugele & Baret provide an excellent review on this topic⁵³.

This change in contact angle arises due to an imbalance at the three-point contact line between the vapor, liquid, and solid phase. In the absence of applied potential, the equilibrium contact angle is described by Young's Equation, which is derived from a force balance at the three-point contact line, Equation 1.6:

$$\gamma_{LV} \cos \theta_Y = \gamma_{SV} - \gamma_{SL} \quad (1.6)$$

where γ_{LV} is the interfacial tension between the liquid and vapor phase, γ_{SV} is the interfacial tension between the solid and vapor phase, γ_{SL} is the interfacial tension between the solid and liquid phase, and θ_Y represents the Young's contact angle. An applied voltage causes the liquid to increase its surface area against both the vapor and solid phases, thereby lowering its capacitive energy and decreasing the contact angle, as described in Equation 1.7,

$$\cos \theta = \cos \theta_Y - \frac{\varepsilon \varepsilon_0}{2d_H \gamma_{LV}} (V - V_0)^2 \quad (1.7)$$

where θ represents the apparent contact angle at a macroscopic scale, ε is the dielectric constant, ε_0 is the permittivity of free space, d_H is the thickness of the Helmholtz Layer, V is the applied potential, and V_0 is the open circuit potential. A more extensive derivation can be found in the literature⁵³. The contact angle θ is dictated by the initial contact angle at equilibrium and the ratio of the capacitive energy (driving the droplet toward the substrate) to the surface tension of the liquid. It should be noted that the Young's angle remains constant at the microscopic level, as does the interfacial tension between the liquid and vapor phases.

An insulating layer can also be added between the liquid and the conductive substrate⁷⁷, as illustrated in **Figure 1.8**. Although this layer increases the necessary voltage to move the droplet, it also prevents unwanted chemical reactions (provided that the voltage is kept below the breakdown voltage of the insulating layer)⁷⁸.

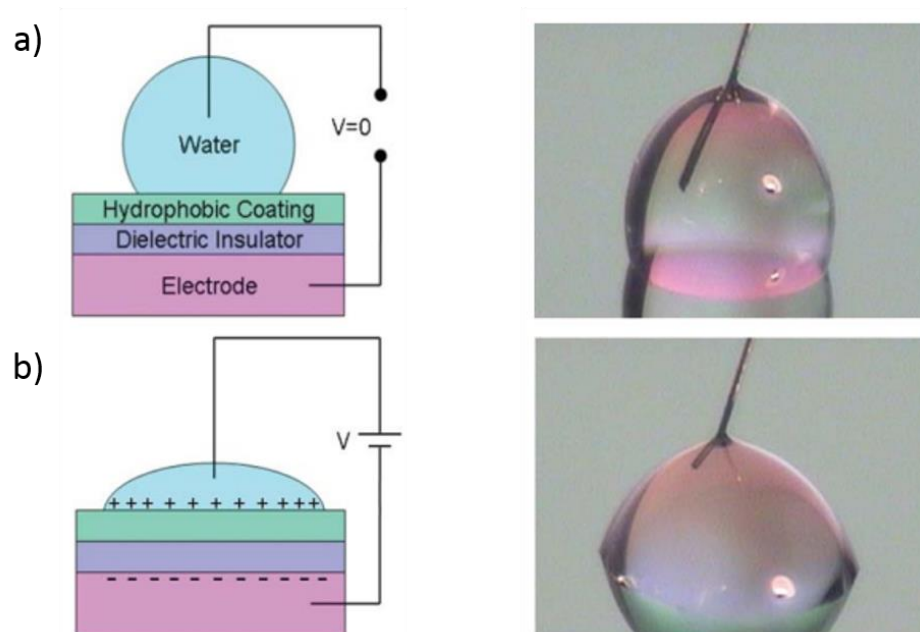


Figure 1.8: Electrowetting-on-dielectric⁷⁷. a) A conductive electrode is coated with a thin dielectric and hydrophobic coating, with a water droplet placed on top. The water reaches an equilibrium contact angle. b) A voltage is applied between the electrode and the droplet, causing charges to migrate to the interface and thereby decrease the effective contact angle. Reproduced with permission from the Royal Society of Chemistry.

This method is called electrowetting-on-dielectric (EWOD), and can be described by Equation 1.8:

$$\cos \theta = \cos \theta_Y - \frac{\epsilon \epsilon_0}{2d\gamma_{LV}} (V - V_0)^2 \quad (1.8)$$

where d , in this case, is the thickness of the insulating dielectric layer. For water, a thin hydrophobic coating is often added to increase the initial contact angle of the drop. For the most effective operation, it is desirable to use an insulating layer that is thin, has a large dielectric constant, and a large breakdown field. The change in contact angle upon applying a

voltage increases with lower interfacial tension, which can be accomplished by including surfactants that reduce the interfacial tension of the liquid phase⁷⁹.

EWOD carries many advantages for moving liquids: it is simple to fabricate, scalable, and requires no moving parts. EWOD has been utilized to drive fluids through capillaries⁸⁰, for aqueous droplet actuation⁸¹ and mixing⁸², for display technologies⁸³, and as a tool for biological diagnostics⁸⁴. EWOD's ability to function at small length scales is a particularly useful feature, as most lab-on-a-chip systems require large supporting components (e.g. mechanical pumps).

Although EWOD has conventionally been utilized for actuation of aqueous droplets, the same principles apply to liquid metals⁸⁵⁻⁸⁷. **Figure 1.9** shows an electrowetting curve, which measures the change in contact angle as a function of voltage, for mercury on a 600 nm thick parylene film⁸⁸ (parylene is a popular dielectric since it can be vacuum-deposited to create conformal, pin-hole free films). Similar results have been achieved for electrowetting of Galinstan¹³, but these took place under conditions that prevented the formation of the oxide layer, which adds a significant experimental complication. Achieving a significant change in contact angle requires a large voltage (>100s of volts) due to the large interfacial tension of liquid metals, which is a notable limitation. Placing liquid metal droplets on semiconducting substrates covered with oxides results in metal-oxide-semiconductor junctions that create asymmetry in the electrowetting curve^{86,87}.

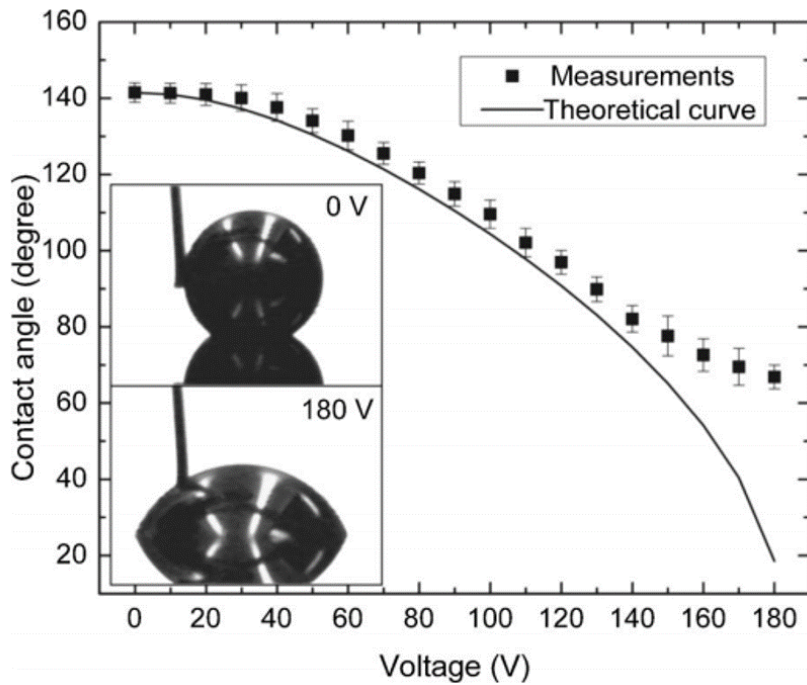


Figure 1.9: Electrowetting curve of a mercury drop. At larger voltages, the contact angle begins to saturate and deviate from the theoretical curve. Dielectric layer is a 600 nm parylene film⁸⁸. Reproduced with permission from ASME.

The principles of EWOD have been utilized to fabricate devices that leverage the properties of liquid metals⁸⁹. Much like the optical switch using CEW, EWOD can actuate mercury to guide light, including the use of a mercury drop as a tunable light reflector⁹⁰. In this case, the dielectric-coated electrode was positioned above the drop and composed of transparent materials. Without an applied voltage, the curvature of the drop allows impinging light to be reflected in all directions. Turning on the potential causes the drop to wet the substrate, and direct light back toward the source. Mercury can also be utilized as a piston underneath a mirror^{91,92}. Controlling electrically the shape of the mercury directs the reflection of the light.

The fast switching properties of EWOD have also been used to create thermal⁹³ and electrical MEMS switches⁹⁴⁻⁹⁷. An effective liquid metal switch should have minimal latency time; this is the amount of time necessary to activate the switch after the actuation signal. **Figure 1.10a** shows an example of a mercury microswitch. Here, the switching time was reduced by fabricating a microframe (Figure 1.10b) to hold the droplet in place and reduce the distance that the droplet had to travel. This allows for on-off latency times of 60 and 150 μ s, respectively, an order of magnitude improvement over previous mercury MEMS switches.

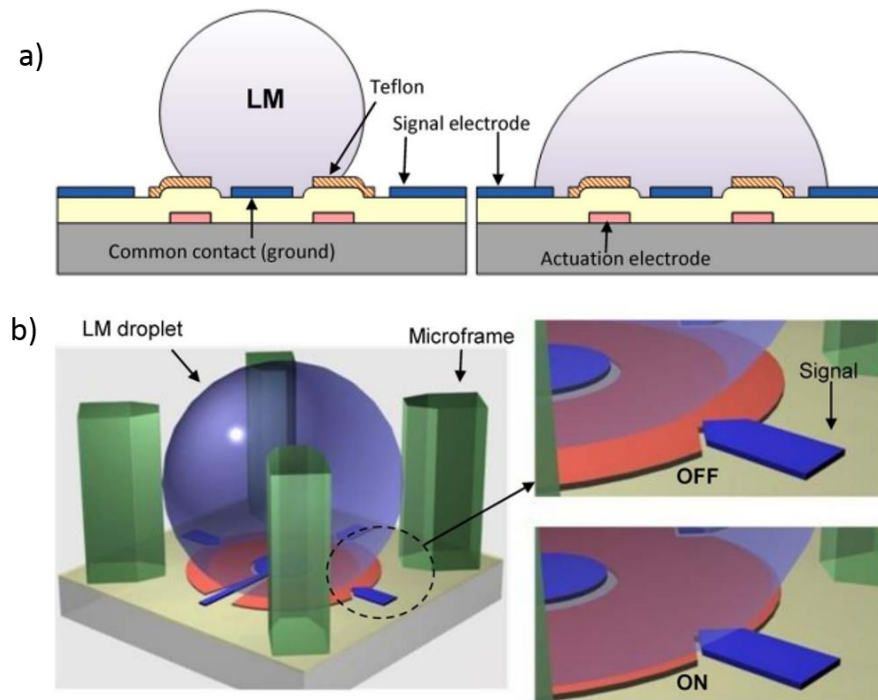


Figure 1.10: A liquid metal-based MEMS switch⁹⁸. a) A mercury droplet on an EWOD substrate for switching. b) The liquid metal droplet was placed in a microframe to ensure accurate positioning.

In addition to actuating droplets, electrowetting has been utilized to convert mechanical energy to electrical energy⁹⁹. Applying a voltage to a liquid metal in an electrowetting setup causes the metal to spread to a new equilibrium shape; mechanically pushing the drop beyond its equilibrium generates a current due to the resulting change in capacitance (arising from the increase in area between the liquid and substrate). In principle, this allows for power generations of up to 1 kW/m²; using multiple drops in series on a plate or in a capillary enables an increase in the current and therefore power.

There are two primary disadvantages of using EWOD systems for manipulating liquid metals: the ineffectiveness of EWOD on liquid metals that develop surface oxides, and the necessity of large voltages. Oxide layers provide mechanical impediments to actuation; aqueous acids and bases, which can remove the oxide, are conductive and therefore cannot be used in conjunction with EWOD. Insulating fluids that remove the oxide from gallium alloys would help address this limitation. Liquid metals also have large interfacial tensions that must be overcome to induce deformation. For water, it is possible to simply decrease the surface tension by including surfactants; while this is also possible for liquid metals (via self-assembled monolayers), these surfactants cannot affect a comparable change in surface tension^{100,101}. In the absence of these self-assembled monolayers, the liquid metal will have a surface tension approximately two orders of magnitude larger than an aqueous drop with a surfactant. This large surface tension necessitates the application of large voltages to achieve electrowetting, yet dielectric breakdown limits the maximum electric field (*i.e.* voltage divided by distance) that can be applied.

1.6 Electrochemically Controlled Capillarity

Electrochemical reactions at surfaces can, in principle, deposit species that help lower surface tension. Electrocapillarity experiments are designed typically to avoid electrochemical reactions such that changes in surface tension arise purely from electrical double layer effects. At excessive cathodic or anodic potentials, bubbles or other reactive by-products can form on the surface of the metal. A chemical reaction at the surface, however, does not necessarily preclude a change in surface tension, as evidenced by the beating mercury heart.

It has been demonstrated that oxidation on a surface-active metal can cause a significant decrease in surface tension¹⁰² and a change in wetting properties¹⁰³. This has been demonstrated, for instance, on an aluminum surface¹⁰⁴. By starting with a high vacuum and slowly increasing the oxygen concentration, the corresponding surface tension was shown to decrease (until the surface was saturated). However, these experiments were performed under carefully controlled oxygen concentrations in vacuum; furthermore, the growing oxide layer eventually acts as a mechanical impediment to further shape change, and the passivating nature of the oxide layer prevents further oxidation. Even noble metals that will not react with oxygen under normal conditions have shown reduced surface tension when electrochemically oxidized in solution¹⁰⁵. We believe Tsai et. al. were the first to show that, on liquid gallium, the surface tension could be decreased significantly by applying large oxidative potentials in acid¹⁰⁶. This surface tension decrease caused gravity-driven spreading of the droplet, allowing it to increase its surface area against the substrate. The researchers used this spreading to create a light valve (**Figure 1.11a** and **1.11b**); by applying less than 1 V into a solution of 5 M HCl, the metal blocked 96% of light transmission at fast switching speed (~49 s) with complete reversibility.

Turning off the voltage allowed the oxide layer on the surface to dissolve in the highly acidic solution, thereby increasing the surface tension and causing the gallium to bead up.

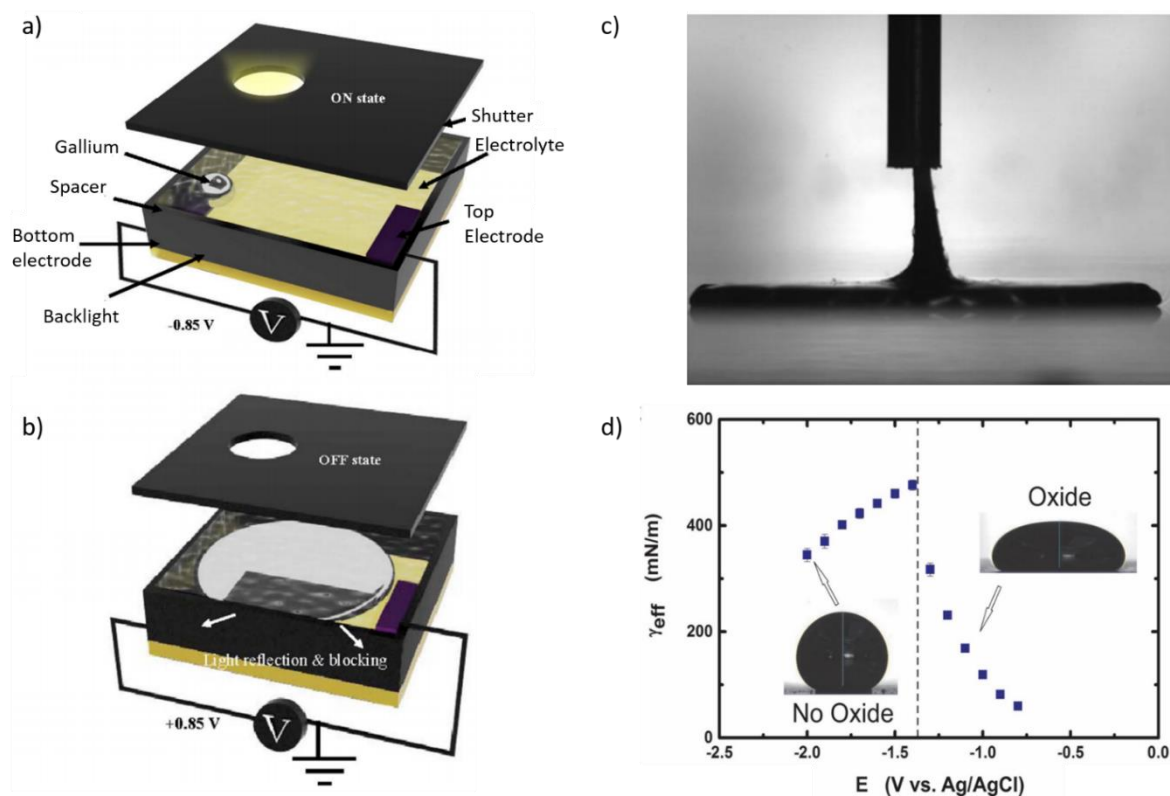


Figure 1.11: Electrochemically driven spreading of gallium-based alloys. a) A drop of liquid gallium sits on a conductor over a backlight. b) Applying a voltage to the drop causes spreading that blocks the back light¹⁰⁶. Reprinted with permission of AIP Publishing. c) A drop of liquid metal being oxidized at 2 V in 1 M NaOH. d) Surface tension of a eutectic gallium indium drop in 1 M NaOH. The vertical dotted line represents formation of the oxide layer¹⁰⁷. Copyright PNAS.

It was later shown that the formation of the oxide was actually the cause of the spreading, rather than standard electrocapillary effects¹⁰⁷. Figure 1.11c shows a 2 V potential

applied to eutectic gallium indium (EGaIn), in a solution of 1 M NaOH. As the droplet flattens, the oxide stabilizes the cylindrical filament that connects the drop to the syringe-needle electrode above. Figure 1.11d shows interfacial tension measurements of a sessile droplet of the liquid metal in 1 M NaOH as a function of potential. In classic electrocapillarity, the surface tension should vary parabolically with respect to voltage (cf. Equation 1.2). In the absence of the oxide layer, the droplet behaves in a manner consistent with traditional electrocapillarity; the surface tension decreases parabolically at negative potentials, until hydrogen bubbles form on the liquid metal at approximately -2 V. However, at potentials more positive than -1.3 V, the oxide forms on EGaIn and the interfacial tension declines sharply (~ 150 mN/m over 100 mV). Increasingly positive potentials drop the tension even more, approaching near-zero interfacial tension. At these potentials, the surface area of the droplet increased until it broke free of the electrical connection to the working electrode. It is reasoned that the oxide layer behaves as a surfactant between the liquid metal and electrolyte. The largest decrease in surface tension occurs when the oxide begins forming on the metal. In addition, deviation from classic electrocapillarity occurs at the oxidation potential. Although surface oxides typically provide physical barriers to flow, the use of electrolytes (such as 1 M NaOH) that continuously remove the oxide allow the metal to flow despite being covered with a film. That is, the oxidative deposition of the oxide layer competes with dissolution by the basic electrolyte. Figure 11d suggests that the effective interfacial tension of the metal can change from ~ 500 mN/m to near zero using approximately one volt (from the open circuit voltage of -1.5 V to -0.5 V) and the change is completely reversibly depending on the applied voltage. It is also possible to lower

the interfacial tension utilizing the potential from redox chemistry, rather than applying an external potential¹⁰⁸.

The reversibility of the oxide ‘surfactant’ allows simple injection and withdrawal from electrolyte-filled capillaries (**Figure 1.12**), an approach referred to as “electrochemically controlled capillarity” (ECC). ECC creates a substantial decline in surface tension, which drives the liquid metal into the channels^{62,108}, as shown in Figure 1.12a. In this example, the application of an oxidative potential between the liquid metal and the electrolyte (0.25 M NaOH) injected the liquid metal into a 600 μm channel at up to 2.5 cm/s. These high speeds are made possible by confining the metal in a shallow reservoir to increase the Laplace pressure to help push the metal into the channel. The build-up of excessive oxide at the interface ultimately hinders the injection rate; this can also be utilized as a feature to stabilize the shape of the liquid metal⁶². Removal of the oxide by a reducing potential can be used to increase the surface tension, causing withdrawal of the liquid metal from the channel at 10s of cm/s¹⁰⁹ (Figure 1.12b). The oxide is only removed at the interface of the between the electrolyte and the metal in contact with the electrode; this implies that the withdrawal stops immediately by removing the potential, and channels not in the direct path between the electrolyte and negative electrode remain stable. This can be seen in Figure 1.12c, where the liquid metal can find the shortest path of a maze, leaving the rest of the metal in the channel. This phenomenon is called ‘recapillarity’ because it uses reductive potentials to induce capillary motion.

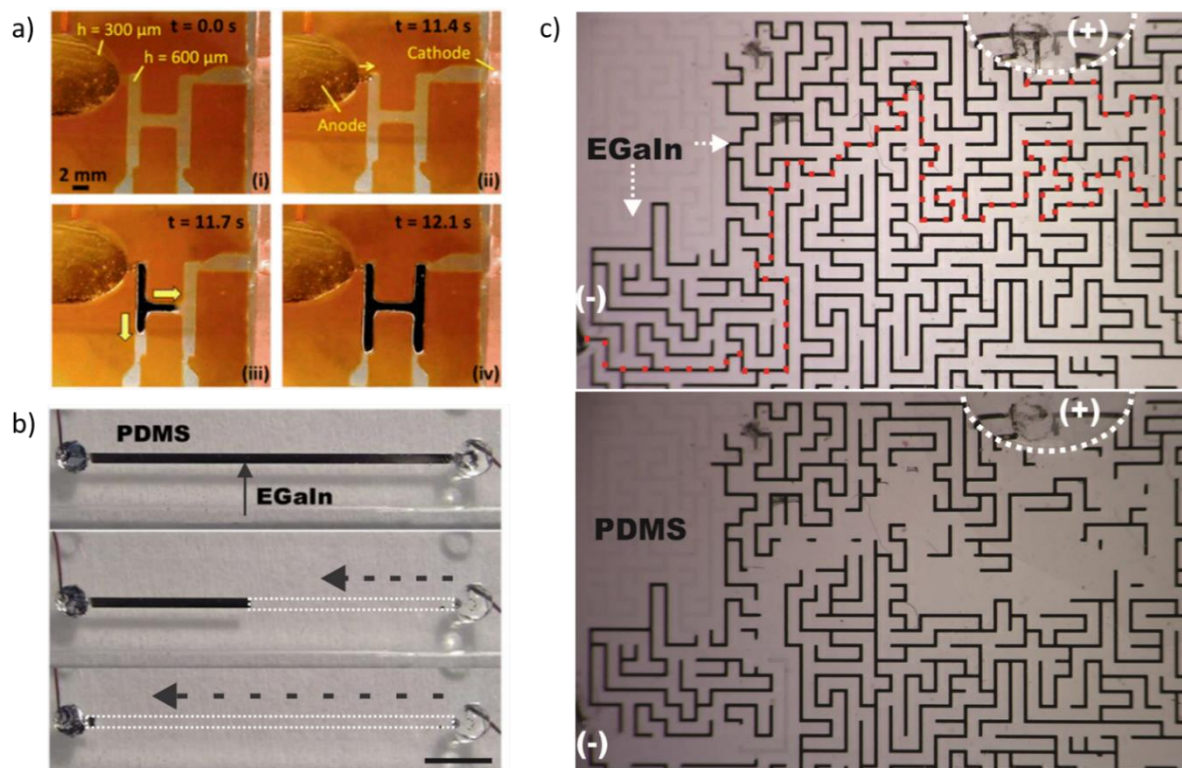


Figure 1.12: Electrochemical injection (ECC) and withdrawal (recapillarity) of a liquid metal. a) Galinstan is injected into a NaOH-filled microchannel by ECC (interfacial oxidation)¹⁰⁶. b) Reduction of the oxide layer at the interface of the channel creates an increase in the liquid metal surface tension, causing rapid withdrawal. c) The same mechanism allows the liquid metal to withdraw from the shortest path of a maze¹⁰⁹. Copyright John Wiley and Sons.

ECC was utilized recently to create reconfigurable reflectors¹¹⁰ and antennas¹¹¹. An electric potential was applied to the liquid metal in a microchannel filled with NaOH to elongate the metal. Varying the potential by < 8 V allowed the antenna to be tuned continuously and reversibly between 0.66 GHz and 3.4 GHz by changing the length of the liquid metal in a capillary connected to a reservoir. Voltages larger than 1 V are needed presumably due to the potential drop through the electrolyte. It is possible to freeze the metal to stabilize it in a temporary shape¹¹⁰ or use Laplace barriers to trap it in a metastable shape within channels.

This electrochemical method is promising, but it is not without shortcomings. Injection of the liquid metal results necessarily in a formation of the oxide, meaning that strong acids or bases must be used to continually remove excessive oxide layer. Neutral electrolytes cause the oxide to build-up and hinder mechanically the injection of the metal. There may be opportunities to explore other electrochemically active species to lower surface tension that do not present mechanical impediments to flow. In addition, electrochemical reactions at the surface of the metal are coupled with half reactions at counter electrodes that can create undesirable bubbles.

Table 1.1 shows a comparison of the advantages and disadvantages of using each of these techniques. In general, the methods that involve direct contact of the liquid metal with an electrolyte are require low voltages and low power to operate.

Table 1.1: Comparison of liquid metal actuation techniques.

Method	Voltage Requirement	Electrolyte	Chemical Reaction
Electrocapillarity	Low	Yes	No
Continuous Electrowetting	Low	Yes	No
Electrowetting-on-Dielectric	High	No	No
Electrochemically controlled capillarity	Low	Yes	Yes

1.7 Outlook and Conclusions

Liquid metals have already shown promise in a variety of functional devices due to their combination of fluidity and metallic properties. This review highlights several ways that liquid metals can be made reconfigurable through electrical potentials that alter interfacial tension or contact angle but there are still challenges with each of these methods, including the necessity of a supporting electrolyte (electrocapillarity, CEW, and ECC), large voltages and oxide free surfaces in an electrically insulating ambient (EWOD). Future work should focus on addressing some of these practical limitations, increasing actuation speeds, providing routes to meta-stable shapes (so the metal can temporarily get ‘trapped’ in shapes that maintain without voltage), improving the complexity of shapes, as well as attempting to expand further into the nanoscale, with the goal of simple, low power, reconfigurable circuitry.

1.8 Acknowledgements

The authors acknowledge support from the NSF CBET-1510772 and AFRL. We are also grateful to insights from Prof. Jason Heikenfeld.

1.9 Thesis Layout

Chapters 1-4 in this thesis are based on the following publications:

Chapter 1: Eaker, C.B., Dickey, M.D. Liquid Metal Actuation by Electrical Control of Interfacial Tension. *Appl. Phys. Rev.* **3**, 031103 (2016)

Chapter 2: Eaker, C.B., Khan, M.R., Bowden, E.F., Dickey, M.D. Giant and Switchable Surface Activity of a Liquid Metal via Surface Oxidation. *Proc. Natl. Acad. Sci.* **111**, 14047–14051 (2014).

Chapter 3: Eaker, C.B., Hight, D., O'Regan, J., Dickey, M.D., Daniels, K.E. Oxide-Mediated Fingering Instabilities in Liquid Metals. *In Preparation*.

Chapter 4: Eaker, C.B., Joshipura, I., Maxwell, L., Heikenfeld, J., Dickey, M.D. Electrowetting without Applied Potential using Paint-on Electrodes. *In Preparation*.

1.10 References

1. Bauer, S. *et al.* 25th Anniversary Article: A Soft Future: From Robots and Sensor Skin to Energy Harvesters. *Adv. Mater.* **26**, 149–162 (2013).
2. Kim, S., Laschi, C. & Trimmer, B. Soft robotics: a bioinspired evolution in robotics. *Trends Biotechnol.* **31**, 287–294 (2013).
3. Hammock, M. L., Chortos, A., Tee, B. C.-K., Tok, J. B.-H. & Bao, Z. 25th Anniversary Article: The Evolution of Electronic Skin (E-Skin): A Brief History, Design Considerations, and Recent Progress. *Adv. Mater.* **25**, 5997–6038 (2013).
4. Zeng, W. *et al.* Fiber-Based Wearable Electronics: A Review of Materials, Fabrication, Devices, and Applications. *Adv. Mater.* **26**, 5310–5336 (2014).
5. Ahn, J.-H. & Je, J. H. Stretchable electronics: materials, architectures and integrations. *J. Phys. Appl. Phys.* **45**, 103001 (2012).
6. Joshipura, I. D., Ayers, H. R., Majidi, C. & Dickey, M. D. Methods to pattern liquid metals. *J. Mater. Chem. C* **3**, 3834–3841 (2015).
7. Clarkson, T. W. & Magos, L. The toxicology of mercury and its chemical compounds. *Crit. Rev. Toxicol.* **36**, 609–662 (2006).
8. Lu, Y. *et al.* Transformable liquid-metal nanomedicine. *Nat. Commun.* **6**, 10066 (2015).

9. Zakharov, D. Eutectic Point of Gallium-Indium System. *Zhurnal Fiz. Khimii* **49**, 2208–2210 (1975).
10. Regan, M. J. *et al.* X-ray study of the oxidation of liquid-gallium surfaces. *Phys. Rev. B Condens. Matter* **55**, 10786–10790 (1997).
11. Giguère, P. A. & Lamontagne, D. Polarography with a Dropping Gallium Electrode. *Science* **120**, 390–391 (1954).
12. Doudrick, K. *et al.* Different Shades of Oxide: From Nanoscale Wetting Mechanisms to Contact Printing of Gallium-Based Liquid Metals. *Langmuir* **30**, 6867–6877 (2014).
13. Liu, T., Sen, P. & Kim, C. J. Characterization of Nontoxic Liquid-Metal Alloy Galinstan for Applications in Microdevices. *J. Microelectromechanical Syst.* **21**, 443–450 (2012).
14. Dickey, M. D. *et al.* Eutectic Gallium-Indium (EGaIn): A Liquid Metal Alloy for the Formation of Stable Structures in Microchannels at Room Temperature. *Adv. Funct. Mater.* **18**, 1097–1104 (2008).
15. Kramer, R. K., Majidi, C. & Wood, R. J. Masked Deposition of Gallium-Indium Alloys for Liquid-Embedded Elastomer Conductors. *Adv. Funct. Mater.* **23**, 5292–5296 (2013).
16. Ladd, C., So, J.-H., Muth, J. & Dickey, M. D. 3D Printing of Free Standing Liquid Metal Microstructures. *Adv. Mater.* **25**, 5081–5085 (2013).
17. Fassler, A. & Majidi, C. 3D Structures of Liquid-Phase GaIn Alloy Embedded in PDMS with Freeze Casting. *Lab. Chip* **13**, 4442–4450 (2013).
18. Jeong, S. H., Hjort, K. & Wu, Z. Tape Transfer Printing of a Liquid Metal Alloy for Stretchable RF Electronics. *Sensors* **14**, 16311–16321 (2014).

19. Dickey, M. D. Emerging Applications of Liquid Metals Featuring Surface Oxides. *ACS Appl. Mater. Interfaces* **6**, 18369–18379 (2014).
20. Xia, Y. & Whitesides, G. M. Soft Lithography. *Annu. Rev. Mater. Sci.* **28**, 153–184 (1998).
21. McDonald, J. C. *et al.* Fabrication of microfluidic systems in poly(dimethylsiloxane). *ELECTROPHORESIS* **21**, 27–40 (2000).
22. Lipomi, D. J. *et al.* Skin-like pressure and strain sensors based on transparent elastic films of carbon nanotubes. *Nat Nano* **6**, 788–792 (2011).
23. Park, Y.-L., Chen, B.-R. & Wood, R. J. Design and Fabrication of Soft Artificial Skin Using Embedded Microchannels and Liquid Conductors. *IEEE Sens. J.* **12**, 2711–2718 (2012).
24. Kim, H.-J., Son, C. & Ziaie, B. A multiaxial stretchable interconnect using liquid-alloy-filled elastomeric microchannels. *Appl. Phys. Lett.* **92**, 11904-11904–3 (2008).
25. Park, J. *et al.* Three-dimensional nanonetworks for giant stretchability in dielectrics and conductors. *Nat. Commun.* **3**, 916 (2012).
26. Zhu, S. *et al.* Ultrastretchable Fibers with Metallic Conductivity Using a Liquid Metal Alloy Core. *Adv. Funct. Mater.* **23**, 2308–2314 (2013).
27. Boley, J. W., White, E. L. & Kramer, R. K. Mechanically Sintered Gallium-Indium Nanoparticles. *Adv. Mater.* **27**, 2355–2360 (2015).
28. So, J.-H. & Dickey, M. D. Inherently aligned microfluidic electrodes composed of liquid metal. *Lab Chip* **11**, 905–911 (2011).

29. Pekas, N., Zhang, Q. & Juncker, D. Electrostatic actuator with liquid metal–elastomer compliant electrodes used for on-chip microvalving. *J. Micromechanics Microengineering* **22**, 97001 (2012).
30. Liu, Y., Gao, M., Mei, S., Han, Y. & Liu, J. Ultra-compliant liquid metal electrodes with in-plane self-healing capability for dielectric elastomer actuators. *Appl. Phys. Lett.* **103**, 64101-64101-4 (2013).
31. Ma, K.-Q. & Liu, J. Nano liquid-metal fluid as ultimate coolant. *Phys. Lett. A* **361**, 252–256 (2007).
32. Zhu, J. Y., Tang, S.-Y., Khoshmanesh, K. & Ghorbani, K. An Integrated Liquid Cooling System Based on Galinstan Liquid Metal Droplets. *ACS Appl. Mater. Interfaces* **8**, 2173–2180 (2016).
33. So, J.-H. *et al.* Reversibly Deformable and Mechanically Tunable Fluidic Antennas. *Adv. Funct. Mater.* **19**, 3632–3637 (2009).
34. Cheng, S., Wu, Z., Hallbjorner, P., Hjort, K. & Rydberg, A. Foldable and Stretchable Liquid Metal Planar Inverted Cone Antenna. *IEEE Trans. Antennas Propag.* **57**, 3765–3771 (2009).
35. Cheng, S. & Wu, Z. Microfluidic stretchable RF electronics. *Lab. Chip* **10**, 3227–3234 (2010).
36. Kubo, M. *et al.* Stretchable Microfluidic Radiofrequency Antennas. *Adv. Mater.* **22**, 2749–2752 (2010).

37. Hayes, G. J., So, J.-H., Qusba, A., Dickey, M. D. & Lazzi, G. Flexible Liquid Metal Alloy (EGaIn) Microstrip Patch Antenna. *IEEE Trans. Antennas Propag.* **60**, 2151–2156 (2012).
38. Ohta, A. T., Guo, S., Lei, B. J., Hu, W. & Shiroma, W. A. A liquid-metal tunable electromagnetic-bandgap microstrip filter. in *2012 IEEE International Conference on Wireless Information Technology and Systems (ICWITS)* 1–4 (2012). doi:10.1109/ICWITS.2012.6417735
39. King, A. J. *et al.* Microfluidically Switched Frequency-Reconfigurable Slot Antennas. *IEEE Antennas Wirel. Propag. Lett.* **12**, 828–831 (2013).
40. Koo, C. *et al.* Manipulating Liquid Metal Droplets in Microfluidic Channels With Minimized Skin Residues Toward Tunable RF Applications. *J. Microelectromechanical Syst.* **PP**, 1–1 (2015).
41. Jeong, S. H. *et al.* Liquid alloy printing of microfluidic stretchable electronics. *Lab. Chip* **12**, 4657 (2012).
42. Cheng, S., Rydberg, A., Hjort, K. & Wu, Z. Liquid metal stretchable unbalanced loop antenna. *Appl. Phys. Lett.* **94**, 144103 (2009).
43. Cheng, S. X., Li, T. & Chandra, S. Producing molten metal droplets with a pneumatic droplet-on-demand generator. *J. Mater. Process. Technol.* **159**, 295–302 (2005).
44. Tropmann, A. *et al.* Pneumatic dispensing of nano- to picoliter droplets of liquid metal with the StarJet method for rapid prototyping of metal microstructures. *Microfluid. Nanofluidics* **12**, 75–84 (2012).

45. Cumby, B. L. *et al.* Reconfigurable liquid metal circuits by Laplace pressure shaping. *Appl. Phys. Lett.* **101**, 174102 (2012).
46. Khan, M. R., Trlica, C., So, J.-H., Valeri, M. & Dickey, M. D. Influence of Water on the Interfacial Behavior of Gallium Liquid Metal Alloys. *ACS Appl. Mater. Interfaces* **6**, 22467–22473 (2014).
47. Li, G., Parmar, M., Kim, D., Lee, J.-B. (JB) & Lee, D.-W. PDMS based coplanar microfluidic channels for the surface reduction of oxidized Galinstan. *Lab. Chip* **14**, 200 (2014).
48. Ilyas, N., Butcher, D. P., Durstock, M. F. & Tabor, C. E. Ion Exchange Membranes as an Interfacial Medium to Facilitate Gallium Liquid Metal Alloy Mobility. *Adv. Mater. Interfaces* n/a-n/a (2016). doi:10.1002/admi.201500665
49. Zhang, J., Yao, Y., Sheng, L. & Liu, J. Self-Fueled Biomimetic Liquid Metal Mollusk. *Adv. Mater.* **27**, 2648–2655 (2015).
50. Mohammed, M., Sundaresan, R. & Dickey, M. D. Self-Running Liquid Metal Drops that Delaminate Metal Films at Record Velocities. *ACS Appl. Mater. Interfaces* **7**, 23163–23171 (2015).
51. Wang, L. & Liu, J. Electromagnetic rotation of a liquid metal sphere or pool within a solution. *Proc. R. Soc. -Math. Phys. Eng. Sci.* **471**, 20150177 (2015).
52. Tang, X. *et al.* Photochemically induced motion of liquid metal marbles. *Appl. Phys. Lett.* **103**, 174104 (2013).
53. Mugele, F. & Baret, J. C. Electrowetting: From basics to applications. *J. Phys.-Condens. Matter* **17**, R705–R774 (2005).

54. Grahame, D. C. The Electrical Double Layer and the Theory of Electrocapillarity. *Chem. Rev.* **41**, 441–501 (1947).
55. Frumkin, A., Polianovskaya, N., Grigoryev, N. & Bagotskaya, I. Electrocapillary phenomena on gallium. *Electrochimica Acta* **10**, 793–802 (1965).
56. Marichev, V. A. Maximum surface tension and optimum surface electron density. *Colloids Surf. Physicochem. Eng. Asp.* **389**, 63–68 (2011).
57. Alam, M. T., Islam, M. M., Okajima, T. & Ohsaka, T. Ionic Liquid Structure Dependent Electrical Double Layer at the Mercury Interface. *J. Phys. Chem. C* **112**, 2601–2606 (2008).
58. Bagotskaya, I. A., Morozov, A. M. & Grigoryev, N. B. On the zero-charge potential of gallium in aqueous solutions and the origin of high capacitance at the gallium/solution interface. *Electrochimica Acta* **13**, 873–879 (1968).
59. Kim, C. W., Yeo, I.-H. & Paik, W.-K. Mechanism of the mercury beating heart: An experimental study of the electrochemical-mechanical oscillator. *Electrochimica Acta* **41**, 2829–2836 (1996).
60. Ni, J., Zhong, C.-J., Coldiron, S. J. & Porter, M. D. Electrochemically Actuated Mercury Pump for Fluid Flow and Delivery. *Anal. Chem.* **73**, 103–110 (2001).
61. Chen, J. Y., Kutana, A., Collier, C. P. & Giapis, K. P. Electrowetting in Carbon Nanotubes. *Science* **310**, 1480–1483 (2005).
62. Gough, R. C. *et al.* Rapid electrocapillary deformation of liquid metal with reversible shape retention. *Micro Nano Syst. Lett.* **3**, 1–9 (2015).

63. Ni, J., Coldiron, S. J., Zhong, C.-J. & Porter, M. D. Electrochemically-actuated mercury valve for flow rate and direction control: design, characterization, and applications. *J. Electroanal. Chem.* **504**, 166–174 (2001).
64. Tang, S.-Y., Lin, Y., Joshipura, I. D., Khoshmanesh, K. & Dickey, M. D. Steering liquid metal flow in microchannels using low voltages. *Lab. Chip* **15**, 3905–3911 (2015).
65. Jackel, J. L., Hackwood, S. & Beni, G. Electrowetting optical switch. *Appl. Phys. Lett.* **40**, 4–5 (1982).
66. Lee, J. & Kim, C. J. Surface-tension-driven microactuation based on continuous electrowetting. *J. Microelectromechanical Syst.* **9**, 171–180 (2000).
67. Beni, G., Hackwood, S. & Jackel, J. L. Continuous electrowetting effect. *Appl. Phys. Lett.* **40**, 912–914 (1982).
68. Yun, K.-S., Cho, I.-J., Bu, J.-U., Kim, C.-J. & Yoon, E. A surface-tension driven micropump for low-voltage and low-power operations. *J. Microelectromechanical Syst.* **11**, 454–461 (2002).
69. Lea, M. C. Optical modulators based on electrocapillarity. *Opt. Lett.* **6**, 395 (1981).
70. M. Le Berre, Y. C. Electrocapillary force actuation of microfluidic elements. *Microelectron. Eng.* **78–79**, 93–99 (2005).
71. Gough, R. C. *et al.* Continuous Electrowetting of Non-toxic Liquid Metal for RF Applications. *IEEE Access* **2**, 874–882 (2014).
72. Tang, S.-Y. *et al.* Electrochemically induced actuation of liquid metal marbles. *Nanoscale* **5**, 5949–5957 (2013).

73. Sheng, L., Zhang, J. & Liu, J. Diverse Transformations of Liquid Metals Between Different Morphologies. *Adv. Mater.* **26**, 6036–6042 (2014).
74. Tang, S.-Y. *et al.* Liquid metal enabled pump. *Proc. Natl. Acad. Sci.* **111**, 3304–3309 (2014).
75. Tang, S.-Y. *et al.* Liquid Metal Actuator for Inducing Chaotic Advection. *Adv. Funct. Mater.* **24**, 5851–5858 (2014).
76. Kornyshev, A. A. *et al.* Ultra-Low-Voltage Electrowetting. *J. Phys. Chem. C* **114**, 14885–14890 (2010).
77. Shamai, R., Andelman, D., Berge, B. & Hayes, R. Water, electricity, and between... On electrowetting and its applications. *Soft Matter* **4**, 38–45 (2007).
78. Quilliet, C. & Berge, B. Electrowetting: a recent outbreak. *Curr. Opin. Colloid Interface Sci.* **6**, 34–39 (2001).
79. Raccurt, O., Berthier, J., Clementz, P., Borella, M. & Plissonnier, M. On the influence of surfactants in electrowetting systems. *J. Micromechanics Microengineering* **17**, 2217–2223 (2007).
80. Prins, M. W. J., Welters, W. J. J. & Weekamp, J. W. Fluid control in multichannel structures by electrocapillary pressure. *Science* **291**, 277–280 (2001).
81. Cho, S. K., Moon, H. J. & Kim, C. J. Creating, transporting, cutting, and merging liquid droplets by electrowetting-based actuation for digital microfluidic circuits. *J. Microelectromechanical Syst.* **12**, 70–80 (2003).
82. Paik, P., Pamula, V. K., Pollack, M. G. & Fair, R. B. Electrowetting-based droplet mixers for microfluidic systems. *Lab. Chip* **3**, 28–33 (2003).

83. Hayes, R. A. & Feenstra, B. J. Video-speed electronic paper based on electrowetting. *Nature* **425**, 383–385 (2003).
84. Srinivasan, V., Pamula, V. K. & Fair, R. B. An integrated digital microfluidic lab-on-a-chip for clinical diagnostics on human physiological fluids. *Lab. Chip* **4**, 310–315 (2004).
85. Antelmi, D. A., Connor, J. N. & Horn, R. G. Electrowetting Measurements with Mercury Showing Mercury/Mica Interfacial Energy Depends on Charging. *J. Phys. Chem. B* **108**, 1030–1037 (2004).
86. Arscott, S. & Gaudet, M. Electrowetting at a liquid metal-semiconductor junction. *Appl. Phys. Lett.* **103**, 74104 (2013).
87. Arscott, S. Electrowetting at a liquid metal-oxide-semiconductor junction. *Appl. Phys. Lett.* **103**, 144101 (2013).
88. Wan, Z., Zeng, H. & Feinerman, A. Reversible Electrowetting of Liquid-Metal Droplet. *J. Fluids Eng.* **129**, 388–394 (2007).
89. Latorre, L. *et al.* Electrostatic actuation of microscale liquid-metal droplets. *J. Microelectromechanical Syst.* **11**, 302–308 (2002).
90. Wan, Z., Zeng, H. & Feinerman, A. Area-tunable micromirror based on electrowetting actuation of liquid-metal droplets. *Appl. Phys. Lett.* **89**, 201107-201107–3 (2006).
91. Zeng, H. J., Feinerman, A. D., Wan, Z. L. & Patel, P. R. Piston-motion micromirror based on electrowetting of liquid metals. *J. Microelectromechanical Syst.* **14**, 285–294 (2005).
92. Zeng, H., Wan, Z. & Feinerman, A. D. Tilting Micromirror With a Liquid-Metal Pivot. *J. Microelectromechanical Syst.* **15**, 1568–1575 (2006).

93. Tsukamoto, T., Esashi, M. & Tanaka, S. Long working range mercury droplet actuation. *J. Micromechanics Microengineering* **19**, 94016 (2009).
94. Kim, J., Shen, W., Latorre, L. & Kim, C.-J. A micromechanical switch with electrostatically driven liquid-metal droplet. *Sens. Actuators Phys.* **97–98**, 672–679 (2002).
95. Chen, C.-H. & Peroulis, D. Liquid RF MEMS Wideband Reflective and Absorptive Switches. *IEEE Trans. Microw. Theory Tech.* **55**, 2919–2929 (2007).
96. Sen, P. & Kim, C.-J. A Fast Liquid-Metal Droplet Microswitch Using EWOD-Driven Contact-Line Sliding. *J. Microelectromechanical Syst.* **18**, 174–185 (2009).
97. Damgaci, Y. & Cetiner, B. A. A frequency reconfigurable antenna based on digital microfluidics. *Lab. Chip* **13**, 2883–2887 (2013).
98. Kim, O., Shin, T. J. & Park, M. J. Fast low-voltage electroactive actuators using nanostructured polymer electrolytes. *Nat. Commun.* **4**, (2013).
99. Krupenkin, T. & Taylor, J. A. Reverse electrowetting as a new approach to high-power energy harvesting. *Nat. Commun.* **2**, 448 (2011).
100. Kraack, H., Tamam, L., Sloutskin, E., Deutsch, M. & Ocko, B. M. Alkyl-thiol Langmuir Films on the Surface of Liquid Mercury. *Langmuir* **23**, 7571–7582 (2007).
101. Elsen, A. *et al.* Surface Layering at the Mercury-Electrolyte Interface. *Phys. Rev. Lett.* **104**, 105501 (2010).
102. Molina, J.M., Voytovych, R., Louis, E., Eustathopoulos, N. The surface tension of liquid aluminum in high vacuum: the role of surface condition. *Int. J. Adhes. Adhes.* **27**, 394-401 (2007).

103. Sobczak, N., Sobczak, J., Asthana, R., Purgert, R. The mystery of molten metal. *69th World Foundry Congress*. (2010).
104. Giuranno, D., Ricci, E., Arato, E. & Costa, P. Dynamic surface tension measurements of an aluminium-oxygen system. *Acta Mater.* **54**, 2625–2630 (2006).
105. Lin, K. F. & Beck, T. R. Surface Stress Curves for Gold. *J. Electrochem. Soc.* **123**, 1145–1151 (1976).
106. Tsai, J. T. H., Ho, C.-M., Wang, F.-C. & Liang, C.-T. Ultrahigh contrast light valve driven by electrocapillarity of liquid gallium. *Appl. Phys. Lett.* **95**, 251110 (2009).
107. Khan, M. R., Eaker, C. B., Bowden, E. F. & Dickey, M. D. Giant and switchable surface activity of liquid metal via surface oxidation. *Proc. Natl. Acad. Sci.* **111**, 14047–14051 (2014).
108. Gough, R. C. *et al.* Self-Actuation of Liquid Metal via Redox Reaction. *ACS Appl. Mater. Interfaces* **8**, 6–10 (2016).
109. Khan, M. R., Trlica, C. & Dickey, M. D. Recapillarity: Electrochemically Controlled Capillary Withdrawal of a Liquid Metal Alloy from Microchannels. *Adv. Funct. Mater.* **25**, 671–678 (2015).
110. Chrimes, A. F., Berean, K. J., Mitchell, A., Rosengarten, G. & Kalantar-zadeh, K. Controlled Electrochemical Deformation of Liquid-Phase Gallium. *ACS Appl. Mater. Interfaces* **8**, 3833–3839 (2016).

111. Wang, M., Trlica, C., Khan, M. R., Dickey, M. D. & Adams, J. J. A reconfigurable liquid metal antenna driven by electrochemically controlled capillarity. *J. Appl. Phys.* **117**, 194901 (2015).

Chapter 2

Giant and Switchable Surface Activity of Liquid Metal via Surface Oxidation

2.1 Introduction

The ability to control interfacial energy is an effective approach for manipulating fluids at sub-millimeter length scales due to the dominance of these forces at these small length scales and can be accomplished using a wide variety of methods including temperature^{1,2}, light³, surface chemistry⁴⁻⁶, or electrostatics⁷. These techniques are effective for many organic and aqueous solutions, but they have limited utility for manipulating high interfacial tension liquids, such as liquid metals. Liquid metals offer new opportunities for soft, stretchable, and shape-reconfigurable electronic and electromagnetic components⁸⁻¹². Although it is possible to mechanically manipulate these fluids at sub-millimeter length scales¹³, electrical methods^{14,15} are preferable due to the ease of miniaturization, control, and integration. Existing electrohydrodynamic techniques can modestly tune the interfacial tension of metals but either limit the shape of liquid metals to plugs (e.g., continuous electrowetting)¹⁶ or necessitate excessive potentials to achieve actuation on a limited scale (e.g., electrowetting)¹⁷. Here, we demonstrate that the surface oxide on a liquid metal can be formed or removed in situ using low voltages (<1 V) and behaves like a surfactant that can significantly lower its interfacial tension from ≈ 500 mJ/m² to near zero. In contrast, conventional molecular surfactants affect only modest changes in interfacial tension (changes of ≈ 20 -50 mJ/m²) and are difficult to remove rapidly on demand¹⁸. Our approach relies on the electrical control of surface oxidation, which is simple, requires minimal energy, and provides rapid and reversible control of

interfacial tension over an enormous range, independent of the properties of the substrate upon which it rests. Furthermore, this method avoids the use of toxic mercury and the ensuing modulation of surface tension is compatible with microfluidics.

2.2 Results

Figure 2.1A contains a series of images that illustrate how liquid metal alloys of gallium (here, eutectic gallium indium, 75 wt% Ga 25 wt% In)¹⁹ spread dramatically in electrolyte in response to modest voltages. Figure 2.1 reports the potentials relative to a saturated Ag/AgCl reference electrode in which the open circuit potential is approximately -1.5 V. Spreading occurs in a variety of electrolytes, over a wide range of pH (over all pH attempted from 0 to 14), with and without dissolved oxygen, over a range of electrolyte concentrations, and on a wide variety of substrates including glass, Teflon, polystyrene, and tungsten. The spreading observed here has been reported previously in the literature, but was attributed to electrocapillarity²⁰. We show here that the mechanism goes beyond electrocapillarity and the electrochemical formation of the surface oxide plays an essential role.

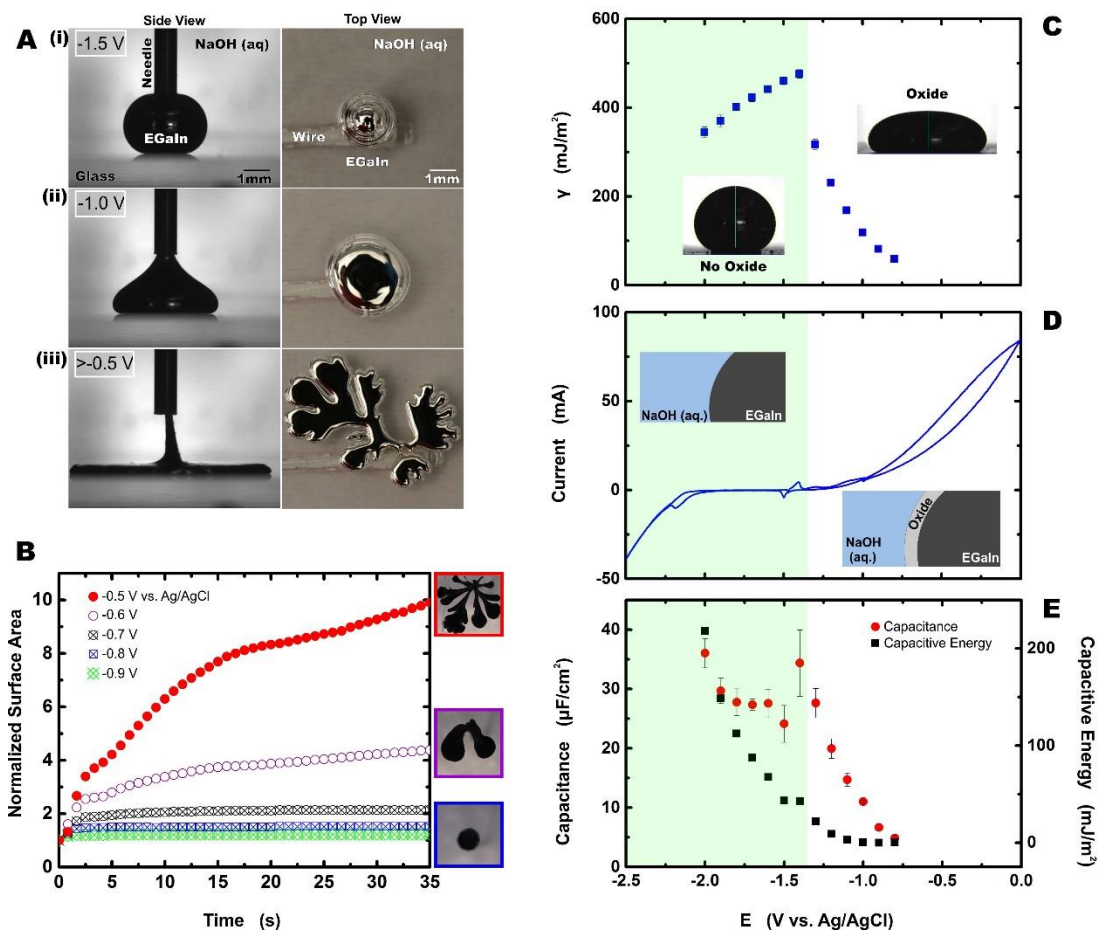


Figure 2.1: Spreading enabled by a surface oxide. (A) Oxidative spreading of a bead of liquid metal in 1M NaOH solution. A needle serves as a top electrical contact to the droplet in the left column, whereas a wire serves as a bottom electrical contact to the droplet in the right column. (i) The drop assumes a spherical shape initially due to its large surface tension; (ii) upon application of an oxidative potential, the metal assumes a new equilibrium shape; (iii) above a critical potential, the metal flattens and spreads without bound and ultimately forms fingering patterns that further increase its surface area and destabilize the metal; (B-D) The areal footprint of a drop of EGaIn as a function of time and potential identifies the critical potential above which spreading occurs without bound (solid circles) and below which the droplet adopts equilibrium shapes (hashed symbols). (C) An electrocapillary curve of EGaIn measured by sessile drop profile in 1 M NaOH; (D) A cyclic voltammogram of EGaIn. (E) The measured capacitance and calculated capacitive energy of EGaIn from impedance spectroscopy.

Figure 2.1B plots the areal footprint of a spreading EGaIn drop as a function of time and potential. The shape of the metal represents a balance between the interfacial tension and

gravity. Lower interfacial tensions therefore correspond with an increased areal footprint. Above a critical potential (≈ -0.6 V relative to a saturated Ag/AgCl reference electrode), the metal spreads initially as a disc that eventually breaks into a fingering morphology (Figure 2.1A(iii)) that continues to increase in area with respect to time until it becomes unstable and separates from the electrode entirely. Below this critical potential (i.e., at potentials that are less oxidative), the drop adopts equilibrium shapes, as indicated by the plateaus in the normalized area in Figure 2.1B.

The change in surface tension of a liquid drop with respect to potential—that is, electrocapillarity—has been used previously to alter the shape of liquid metals²¹ albeit less dramatically than that seen in Figure 2.1A. Electrocapillarity lowers the interfacial tension of the metal, γ , from its maximum value, γ_0 , due to capacitive effects arising from the potential, E , as shown in Equation 2.1²²,

$$\gamma = \gamma_0 - \frac{1}{2}C(E - E_{PZC})^2 \quad (2.1)$$

where C is the capacitance per unit area and E_{PZC} is the potential of zero charge. The potential of zero charge is the potential at which the excess surface charge is zero and the surface tension is at its maximum value. One implication of Equation 2.1 is that any change in potential from the E_{PZC} , whether positive or negative, will result in a symmetric decrease in the surface tension. In contrast, the spreading in Figure 2.1A only occurs at oxidative potentials. Normally, undesirable electrochemical reactions, such as electrolysis, limit electrocapillarity to a small range of potentials (E) and thus a modest range of interfacial tension, whereas here, the electrochemical reactions further lower the interfacial tension.

Figure 2.1C plots the interfacial tension of the metal measured by analyzing the shape of multiple sessile droplets (viewed from the side) versus potential. Between -2 V and -1.4 V, in the absence of the oxide or electrochemical reactions, a droplet of EGaIn behaves in a manner that is consistent with classic electrocapillarity. Fitting this portion of the curve yields a maximum surface tension of 509 mJ/m² and an E_{PZC} of -0.91 V, consistent with previous electrocapillary measurements²³. At potentials more oxidative than -1.4 V, the oxide layer begins to form on the surface²⁴, as confirmed by the cyclic voltammogram in Figure 2.1D. This oxidation causes a sudden and substantial drop in the surface tension, in spite of the decrease of measured capacitance and calculated capacitive energy over this potential range, as shown in Figure 2.1E.

The remarkable implication of the data summarized in Figure 2.1 is that the oxide layer acts like a ‘surfactant’ on the surface of the metal. In the absence of the oxide, the interfacial tension is large, as expected for a metal in contact with electrolyte. When the oxide forms, it replaces this high energy interface with two new interfaces: metal / metal-oxide and metal-oxide / electrolyte. Most oxides, including gallium oxide, form hydroxyl groups on their exterior surface, rendering them hydrophilic (confirmed by a near zero contact angle of water on the oxide surface). The interior of gallium oxide, however, consists of Ga atoms²⁵. The absence of any notable change in contact angle between the droplet and substrate during spreading and the independence of spreading relative to substrate composition further suggests spreading is due primarily to liquid metal / oxide / electrolyte interactions.

Oxygen adsorption is known to lower the interfacial tension of molten metals as a function of the partial pressure of oxygen²⁶. At partial pressures in which the oxide forms fully, the interfacial tension of the metal becomes challenging to measure because it is encased in an oxide with mechanical properties that prevent the liquid from adopting an equilibrium shape. Alloys of gallium are no exception; the oxide can stabilize the metal in non-equilibrium shapes²⁷ despite being quite thin (≈ 1 nm in dry air)^{25,28,29}. To achieve spreading, an electrochemical driving force is necessary. Although it is conceivable that spreading could be due to mechanical stresses arising from oxide growth, the ability of the drop to return to equilibrium shapes after physical perturbation at sub-critical potentials, the lack of hysteresis in the ‘electrocapillary’ curve, and the retardation of spreading by the formation of thicker oxides in pH neutral electrolytes suggest otherwise. In NaOH(aq.), dissolution of the oxide³⁰ competes with the electrochemical formation of the oxide³¹, which likely allows the metal to behave as a fluid with minimal mechanical hindrance.

The change in surface tension in response to potential is completely reversible, with limited hysteretic effects. **Figure 2.2** demonstrates the ability to reversibly and rapidly switch the interfacial tension over a large range by only varying the potential modestly in steps of 0.25 or 0.5 V. In each case, the drop returns to the expected interfacial tension in < 1 s, in spite of the kinetics of oxide growth and dissolution.

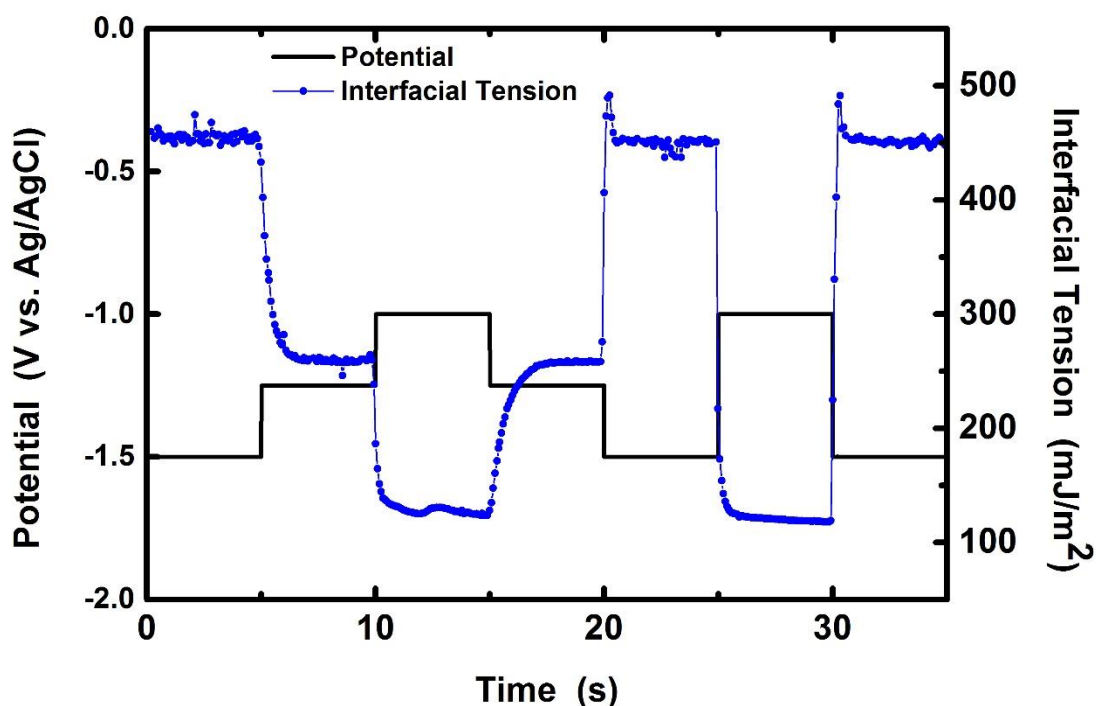


Figure 2.2: The interfacial tension of the metal may be tuned dramatically, rapidly, and reversibly in response to small changes in potential, as shown using multi-step chronoamperometry of a sessile EGaIn drop in 1 M NaOH. Increasing the electrochemical potential results in a corresponding decrease of the interfacial tension, consistent with the values in Figure 2.1C.

The interfacial tension undergoes a large step change when the oxide forms at -1.4 V, but continues to decrease with increased potential according to Figure 2.1C. The interfacial dynamic behavior in this regime is difficult to analyze, but the decrease in the measured capacitance values from -1.4 to -0.7 suggests that (1) electrocapillary behavior cannot solely explain the decrease in interfacial tension with respect to potential and (2) the effectiveness of the oxide for separating the electrolyte from the metal likely improves with respect to potential.

At potentials above the critical voltage (-0.6 V), two self-consistent observations suggest behavior resembling that of very low surface tension: (1) the area increases without bound until it becomes unstable, and (2) the interfacial tension projects toward zero at this critical voltage (cf., Figure 2.1C). It is difficult to measure the interfacial tension beyond -0.6 V because the metal spreads without ever reaching an equilibrium shape and sessile drop analysis poorly fits the resulting shape. To approximate the interfacial tension at potentials greater than -0.6 V, we use a scaling analysis based on the capillary length since the shape of the metal represents a balance between gravity and interfacial tension. Comparing the critical dimension (height) during spreading to the critical dimension at voltages of known tension provides an estimate, as described in the Materials and Methods section. First, comparing the capillary length of the oxide-coated metal when it is nearly spherical (-1.5 V) to when it spreads critically (-0.6 V) suggests the interfacial tension is ≈ 2 mN/m at -0.6 V. Likewise, comparing the capillary length of the oxide-coated metal at the last measureable point in Figure 2.1C (i.e., -0.7 V) to the critical voltage (-0.6 V) also suggests the interfacial tension is ≈ 2 mN/m at -0.6 V. Although these two values are above zero, we refer to them as ‘near zero’ since (1) the values are only estimates and are remarkably low considering the enormous tension of the bare metal, (2) the metal never reaches an equilibrium shape at this potential, and (3) the oxide may provide some minor mechanical impediment to spreading, in which case the liquid tension would be even lower.

The spreading of EGaIn at oxidative potentials can be exploited to manipulate the shape of the metal in both closed and open systems. For example, oxidative potentials can induce the metal to flow uphill into capillaries containing electrolyte, as shown in **Figure 2.3A**. Removal

of the oxide chemically or electrochemically reverses the direction of flow, making it possible to impart reversible flow. Likewise, the position of a counter-electrode in electrolyte directs the movement of the metal in an open channel, as shown in Figure 2.3B, since the spreading metal moves preferentially toward the counter electrode. Oxidative potentials can also cause the metal to form metastable fibers as it extrudes from a syringe, as shown in Figure 2.3D. In the absence of applied potential, metal pumped out of the end of a capillary forms beads that fall periodically due to the force of gravity, as shown in Figure 2.3C.

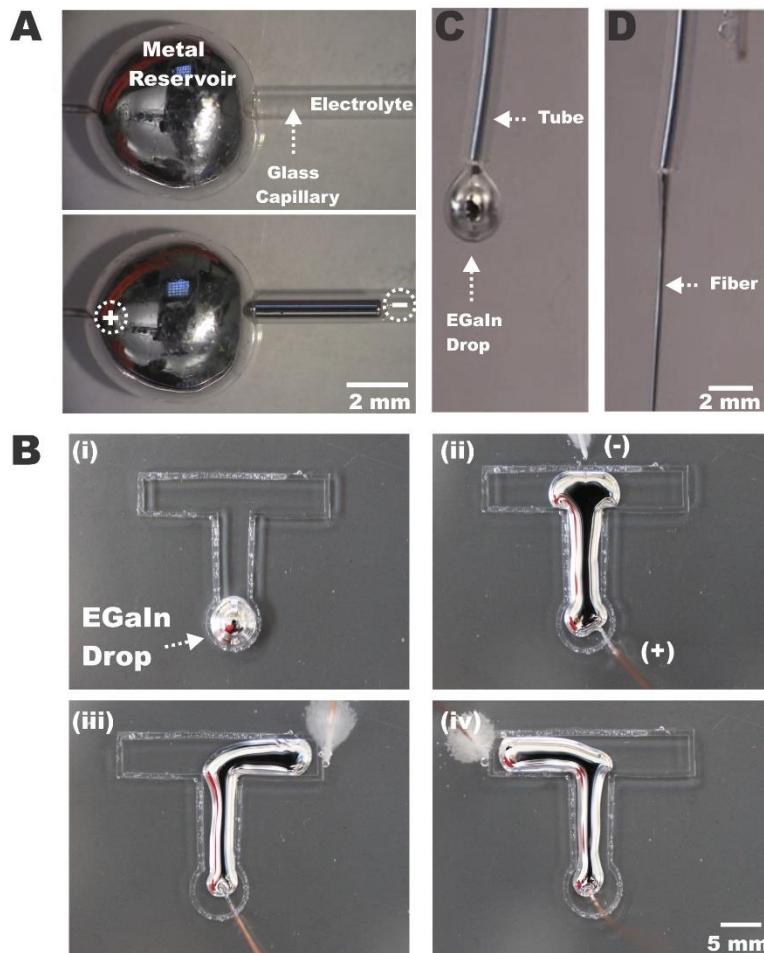


Figure 2.3: (A) Inducing liquid metal into an upward-tilted capillary channel (~0.9 mm ID) by application of a voltage in the presence of 1 M NaOH; (B) Controlling the shape and direction of a metal drop into an open T-shaped Plexiglas[®] channel submerged in 1 M NaOH solution using only voltage. Switching the position of the counter electrode at different points (ii-iv), guides the direction of the metal droplet; (C) Side view of a small droplet of EGaIn pumped out of a 0.5 mm ID polymer tube at 20 mL/hr in 1 M NaOH. The metal forms droplets in the absence of potential; (D) Formation of an oxide coated liquid metal fiber coming out of the tube at 5 V.

It is also possible to remove the oxide skin using modest reductive potentials (e.g., -1 V applied) to return the metal to a state of large interfacial tension, induce capillary behavior, change the contact angle, and alter the rheological properties on demand; we call this behavior

recapillarity (reductive capillarity). Prior to reduction, the oxide layer stabilizes the metal droplet in a non-equilibrium shape and gives it non-Newtonian rheological properties³². In the absence of the stabilizing skin, the metal becomes Newtonian, decreases its footprint, and increases its contact angle (**Figure 2.4A**). The experiments reported in Figure 2.4 began by placing a droplet of the metal on a dry glass substrate before submerging the substrate in pH neutral electrolyte. The presence of the oxide causes the drop to pin to the dry substrate and allows the drop to be physically manipulated to a low initial contact angle prior to applying potential. The ability to mechanically manipulate the contact angle is indicative of the hysteretic nature of the wetting of the oxide-coated metal on dry surfaces³³. Removing the oxide allows the metal to dewet the substrate and return to an equilibrium contact angle. Recapillarity can turn on or off this dewetting process by removing the oxide in pH neutral solutions. Dewetting can occur asymmetrically by removing oxide preferentially from one side of the drop. Figure 2.4B shows sequential images of a drop of metal in which the contact angle changes asymmetrically from 31 to 86 to 124 degrees incrementally by inducing recapillarity in discrete steps on one side of the drop. The contact angle on the other side of the drop increases due to the combination of conservation of mass in the drop and the ability of the underlying oxide to pin the drop to the substrate.

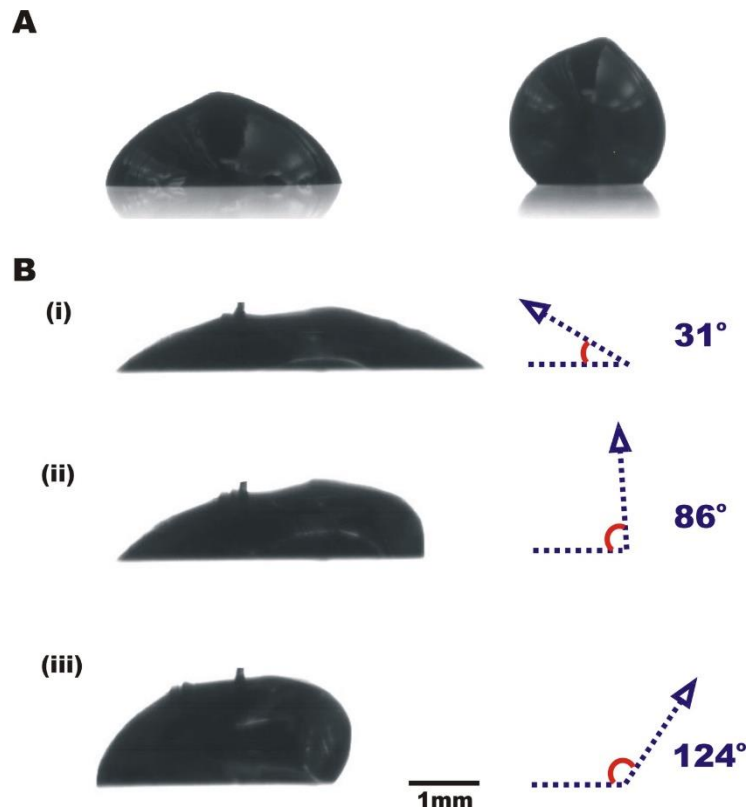


Figure 2.4: ‘Recapillarity’ can manipulate the shape and local contact angle of droplets placed on dry substrates. (A) Electrochemical reduction of the oxide on a droplet of liquid metal supported by a glass slide causes the metal to bead up. Removal of the electrode prior to imaging creates the lobe on the top of the drop; (B) Three sequential side views (i-iii) of an EGaln drop that asymmetrically dewets a glass slide in DI water upon application of reductive potentials relative to a counter electrode placed on the right side of the drop. Recapillarity causes the metal to move away from the anode, which is outside the frame of the image. The cathode gently touches the top of the drop to minimize perturbation of the shape of the metal.

In the absence of potential, the oxide mechanically stabilizes the metal in microchannels (**Figure 2.5B**). The adhesion of the oxide to the walls of dry channels makes it difficult to remove the metal by pressure differentials without leaving residue³⁵. In contrast, recapillarity induces liquid metal to withdraw controllably, smoothly, and rapidly (up to 20 cm/s) from microchannels via capillary action without leaving metal and oxide residue (Figure

2.5). The use of a pH-neutral electrolyte (NaF) ensures that segments of the metal that are not in the electrical path remain stable because of the presence of oxide skin (Figure 2.5C).

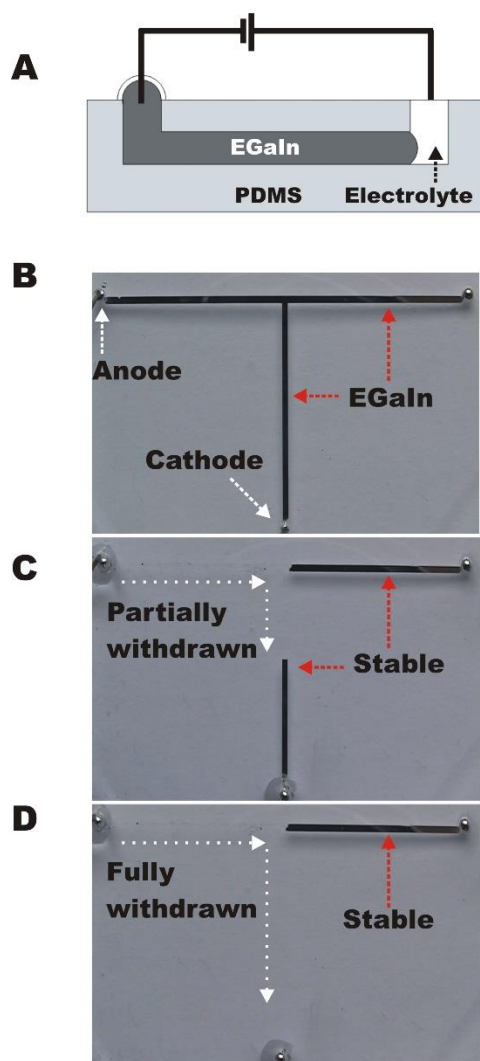


Figure 2.5: Recapillarity-induced withdrawal of liquid metal from microchannels. (A) The electrochemical reduction of gallium oxide in pH-neutral electrolyte induces retreat of the metal from the channel by applying a reductive potential; (B) Top-down photograph of a T-shaped microfluidic channel. (1 mm wide, 100 μm tall, 65 mm long horizontally) The surface oxide stabilizes the liquid metal in the channel; (C) A reductive bias (-1 V) applied to the metal relative to a drop of electrolyte (0.01 M NaF) at the anode removes the oxide and the liquid metal retreats toward the cathode; (D) The metal continues to withdraw until the applied voltage ceases. Metal that is not in the electrical pathway remains stable.

This chapter demonstrates that surface oxides behave as excellent surfactants for metals and may be removed or deposited to rapidly and reversibly tune the interfacial tension of a low-toxicity liquid metal from $\approx 500 \text{ mJ/m}^2$ to near zero using modest voltages. This capability enables new types of electrohydrodynamic phenomena to manipulate the shape of metal, which is attractive for a wide range of applications including MEMS switches and conductive micro-components³⁵, microactuators and pumps³⁶, adaptive electronic skins³⁷, tunable antennas and apertures^{38,39}, fluidic optical components and displays^{40,41}, field-programmable circuits⁴², and metamaterials with reversible cloaking. The necessity of electrolyte and the reliance on electrochemical reactions may present some practical limitations for long term switchability, although batteries operate with similar restrictions. The spreading behavior induced by a surface oxide provides the most significant evidence to date that buried oxide interfaces—which exist ubiquitously on most metals and semiconductors, yet are difficult to probe—lower interfacial energy of the underlying substrate significantly. The ability to rapidly remove and deposit oxides on a wide range of materials may enable new methods to control interfacial phenomenon on both liquids and solids.

2.3 Materials and Methods

2.3.1 Electrochemical Experiments

Electrochemical measurements (i.e., cyclic voltammetry and electrochemical impedance spectroscopy) were made using a Bio-Logic SP-200 potentiostat. A saturated Ag/AgCl reference electrode and a platinum mesh counter-electrode were used in all of the experiments, with copper acting as the connection to the EGaIn (purchase from Indium

Corporation and 5N) working electrode. Copper was chosen because it makes excellent electrical contact with EGaIn. X-ray photoelectron spectroscopy measurements detected no copper at the interface of EGaIn / electrolyte after exposing the EGaIn to the copper wire. Care was taken to minimize or eliminate the exposure of the copper electrode to the solution. In experiments in which the copper was exposed, there was no measurable effect on the interfacial tension at each potential. Unless otherwise stated, all experiments took place in 1 M NaOH.

2.3.2 Area Measurements

EGaIn drops of approximately 30 μL were placed in a plastic petri dish filled with 1 M NaOH. A copper wire was connected to the top of the drop, and a video camera was placed underneath the transparent petri dish. Oxidative potentials were applied from -1.4 V to -0.5 V vs. the reference electrode (placed ≈ 5 cm away from the liquid metal), in 100 mV increments. A camera filmed the drop for 2 min after each incremental change in voltage, or until it separated from the copper wire due to excessive spreading. The images were then analyzed in ImageJ to determine the areal footprint, as illustrated in **Figure 2.6**.

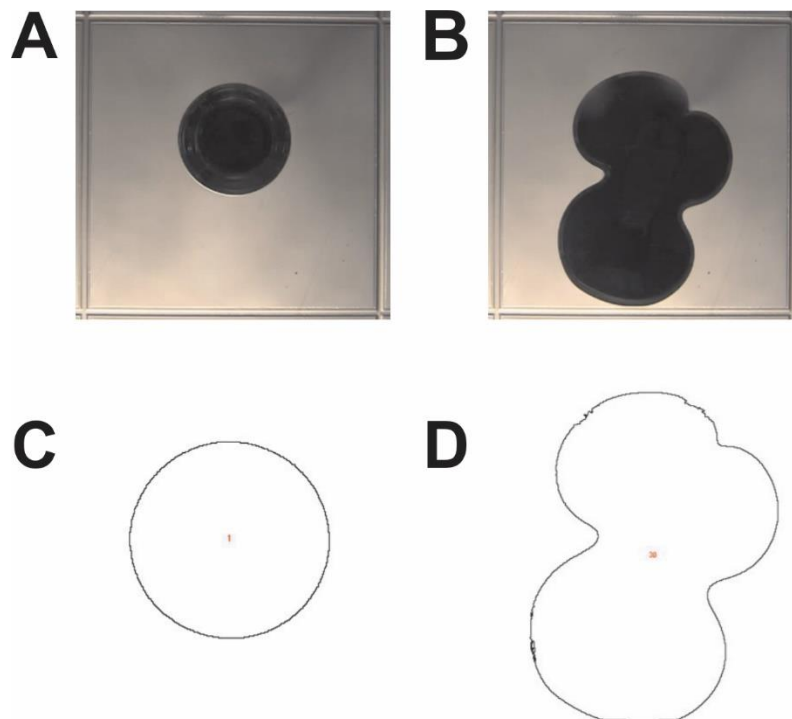


Figure 2.6: (A) Photograph of the bottom of a drop of EGaIn taken before applying a potential; (B) Photograph of the bottom of the same drop of EGaIn several seconds after applying 900 mV relative to the open circuit potential; (C-D), ImageJ outlines of the EGaIn drop used to estimate the area.

2.3.2 Interfacial Tension Measurements

The interfacial tension was determined as a function of potential by using the potentiostat in conjunction with a goniometer (First Ten Angstroms 1000B). Sessile droplets of EGaIn, ranging in volume from 25-50 μL , were placed on the tip of a small, exposed copper wire (**Figure 2.7**). The goniometer determined the volume and the interfacial tension and surface area as a function of voltage. The potential was increased in increments of 100 mV from -2 V to -0.8 V vs. the reference electrode. At potentials more negative than -2 V, bubbles formed rapidly on the surface of the EGaIn from reductive electrolysis of water. At potentials more positive than -0.7 V, the shape of the EGaIn drop flattened to such an extent that

interfacial tension could no longer be estimated using the goniometer, although the metal did continue to spread until it disconnected from the electrode.

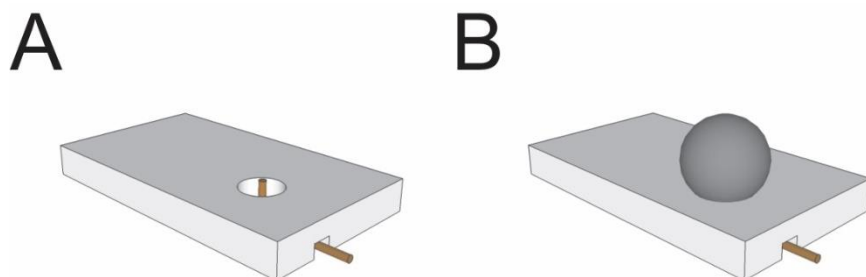


Figure 2.7: Schematic depicting the acrylic sheet used to secure a copper wire. (A) A 1 mm diameter hole was cut in the acrylic using a Universal VLS3.50 laser cutter. An insulated copper wire was secured using a photocurable resin; (B) Drops of EGaIn were placed on top of the hole with the wire extended $\approx 100 \mu\text{m}$ beyond the plane of the surface to avoid distorting the shape of the drop.

2.3.4 Capacitance Measurements

The capacitance was measured by electrochemical impedance spectroscopy. An EIS scan was performed at each potential used in the interfacial tension measurements, from 200 kHz to 1 Hz. Fitting software determined the double-layer capacitance from the resulting Nyquist plots (examples of which can be seen in **Figure 2.8**). This fitting was accomplished by assuming a solution resistance in series with an interfacial resistance and a constant phase element in parallel. For the region where no oxide was present (shaded region of Fig. 1C), the interfacial resistance was necessary to adequately fit the low frequency end of the spectrum (down to 1 Hz). However, the high frequency region (10^2 - 10^4 Hz)—where double-layer capacitance dominates the response—could be fit satisfactorily with a simple solution

resistance and constant phase element in series with minor change in the capacitance values. For the potential region where the oxide layer was present, the model was fit only to the high frequency capacitive region, while the low-frequency end that reflects more complicated chemistry, e.g., adsorption of hydroxyl ion^{43,44}, was not analyzed in the present work. The specific capacitance was determined by dividing the capacitance by the surface area determined by the goniometer at each potential. Although we assumed pseudo steady-state growth of the oxide layer, we ascertained similar Nyquist plots and capacitance values to those given by MacDonald et al⁴³ for Al (a metal from the same column of the periodic table that also forms a passivating oxide) over the entire range of potentials.

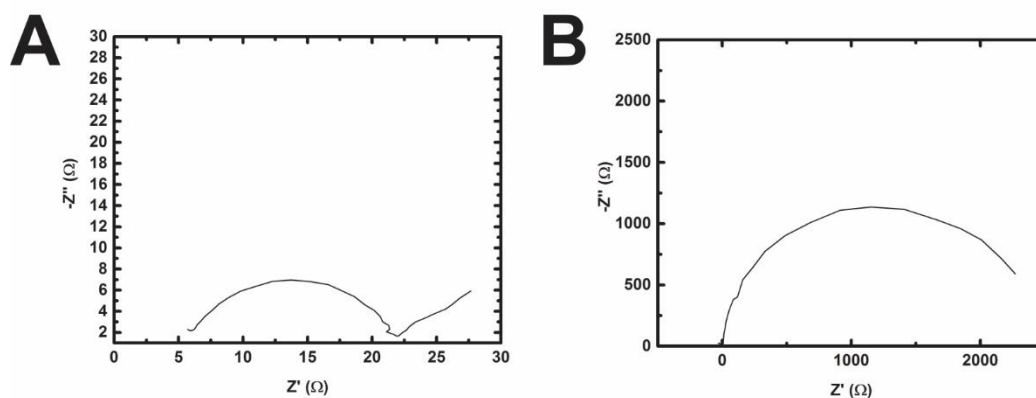


Figure 2.8: (A) Nyquist plot of EGAIn drop at -1.2 V vs. Ag/AgCl and (B) -1.9 V vs. Ag/AgCl.

The capacitive energy (U) was calculated by first estimating the potential (E) relative to the potential of zero charge (E_{pzc}), determined from Fig. 1C, and using the equation $U = \frac{1}{2} C(E - E_{pzc})^2$. The capacitance values obtained from a best fit of the shaded region of Figure 2.1C—approximately $C = 27 \mu\text{F}/\text{cm}^2$ —agreed with the values measured directly via impedance spectroscopy at reducing potentials (Figure 2.1E).

2.3.5 Reversibility Measurements

We measured the interfacial tension of the metal after stepping the voltage up and down several times. These reversibility measurements were performed by multi-step chronoamperometry in the same setup described previously to measure interfacial tension (i.e., sessile drop). In this case, the potential was varied between -1.5, -1.25, and -1.0 V vs Ag/AgCl, and held at each potential for 5 seconds while measuring continuously the interfacial tension of a sessile drop.

2.3.6 Capillary Length

To estimate the interfacial tension beyond the measuring capability of our instruments (i.e., at voltages greater than or equal to the critical voltage of -0.6 V, at which point the metal spreads dramatically), a scaling analysis based on the capillary length of the drop was used. The capillary length is based on a ratio between gravitational and interfacial forces, as shown in Equation 2.2,

$$L = \sqrt{\frac{\gamma}{\rho g}} \quad (2.2)$$

where L is the characteristic capillary length, ρ is the density of the EGaIn, and g is the acceleration due to gravity. We used the ratio of capillary lengths to estimate the interfacial tension relative to a known value, as shown in Equation 2.3

$$\frac{L_2}{L_1} = \frac{\sqrt{\frac{\gamma_2}{\rho g}}}{\sqrt{\frac{\gamma_1}{\rho g}}} \quad (2.3)$$

where the subscripts 2 and 1 represent droplets at two different potentials. Algebraic rearrangement yields Equation 2.4

$$\gamma_2 = \gamma_1 \left(\frac{L_2}{L_1} \right)^2 \quad (2.4)$$

When the drop is roughly spherical (at -1.5 V), $\gamma_1 = 330$ mN/m and the characteristic length is the radius ($L_1 = 2$ mm). When the droplet spreads dramatically (greater than -0.6 V), the capillary length is half the thickness (estimated to be $L_2 = 0.15$ mm based on a >10x increase in areal footprint, according to Figure 1). Using this scaling, $\gamma_2 \approx 2$ mN/m. Repeating this analysis,

but using the last measurable tension (-0.7 V), $\gamma_1 = 49$ mN/m and the characteristic length is half the height ($L_1 = 0.8$ mm). Using this scaling, $\gamma_2 \approx 2$ mN/m.

2.4 Acknowledgements

The authors acknowledge support from NSF CAREER (CMMI-0954321) and Research Triangle NSF MRSEC on Programmable Soft Matter (DMR-1121107). The authors are also grateful for helpful conversations with D. McDonald and M. Chaudhury and for the help of Chris Trlica preparing Figure 2.3A and David Phipps preparing Figure 2.1B.

2.5 References

1. Kataoka DE, Troian SM (1999) Patterning liquid flow on the microscopic scale. *Nature* 402:794–797.
2. Daniel S, Chaudhury MK, Chen JC (2001) Fast Drop Movements Resulting from the Phase Change on a Gradient Surface. *Science* 291:633–636.
3. Ichimura K, Oh SK, Nakagawa M (2000) Light-driven motion of liquids on a photoresponsive surface. *Science* 288:1624–1626.
4. Gallardo BS et al. (1999) Electrochemical principles for active control of liquids on submillimeter scales. *Science* 283:57–60.
5. Zhao B, Moore JS, Beebe DJ (2001) Surface-Directed Liquid Flow Inside Microchannels. *Science* 291:1023–1026.
6. Chaudhury MK, Whitesides GM (1992) How to Make Water Run Uphill. *Science* 256:1539–1541.

7. Lahann J et al. (2003) A reversibly switching surface. *Science* 299:371–374.
8. Rogers JA, Someya T, Huang Y (2010) Materials and Mechanics for Stretchable Electronics. *Science* 327:1603–1607.
9. Bauer S et al. (2014) 25th Anniversary Article: A Soft Future: From Robots and Sensor Skin to Energy Harvesters. *Adv Mater* 26:149–162.
10. Ozbay E (2006) Plasmonics: Merging Photonics and Electronics at Nanoscale Dimensions. *Science* 311:189–193.
11. Monat C, Domachuk P, Eggleton BJ (2007) Integrated optofluidics: A new river of light. *Nat Photonics* 1:106–114.
12. Schurig D et al. (2006) Metamaterial Electromagnetic Cloak at Microwave Frequencies. *Science* 314:977–980.
13. Stone HA, Stroock AD, Ajdari A (2004) Engineering Flows in Small Devices. *Annu Rev Fluid Mech* 36:381–411.
14. Ramos A (2011) *Electrokinetics and Electrohydrodynamics in Microsystems* (Springer Wien, New York).
15. Prins MWJ, Welters WJJ, Weekamp JW (2001) Fluid control in multichannel structures by electrocapillary pressure. *Science* 291:277–280.
16. Beni G, Hackwood S, Jackel JL (1982) Continuous electrowetting effect. *Appl Phys Lett* 40:912–914.
17. Sen P, Kim C-J (2009) A Fast Liquid-Metal Droplet Microswitch Using EWOD-Driven Contact-Line Sliding. *J Microelectromechanical Syst* 18:174–185.

18. Liu Y, Jessop PG, Cunningham M, Eckert CA, Liotta CL (2006) Switchable Surfactants. *Science* 313:958–960.
19. Dickey MD et al. (2008) Eutectic Gallium-Indium (EGaIn): A Liquid Metal Alloy for the Formation of Stable Structures in Microchannels at Room Temperature. *Adv Funct Mater* 18:1097–1104.
20. Tsai JTH, Ho C-M, Wang F-C, Liang C-T (2009) Ultrahigh contrast light valve driven by electrocapillarity of liquid gallium. *Appl Phys Lett* 95:251110.
21. Keizer J, Rock PA, Lin S-W (1979) Analysis of the oscillations in “beating mercury heart” systems. *J Am Chem Soc* 101:5637–5649.
22. Grahame DC (1947) The Electrical Double Layer and the Theory of Electrocapillarity. *Chem Rev* 41:441–501.
23. Frumkin A, Polianovskaya N, Grigoryev N, Bagotskaya I (1965) Electrocapillary phenomena on gallium. *Electrochimica Acta* 10:793–802.
24. Perkins RS (1972) Gallium Oxidation in Alkaline Solution. *J Electrochem Soc* 119:713–715.
25. Regan MJ et al. (1997) X-ray study of the oxidation of liquid-gallium surfaces. *Phys Rev B Condens Matter* 55:10786–10790.
26. Egry I, Ricci E, Novakovic R, Ozawa S (2010) Surface tension of liquid metals and alloys - Recent developments. *Adv Colloid Interface Sci* 159:198–212.
27. Ladd C, So J-H, Muth J, Dickey MD (2013) 3D Printing of Free Standing Liquid Metal Microstructures. *Adv Mater* 25:5081–5085.

28. Regan MJ et al. (1997) X-ray reflectivity studies of liquid metal and alloy surfaces. *Phys Rev B* 55:15874–15884.
29. Cademartiri L et al. (2012) Electrical Resistance of Ag-TS-S(CH₂)(n-1)CH₃//Ga₂O₃/EGaIn Tunneling Junctions. *J Phys Chem C* 116:10848–10860.
30. Pourbaix M (1974) *Atlas of Electrochemical Equilibria in Aqueous Solutions* (Natl Assn of Corrosion, TX, USA) Second English Edition.
31. Hurlen T (1964) Anodic dissolution of liquid gallium in alkaline solutions. *Electrochimica Acta* 9:1449–1452.
32. Xu Q, Qudalov N, Guo Q, Jaeger H, Brown E (2012) Effect of oxidation on the Mechanical Properties of Liquid Gallium and Eutectic Gallium-Indium. *Phys Fluids* 24:063101.
33. Doudrick K et al. (2014) Different Shades of Oxide: From Nanoscale Wetting Mechanisms to Contact Printing of Gallium-Based Liquid Metals. *Langmuir* 30:6867–6877.
34. Giguere PA, Lamontagne D (1954) Polarography with a dropping gallium electrode. *Science* 120:390–391.
35. Sen P, Kim C-J (2009) Microscale Liquid-Metal Switches -A Review. *IEEE Trans Ind Electron* 56:1314 –1330.
36. Tang S-Y et al. (2014) Liquid metal enabled pump. *Proc Natl Acad Sci* 111:3304.
37. Hammock ML, Chortos A, Tee BC-K, Tok JB-H, Bao Z (2013) 25th Anniversary Article: The Evolution of Electronic Skin (E-Skin): A Brief History, Design Considerations, and Recent Progress. *Adv Mater* 25:5997–6038.

38. So JH et al. (2009) Reversibly Deformable and Mechanically Tunable Fluidic Antennas. *Adv Funct Mater* 19:3632–3637.
39. Khan MR, Hayes GJ, So J-H, Lazzi G, Dickey MD (2011) A frequency shifting liquid metal antenna with pressure responsiveness. *Appl Phys Lett* 99:013501–3.
40. Heikenfeld J, Drzaic P, Yeo J-S, Koch T (2011) Review Paper: A critical review of the present and future prospects for electronic paper. *J Soc Inf Disp* 19:129–156.
41. Krupenkin T, Yang S, Mach P (2003) Tunable liquid microlens. *Appl Phys Lett* 82:316–318.
42. Cumby BL et al. (2012) Reconfigurable liquid metal circuits by Laplace pressure shaping. *Appl Phys Lett* 101:174102.
43. Macdonald DD, Real S, Smedley SI, Urquidi-Macdonald M (1988) Evaluation of Alloy Anodes for Aluminum-Air Batteries IV . Electrochemical Impedance Analysis of Pure Aluminum in at 25°C. *J Electrochem Soc* 135:2410–2414.
44. deWit JHW, Lenderink HJW (1996) Electrochemical Impedance Spectroscopy as a tool to obtain mechanistic information on the passive behaviour of aluminium. *Electrochimica Acta* 41:1111–1119.

Chapter 3

Oxide-Mediated Fingering Instabilities in Liquid Metals

3.1 Introduction

Fingering patterns in spreading materials arise via a number of different mechanisms: viscous fingering and diffusion limited aggregation¹⁻⁶, directional solidification^{7,8}, Marangoni-driven spreading^{9,10}, and even in zero-surface tension granular¹¹ and ordinary¹² fluids. Here, we demonstrate an additional fingering mechanism by which liquid metals can form branched, lobed structures via an oxidative reaction. Liquid metals are of interest because of their metallic electrical, thermal, and optical properties. Liquid metals might seem an unlikely candidate to undergo instabilities because they have the largest known surface tension of any room-temperature fluid. However, gallium-based liquid metals, such as eutectic gallium indium (EGaIn), have been shown to approach near zero surface tension via surface oxidation¹³. In the presence of aqueous solutions, applying an oxidative electrochemical potential to the alloy drives surface oxidation. In the absence of the oxide, the metal has an enormous surface tension. The deposition of this oxide can drastically lower the alloy's surface tension (from ~ 500 mN/m to near zero over less than 1 V applied), which enables instabilities in this otherwise stable liquid. This sudden drop in surface tension is not due primarily to classic electrocapillarity, but instead due to the oxide acting like a surfactant. This chapter studies the dynamics of the instabilities of the metal as it approaches zero surface tension and shows that, beyond a threshold potential, the instabilities can be suppressed.

Here, we characterize oxide-mediated fingering instabilities of EGaIn in an alkaline solution driven by an applied electric potential. Under sufficient oxidative potential, EGaIn

demonstrates behavior consistent with fractal-like growth and is visually similar to Hele-Shaw flow^{14,15}. Rather than arising through the injection of fluid at constant flux of pressure, these instabilities occur with an unconfined constant-volume droplet in solution. Furthermore, in conventional Hele-Shaw systems, the instabilities occur in the less viscous of the two fluids. However, in this system, EGaIn is approximately twice as viscous as the surrounding fluid when instabilities develop. **Figure 3.1a** shows an example of the fractal morphology the liquid metal can exhibit. Although the morphology appears similar to viscous fingering, the fractal dimension of the droplet ($D = 1.30 \pm 0.05$) indicates that a different phenomenon is causing the instabilities in EGaIn.

The instabilities are present within an intermediate range of oxidative potentials. If the electric potential (ε) is below a critical value, the interfacial tension is large enough that the droplet maintains a spherical shape. If ε is too large, the surface oxide grows thick enough to effectively behave as a mechanical shell that is strong enough to suppress the growth of instabilities. Thus, the same surface oxide which destabilizes the droplet, allowing spreading, can also re-stabilize it in a new equilibrium. In this chapter, we explore the regimes characterizing the different exhibited morphologies and the phase diagram boundaries between them, and we find a scaling collapse for droplets of different sizes. Finally, we provide a semi-quantitative treatment of key forces which determine the regime boundaries.

3.2 Methods and Materials

Apparatus: Our experimental apparatus, shown schematically in **Figure 3.1a**, consists of a horizontal container filled with 1 M sodium hydroxide (NaOH) to provide active

dissolution of the oxide layer and increase the ionic strength relative to de-ionized water. The container is a transparent sheet of poly(methyl methacrylate), the walls of the cylindrical container are lined with a copper counter-electrode with a diameter of 152 mm and the top surface open to the atmosphere. Experiments take place in a fluid layer of depth 10.5 ± 0.5 mm, sufficient to allow full submersion of an EGaIn droplet placed at the center. The entire apparatus is placed on a leveling table to minimize gravitational gradients, and is lit from below by a diffuse light source. Video imaging of the apparatus is done with a video camera (frame rate 29.97 Hz) mounted directly above the apparatus.

Electrical measurements: A three-electrode setup is used in conjunction with a Gamry Reference 600 potentiostat to both set the electric potential (ϵ) and measure the resulting current $I(t)$. This setup consists of a working, counter, and reference electrode. The liquid metal serves as the working electrode, and is connected to the potentiostat through a copper wire fixed in a 1 mm diameter hole directly underneath the metal droplet; the reference electrode, a saturated Ag/AgCl electrode, is positioned in the solution approximately 9 cm from the working electrode. To ensure a uniform, symmetric electric field around the droplet, a copper ring of 7.6 cm inner radius (R_{elec}) and 8.6 cm outer radius (R_{outer}) is fixed to the apparatus and utilized as a counter-electrode. The sampling frequency of the current is set to match the camera frame rate.

EGaIn Properties: We perform all of our experiments on EGaIn, a liquid metal comprised of 75 wt% gallium and 25 wt% indium, with a density of 6250 kg/m^3 , a viscosity of 2×10^{-2} Poise (approximately twice that of the electrolyte solution), and a surface tension of

470 mN/m in 1 M NaOH at the open circuit potential (approximately -1.5 V vs. reference electrode).

Data collection: We varied ε for EGaIn droplets of four different volumes: 3 μL , 10 μL , 30 μL , and 100 μL . Each droplet is dispensed and measured by a First Ten Angstroms 1000B contact angle goniometer. We report ε with respect to the reference electrode, with values ranging from -0.8 V to 4.0 (V vs. Ag/AgCl), applied in 100 mV increments. While we report the absolute value of the potential with respect to the reference, all calculations utilizing the potential are performed by adding 1.5 V to obtain the net applied potential. For every run, the potential is maintained for approximately 60 seconds; new runs begin after the oxide has dissolved and the droplet has returned to its open circuit potential equilibrium shape. The experiment is repeated for three to five trials for each electric potential to ensure consistency. New droplets are used for each value of electric potential. Gas bubbles form around the counter electrode at larger applied potential, and are removed from the electrode before new runs. To perform morphological measurements, we binarize all images by thresholding at mean value and calculate the droplet cross-sectional area $A(t)$.

Oxide Thickness: In the course of our analyses, it will become important to estimate the thickness of the oxide layer. We assume that the rate of oxide growth (but not the dissolution rate) depends on the applied potential. To estimate this rate, and therefore the oxide thickness, we simultaneously record the droplet cross-sectional area and the current of the oxidation reaction. From these variables, we model the oxide thickness as a function of time, volume, and voltage.

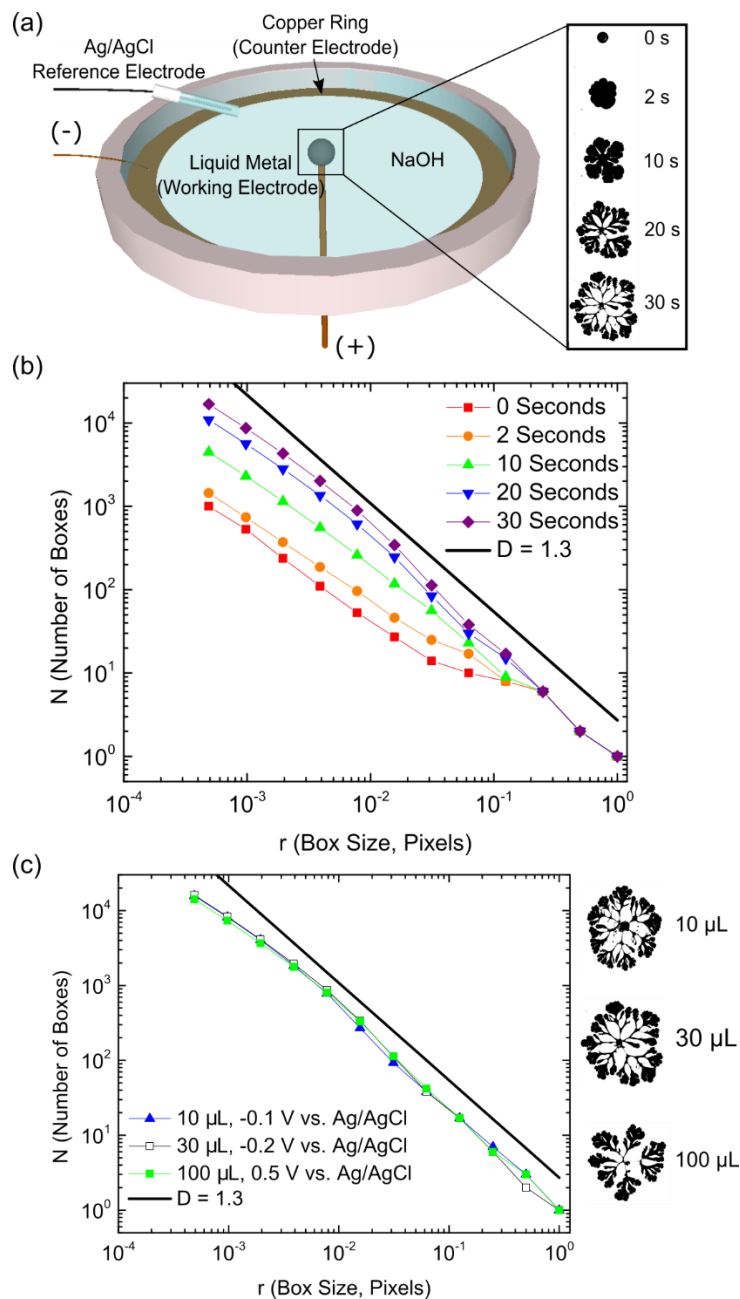


Figure 3.1: (a) Schematic of apparatus, and experimental images showing evaluation of fingering instability of liquid metal. (b) Box-counting plot for a 30 μL droplet of EGaln spreading with -0.2 V vs Ag/AgCl applied potential (shown in (a)). (c) Box-counting plot of droplets with $V = 10\ \mu\text{L}$, $30\ \mu\text{L}$, and $100\ \mu\text{L}$, analyzed immediately before first branch break-off.

3.3 Results

3.3.1 Droplet Morphology

For $\varepsilon > -0.5$ V, we observe that the droplets spread with a fractal-like morphology. As shown in Figure 3.1a, the initially spherical droplet becomes increasingly branched as it spreads outwards, with the first undulations appearing about 2 seconds after the potential is first applied. Over the next ~ 30 seconds, the droplet develops undulations and branches covering several orders of magnitude in size. At longer times, the droplet reaches a maximum surface area as the branches of the liquid metal become so thin that they pinch off from the main droplet.

To test for self-similarity, we use a box-counting algorithm¹⁶ to measure the Hausdorff Dimension (D)

$$D = \lim_{r \rightarrow 0} \frac{\log(N)}{\log(1/r)} \quad (3.1)$$

where r is the size of the boxes used to cover the surface, and N is the number of boxes necessary to perform the covering. As the droplet spreads, D asymptotically approaches a value of 1.30 ± 0.05 , as shown by the solid line in Figure 4.1b. The same fractal dimension is observed for $V = 10 \mu\text{L}$, $30 \mu\text{L}$, and $100 \mu\text{L}$ droplets, as shown in Figure 4.1c, measured immediately before the liquid disconnects from the electrode (at its maximum area). This indicates that this new fingering phenomenon belongs to a different universality class than radial viscous fingering in Hele-Shaw cells and diffusion-limited aggregation^{6,17}, which have a fractal dimension of $D = 1.713 \pm 0.003$.

Across the range of (ϵ , V) values tested, we observed four distinct regimes, which we describe below by the designations A-D. **Figure 3.2** shows representative images and dynamics for each regime. We differentiate among the regimes via three visual features of the droplet – smooth, undulated, and branched – as well as whether spreading and/or contraction were observed. In the descriptions below, smooth refers to droplets which maintain a spherical cap shape (regime A,D) undulated refers to undulations around the perimeter (regime B,C) and branched refers to the presence of thinned structures that connect the electrode to fingers further away (regime B). In all cases, the droplet volume V is conserved; any increases in area A are accompanied by an unquantified decrease in droplet thickness h . The potential in each regime is sufficient to cause surface oxidation (i.e. $\epsilon > -1.4$ V).

Regime A is characterized by smooth droplets that remain shiny in appearance (are free of any visual traces of the oxide.) The droplet area A spreads by up to 50-100% before equilibrating at a final size which is stable to mechanical perturbations.

Regime B droplets area almost immediately unstable to undulations along the perimeter of the droplet. These undulations simultaneously become deeper (extending back to the center electrode) and develop secondary, tertiary, etc. undulations of their own. Together, these two processes form the fractal morphology characterized in Figure 3.1 and can spread by more than 200 times their initial area. The droplet loses some of its shininess during this process, particularly around the droplet perimeter. Eventually, the droplet spreads and thins to the point where one or more branches pinch off into small satellite droplets. If these satellite droplets lose their electrical contact, then their oxide layer re-dissolves, they become shiny in appearance, and their (now high) surface tension causes the liquid to retract back to a spherical

shape. If the satellite droplets happen to re-attach to the electrode, they can begin spreading again from this new site.

Regime C dynamics proceed as in regime B, but the growth of the undulations is interrupted after a few seconds and they do not themselves become unstable to secondary undulations. In this regime, the branching effect is diminished or not present at all. The droplet eventually begins to contract over time rather than expanding outwards. Figure 3.2b captures this contraction. After reaching a peak at approximately 10 seconds, the droplet area begins to decrease.

In regime D, the droplet spreads rapidly, but the oxide layer grows thick enough to prevent further spreading, and ultimately begins to contract. This size decrease correlates with a sudden change in system resistance ($\Omega = (\varepsilon + 1.5V)/I$) as seen in Figure 3.2c. After 1-2 seconds, regime D shows a sharp spike in the resistance, which can be attributed to both the decrease in surface area and to the charge transfer resistance provided by the growing oxide layer.

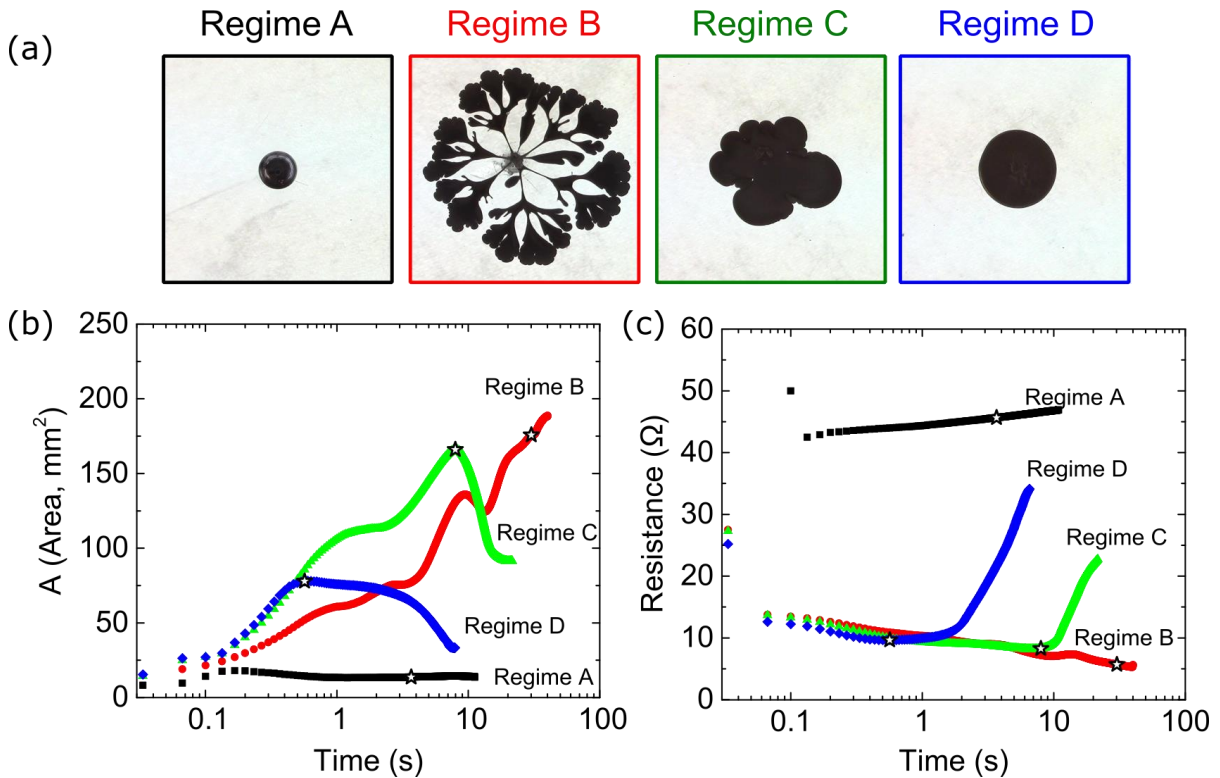


Figure 3.2: (a) Representative images taken at the maximum area for all four regimes, and their dynamics characterized by (b) area $A(t)$ and (c) the electrical resistance measured from from $(\varepsilon + 1.5 \text{ V})/I(t)$. The star indicates the time at maximum area. All panels show data from the same 4 trials with $V = 30 \mu\text{L}$ and $\varepsilon = -0.7 \text{ V}$ (regime A); $\varepsilon = 0.3 \text{ V}$ (regime B); $\varepsilon = 1.3 \text{ V}$ (regime C); $\varepsilon = 2.5 \text{ V}$. All potentials relative to a Ag/AgCl reference electrode.

We characterize each of the four trials into one of these four regimes and plot a phase diagram as a function of (ε, V) . As shown in **Figure 3.3**, at each volume V , there is a progressive regime $A \rightarrow B \rightarrow C \rightarrow D$ as ε increases. While the phase boundary between regimes A and B is vertical, the other boundaries are tilted so that they occur at larger ε as the droplet volume increases. This volume-dependence arises from the corresponding decrease in the surface area to volume ratio, as will be discussed below.

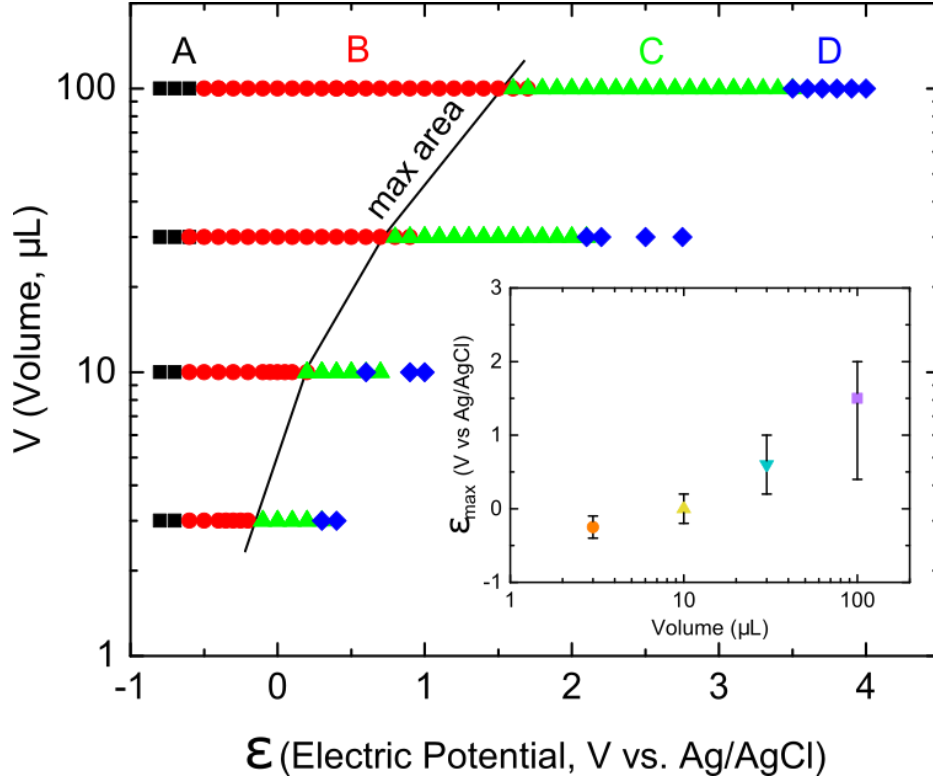


Figure 3.3: Phase diagrams for droplets of volume V subject to an applied electric potential ε . The solid black line corresponds to the peak \tilde{A} in Figure 3.4. The inset represents the potential ε_{\max} at which the maximum in Figure 3.4a occurs, as a function of droplet volume (on a logarithmic scale). Error bars represent the width ε_w of Figure 3.4a at half \tilde{A}_{\max} .

To understand the volume-dependence, we consider the dimensionless (scaled) area ($\tilde{A} \equiv A^{2/3}/V$) where low values of \tilde{A} are more spherical, and high values of \tilde{A} are more branched. As shown in Figure 3.4a, the maximum value of \tilde{A} is approximately 35 for all droplet volumes. However, larger droplets require a larger electrical potential ε_{\max} at which they reach this maximum. We find a scaling collapse for $\tilde{A}(\varepsilon)$ by re-plotting the data as a function of

$$\tilde{\varepsilon} = \frac{\varepsilon - \varepsilon_{\max}}{\varepsilon_w} \quad (3.2)$$

where ε_w is the full width of the curve at half-maximum. This scaling collapse over all four droplet volumes is shown in Figure 3.4b. For all four droplet volumes, regimes A and D both

have low values of \tilde{A} . Regime B appears on the left side of the peak ($\varepsilon < \varepsilon_{\max}$) and regime C on the right ($\varepsilon > \varepsilon_{\max}$). The peak roughly corresponds to the boundary between regimes B and C, an observation that we will explain below in terms of the development of the oxide layer. For regime B, some of the droplets continued to spread, even after satellite droplets had broken off. This continued growth is not reflected in the data.

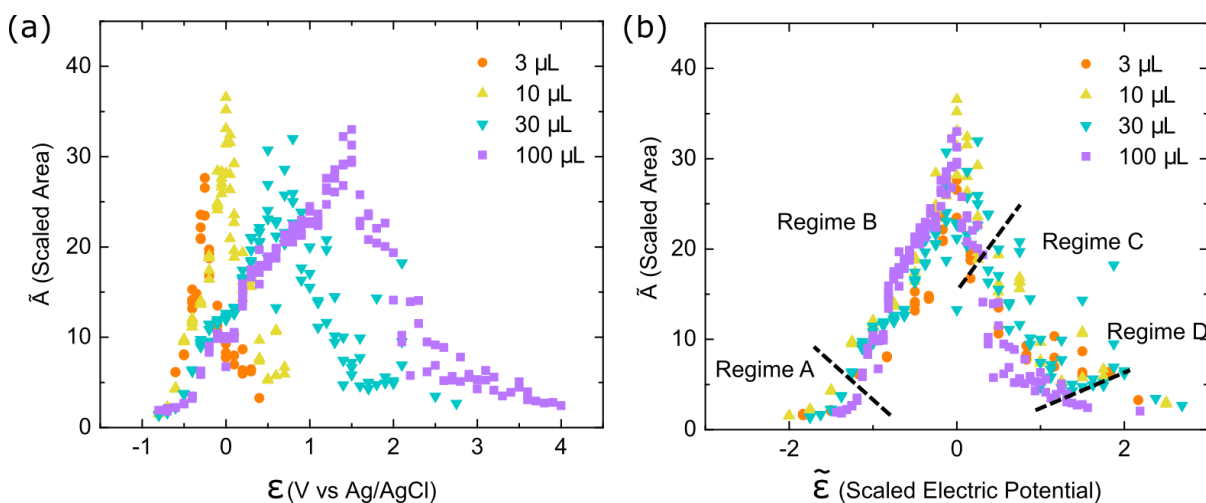


Figure 3.4: (a) Scaled area \tilde{A} as a function of applied electric potential ε . (b) The data from (a) with a rescaled horizontal axis to show similarity of results, with $(\varepsilon_{\max}, \varepsilon_w)$ measured from (a) for each droplet volume.

3.3.2 Spreading and Restoring Forces

The transitions between these four regimes can be understood in terms of the relative magnitude of spreading vs. restoring forces. The following forces were considered: gravity, surface tension, electrostatics, electrostriction, oxidative stresses, and inertia. Several of these forces are negligible based on either calculations or experimental observations, as discussed below. We find that 3 main forces – gravity, surface tension, and oxidative stresses – are sufficient to explain the regimes shown in the phase diagram: the spreading (and corresponding

decreasing thickness) of the droplets, the undulation/branching instability, and the contraction of the droplet.

Gravity: In all regimes, the droplets spread primarily due to the force of gravity. For a droplet of volume $V \propto R^2h$ and density ρ , the force per unit area on the outer rim region with area Rh is

$$P_g = \Delta\rho gh \quad (3.3)$$

As the droplet spreading over time, h gets smaller and therefore gravitational forces become correspondingly smaller. Typical magnitudes range from 10-100 Pa, but can fall as low as 1 Pa for the thinnest droplets in regime B. These calculations indicate that the behavior of the liquid metal is dictated, in part, by the balance between surface tension and gravity.

Surface Tension: Droplets exhibit a restoring Laplace pressure P_L due to their surface tension

$$P_L \sim \frac{\gamma}{h} \quad (3.4)$$

where γ is the surface tension of the droplet, and the droplet thickness, h , is the smallest radius of curvature. This pressure will decrease under applied ε as the surfactant-like oxide grows and lower thereby γ . Typical magnitudes are 50-1000 Pa in regime A, dropping as low as 0.1 Pa in all other regimes, along the gravitational spreading forces to overtake it.

Electrostatics: Electrostatic forces have been shown to influence similar systems (the liquid metal will actuate selectively toward the counter electrode). Despite these forces, we found that positioning the counter electrode in solution above the droplet still resulted in outward-spreading even though any electrical forces would point inward and upward. By

tilting the apparatus, we introduce a lateral gradient of gravitational forces to estimate the magnitude of the electrostatic force. We examined the average displacement of the droplet's leading edge for a range of tilting angles, $0 \leq \theta < 2$. The rate of displacement changes sharply for angles of tilt greater than a critical angle, $\theta_c \sim 0.32$ (**Figure 3.5**).

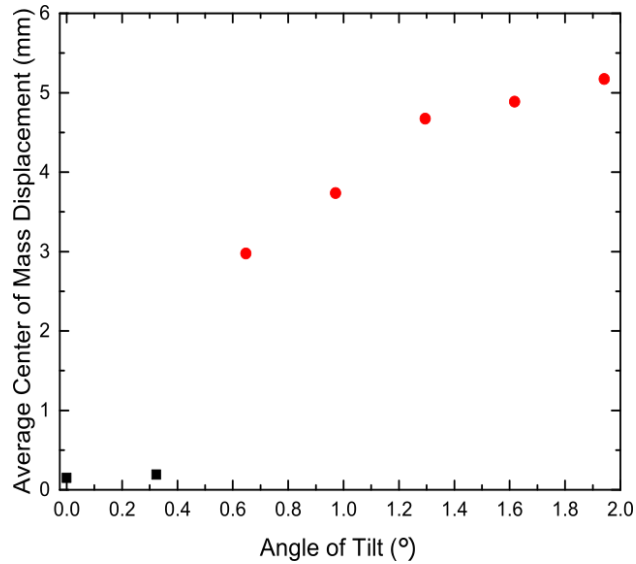


Figure 3.5: Average center of mass displacement created by tilting the apparatus in Figure 3.1a. 2.5 volts were applied to a 30 μL droplet with no reference electrode present in the system.

At this critical angle, the gravitational forces exceed electrostatic forces. Using this angle, we relate the electrostatic force to the gravitational force and find $P_\epsilon \sim mg \sin(\theta_c)/A \sim 0.5 \text{ Pa}$, which is lower than all calculated gravitational forces, indicating that the effects of electrostatics remain smaller than other forces.

Electrostriction: Another possible explanation is lateral stresses caused by electrostriction or the growth of the oxide layer. In the case of electrostriction, the oxide would act as a dielectric in a capacitor, with charges on either side acting to compress the oxide and create lateral forces to cause spreading. This force can be estimated by

$$F_E = \frac{1}{2} \epsilon_{oxide} \left(\frac{\Delta E}{d} \right) \quad (3.5)$$

where ϵ_{oxide} is the dielectric permittivity of the oxide layer (which we assume to be $10^{-10} \text{ m}^{-3} \text{ kg}^{-1} \text{ s}^4 \text{ A}^2$). Even assuming an oxide layer thickness of 3 nm and an applied potential of 1 V, this force remains an order of magnitude lower than the yield stress of the oxide layer (5 MPa vs. 30 MPa); additionally, the oxide thickness grows more quickly than the potential, indicating that this force is smaller at higher regimes. These calculations indicate that electrostriction is not the driving force behind the spreading.

Oxidative Stresses: Previous studies of anodic growth of oxides in aluminum¹⁸ have shown internal oxidative stresses on the order of 0.1 GPa. Based on the size of the droplets (~1 mm), this would correspond to a force of approximately 100 N; this force is more than enough to exceed the force provided by surface tension at this scale (10^{-4} N). Oxidative stresses would also be consistent with the contraction seen in regime C and D; as the oxide grows too thick, the oxidation slows down and the surface tension acts as a restoring force. Furthermore, when a liquid metal droplet is confined laterally such that outward spreading can no longer occur, visible buckling appears on the surface of the metal in regime B; this is also consistent with oxidative stresses.

Inertial Forces: Inertial effects due to initial kick of velocity $v \propto \frac{dR(t)}{dt} = \dot{R}$ and mass $= \rho v$. This is decreasing over time as v decreases, and points outwards. With an outer rim area $A \propto Rh$ and Stokes' drag $F_{drag} \propto \mu Rv$

$$P_I(t) \propto \frac{F_{drag}}{Rh} = \frac{\mu R(t)}{h(t)} \quad (3.6)$$

In all regimes, the maximum value of the inertial forces calculated is 0.01-0.1 Pa (with a value of zero in regime A), indicating that inertial forces are not the primary driver of spreading. We tested regime D to see if inertial effects were the causing an "overshoot" before the drop ultimately retracted. To determine whether this overshoot of the final area was inertial, we changed the method of applying the potential. Rather than stepping up immediately to the final potential, we used a linear sweep of potential at a rate of 100 mV/s to slowly bring the drop into regime D. When this linear sweep was utilized, the overshoot and retraction disappeared. From this we can conclude that inertial forces are responsible for the initial spreading, or that stepping the potential immediately to its final value does not provide sufficient time for oxide growth.

3.3.3 Oxide Growth and Dissolution

To understand the forces imparted onto the liquid metal by the oxide layer, it is important to first quantify the thickness of the oxide layer as a function of time and potential. Direct measurement of the oxide thickness is hindered by a number of challenges; the dynamic nature of the droplet shape makes measurements via optical techniques (e.g. ellipsometry) impractical, as does the asymmetry of oxide growth across the droplet. Here, we use electrochemical measurements to estimate both the average growth and dissolution of rates of the oxide layer across the surface with a simple mathematical model.

To model the thickness, we first estimate the dissolution rate of the oxide (which we assume to be constant across all potentials) in 1 M NaOH. In regime A, where the droplets are spheroids, we employ a quasi-steady-state model, where the growth rate and dissolution rate of the oxide are assumed to be equal. These rates are determined by the two variables measured

during the experiment: the Faradaic current and the 2-D projection of the droplet surface area ($A_{S,2D}$). The Faradaic current allows calculation of the amount of gallium oxidized as a function of time by

$$\int I(t) dt = q \quad (3.7)$$

Where $I(t)$ represents the current as a function of time, and q represents charge transferred. The charge can be converted to moles of Ga^{3+} generated by

$$n = \frac{q}{zF} \quad (3.8)$$

where z is the number of electrons transferred in the oxidation reaction and F is the Faraday constant (96485 C/mol). This growth rate is first normalized by the surface area of the droplet; however, $A_{S,2D}$ is not an accurate representation of the 3-D surface area of the droplet $A_{S,3D}$ in regime A. To estimate the actual surface area, we assume that the droplet is an oblate spheroid when the potential is applied. By measuring the radius of the droplet (and with the known volume), $A_{S,3D}$ is determined by the surface area equation for an oblate spheroid

$$A_{S,3D} = 2\pi R^2 + \pi \frac{h^2}{e} \ln \frac{1+e}{1-e} \quad (3.9)$$

where e is

$$e = \sqrt{1 - \frac{h^2}{R^2}} \quad (3.10)$$

and h is the height of the droplet, determined from the volume. From these values, the growth rate of the oxide in regime A (and therefore, the dissolution rate across all regimes) can be estimated

$$k_{growth,Regime A} = k_{dissolution} = \frac{n}{A_{S,3D}\Delta t} \quad (3.11)$$

These represent the rate at which the gallium is oxidized at the surface. While the dissolution rate is assumed constant across regimes, we repeat this process for regime B-D to ascertain the growth rate for each regime. We also assume that, because the height of the droplet is much smaller in these regimes, $A_{S,2D}$ is the most reasonable representation of the true surface area of the droplet. The growth and dissolution rate represent the oxidation of gallium on the droplet; the average thickness across the entire surface can then be represented by

$$d(t) = \frac{M_W}{2\rho} \int_0^t (k_{growth} - k_{dissolution}) dt \quad (3.12)$$

where M_W and ρ represent the molecular weight and density of the oxide, respectively.

We note that this model depends on a variety of assumptions: We assume that the growth on the surface is dominated by gallium oxide is the dominant molecule being grown on the surface of the droplet; however, previous electrochemical studies indicate that gallium hydroxide and gallate salts form on the surface in alkaline solutions. We also acknowledge that this provides an average of growth across the surface, while the layer can be seen visually to growth thicker in areas closer to the counter-electrode. However, this model is designed to provide an approximation of the average oxide thickness for each Regime relative to each other; further studies will be necessary to obtain a more complete picture of the the oxide profile across the surface of the droplet over time. **Figure 3.6a** shows the change in the growth rate as a function of time for the case of regimes B, C, and D. For each regime, the initial increase in the surface area causes a drastic decrease in the growth rate, which ultimately levels to a steady-state value. These data (Figure 3.6b and 3.6c) indicate that the oxide thickness

grows to a maximum of 1-4 microns, and is relatively consistent across regimes B and C, though larger in regime D. The maximum oxide layer thickness increases monotonically with electrical potential, and is approximately three orders of magnitude larger than the oxide thickness in air; although the steady-state growth rate is slightly smaller for regime B than regime C, the data still indicate a larger oxide thickness, due to a larger initial growth rate.

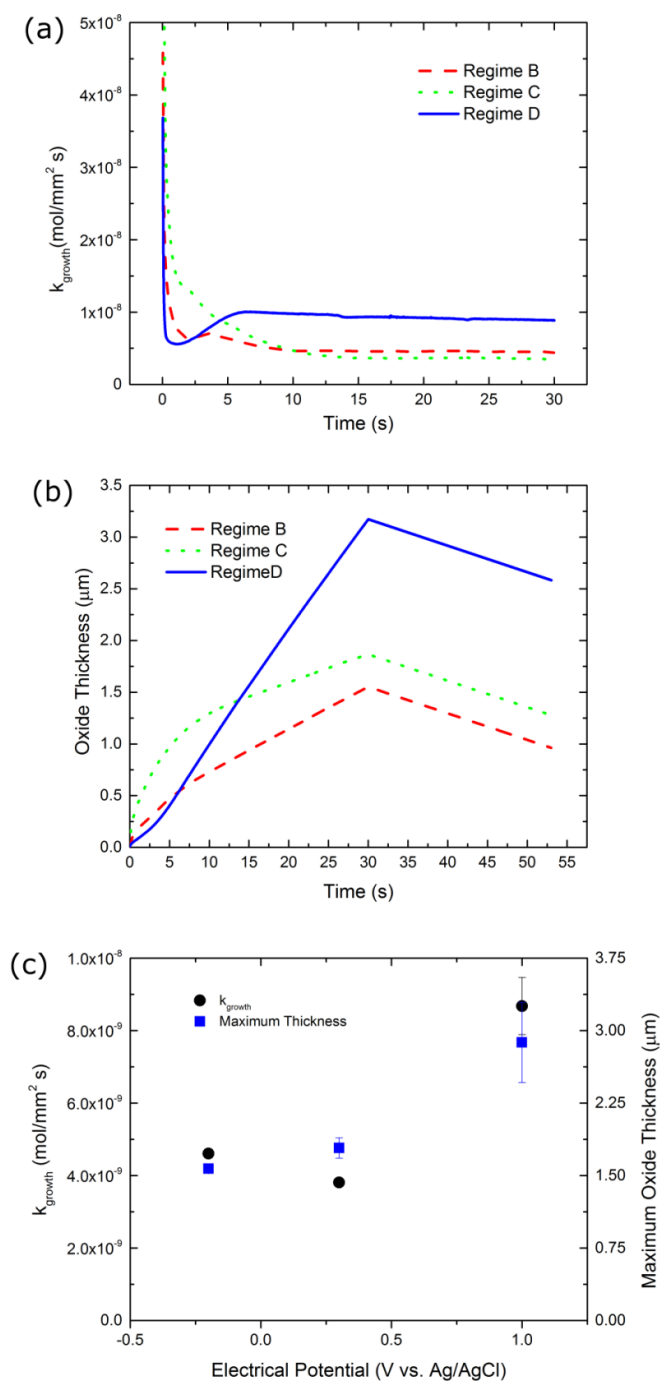


Figure 3.6: Oxide growth during anodic oxidation. a) Modeled growth rate of the oxide layer, estimated from the measured surface area and current profile of a 30 μL droplet at -0.2 V, 0.3 V, and 1 V. b) Modeled average oxide thickness under the same conditions. c) Steady-state growth rate and maximum oxide thickness.

3.4 Conclusions

We have demonstrated fingering instabilities in a liquid metal droplet that drastically changes its shape under an applied potential in aqueous solution. This behavior is interesting for a variety of reasons: it shows that an oxide layer can be tuned to both create fingering instabilities and ultimately halt them; it demonstrates a new class of self-similar dynamics; and it has the potential to be used in devices that necessitate shape reconfigurable conductors. Future work will focus on better characterizing the oxide layer. This will include measuring or modeling the oxide growth not only over time and potential, but also as a function of position on the droplet.

3.5 References

1. Witten, T. A. & Sander, L. M. Diffusion-Limited Aggregation, a Kinetic Critical Phenomenon. *Phys. Rev. Lett.* **47**, 1400–1403 (1981).
2. Saffman, P. G. & Taylor, G. The Penetration of a Fluid into a Porous Medium or Hele-Shaw Cell Containing a More Viscous Liquid. *Proc. R. Soc. A* **245**, 312–329 (1958).
3. Tabeling, P., Zocchi, G. & Libchaber, A. An experimental study of the Saffman-Taylor instability. *J. Fluid Mech.* **177**, 67 (1987).
4. Sharon, E., Moore, M. G., McCormick, W. D. & Swinney, H. L. Coarsening of Fractal Viscous Fingering Patterns. *Phys. Rev. Lett.* **91**, 205504 (2003).
5. Mathiesen, J., Procaccia, I., Swinney, H. L. & Thrasher, M. The universality class of diffusion-limited aggregation and viscous fingering. *Europhys. Lett. EPL* **76**, 257–263 (2006).

6. Davidovitch, B., Levermann, A. & Procaccia, I. Convergent calculation of the asymptotic dimension of diffusion limited aggregates: Scaling and renormalization of small clusters. *Phys. Rev. E* **62**, R5919–R5922 (2000).
7. Langer, J. S. Instabilities and pattern formation in crystal growth. *Rev. Mod. Phys.* **52**, 1–28 (1980).
8. Utter, B., Ragnarsson, R. & Bodenschatz, E. Alternating tip splitting in directional solidification. *Phys. Rev. Lett.* **86**, 4604–4607 (2001).
9. Troian, S. M., Herbolzheimer, E., Safran, S. A. & Joanny, J. F. Fingering Instabilities of Driven Spreading Films. *EPL Europhys. Lett.* **10**, 25 (1989).
10. Cachile, M. & Cazabat, A. M. Spontaneous Spreading of Surfactant Solutions on Hydrophilic Surfaces: CnEm in Ethylene and Diethylene Glycol. *Langmuir* **15**, 1515–1521 (1999).
11. Cheng, X., Xu, L., Patterson, A., Jaeger, H. M. & Nagel, S. R. Towards the zero-surface-tension limit in granular fingering instability. *Nat. Phys.* **4**, 234–237 (2008).
12. Bischofberger, I., Ramachandran, R. & Nagel, S. R. Fingering versus stability in the limit of zero interfacial tension. *Nat. Commun.* **5**, 5265 (2014).
13. Khan, M. R., Eaker, C. B., Bowden, E. F. & Dickey, M. D. Giant and switchable surface activity of liquid metal via surface oxidation. *Proc. Natl. Acad. Sci.* **111**, 14047–14051 (2014).
14. Biggins, J. S., Wei, Z. & Mahadevan, L. Fluid-driven fingering instability of a confined elastic meniscus. *Europhys. Lett.* **110**, 34001 (2015).

15. Zhao, M., Belmonte, A., Li, S., Li, X. & Lowengrub, J. Nonlinear simulations of elastic fingering in a Hele-Shaw cell. *J. Comput. Appl. Math.* in press (2015).
doi:10.1016/j.cam.2015.11.016
16. Costa, Alceu. Hausdorff (Box-Counting) Fractal Dimension.
<https://www.mathworks.com/matlabcentral/fileexchange/30329-hausdorff--box-counting--fractal-dimension>
17. Daccord, G., Nittmann, J. & Stanley, H. E. Radial viscous fingers and diffusion-limited aggregation: Fractal dimension and growth sites. *Phys. Rev. Lett.* **56**, 336–339 (1986).
18. Çapraz, Ö. Ö., Shrotriya, P. & Hebert, K. R. Measurement of Stress Changes during Growth and Dissolution of Anodic Oxide Films on Aluminum. *J. Electrochem. Soc.* **161**, D256–D262 (2014).

Chapter 4

Electrowetting Without Applied Potential Using Paint-on Electrodes

4.1 Introduction

Electrowetting is a technique used to manipulate liquid drops on a substrate.^{1,2} It is useful for microfluidic applications including liquid lenses³, displays^{4,5}, and miniature bioassays.^{6,7} Unlike electrocapillarity⁸, electrowetting is driven by an electromechanical force and does not involve a change in interfacial tension. Applying a potential to the fluid of interest (often water) relative to an electrically insulated counter electrode generates the required electrical charge. The electrical insulation (dielectric) prevents Faradaic electrochemical reactions from occurring in the liquid (e.g., electrolysis of water). This configuration is called electrowetting-on-dielectric (EWOD) and is the most common electrowetting technique for actuating fluids. As applied voltage is increased, the liquid changes its apparent contact angle to lower its capacitive energy. An ideal EWOD system should achieve maximum changes in contact angle with minimal applied voltage.

However, fabricating an ideal electrode for EWOD is typically a challenging process, especially when low voltage operation (< 15 V) is desired. The dielectric coated atop a conductive metal film or doped Si wafer⁹, is often achieved via thermal oxidation, sputtering, thermal evaporation, or atomic layer deposition. An ideal dielectric exhibits a large electrical capacitance and is free of pin holes to prevent electrical shorts through the insulator. Electrowetting dielectrics are commonly hundreds of nanometers to several microns thick to ensure sufficient insulation between the liquid and the electrode.¹⁰ However, thicker dielectrics

necessitate larger voltages. Furthermore, reducing the dielectric thickness is often insufficient, because the required voltage decreases only as the square root of the thickness.¹¹ Some clever resolutions have been developed to mitigate dielectric breakdown, including multilayers of dielectrics¹¹, self-healing dielectrics¹², and utilization of two immiscible electrolytes.¹³

Here, we demonstrate a unique approach for creating self-healing, low-voltage, battery-free, and even stretchable electrowetting systems. In this work, an electrode composed of eutectic gallium indium (EGaIn, 75% Ga, 25% In by weight)¹⁴ or pure gallium can be simply painted on a substrate (e.g. glass) at room temperature. Due to the low melting point (~15.5 °C) of EGaIn, the metal is liquid at room temperature and forms a thin (~1-3 nm)¹⁵ passivating oxide layer. This oxide forms spontaneously in the presence of oxygen and serves to mechanically stabilize the liquid metal in the shape of a film. This work takes advantage of the thin, self-forming oxide as a dielectric for electrowetting.

Using an EGaIn electrode is a simple approach that solves numerous electrowetting challenges: (i) Unlike traditional EWOD dielectrics, EGaIn can be applied to a surface quickly, at room temperature, and without vacuum processing. This process is shown in **Figure 4.1**. (ii) As a liquid, EGaIn conforms to both non-planar and stretchable substrates. (iii) The Ga oxide on EGaIn can support self-assembled lipid bilayers^{16,17} that enable large contact angle changes (> 100°) for water by applying small voltages (100s of mV). (iv) The anodic nature of the oxide and the self-assembly of the lipid bilayer allows the dielectric layer to self-heal upon breakdown.¹² (v) Perhaps most interestingly, the small voltages required to induce changes in contact angle in this system reveal the effects of the so-called ‘potential of zero charge’, which

allows significant electrowetting to occur simply by shorting the electrodes without the need for an external voltage.

The potential of zero charge, V_{PZC} , is the electric potential at which the plot of apparent contact angle versus potential (i.e. the electrowetting curve) reaches a maximum. It can be understood by considering the Lippmann-Young equation¹, which models the contact angle change in response to voltage across an electrowetting interface as shown in Equation 4.1,

$$\cos \theta(V) = \cos \theta_Y + \frac{C(V - V_{PZC})^2}{2\gamma_{wo}} \quad (4.1)$$

where θ is the contact angle of the liquid as a function of applied voltage (V), θ_Y is the Young's angle (i.e., the angle in the absence of applied voltage), C is the capacitance of the dielectric normalized by area in contact with the liquid, V is the applied voltage, V_{PZC} is the potential of zero charge, and γ_{wo} is the interfacial surface tension between the two liquids (e.g. water and oil). The V_{PZC} is a function of surface potential, electrolyte composition, and the composition of the top and bottom electrodes. According to Equation 4.1, the V_{PZC} causes the electrowetting curve to be centered away from zero volts.¹⁸ In most electrowetting systems, however, inducing changes in contact angle requires application of tens¹⁹ to hundreds²⁰ of volts. These voltages are significantly larger than the V_{PZC} (< 1 V); therefore, the electrowetting curve often appears to center at zero volts. Thus, in practice, the V_{PZC} is neither experimentally significant nor discernable.

In the system described here, the voltages needed to induce electrowetting are extremely low (similar in magnitude to the V_{PZC}) due to the very large capacitance (arising from the thin dielectric) and the low γ_{wo} (arising from the use of surfactants). Furthermore, the

materials of construction render a large V_{PZC} . Consequently, significant electrowetting occurs by simply short-circuiting the electrodes without an external potential present. Stated differently, Equation 4.1 evaluated at $V=0$ results in a significant change in contact angle since V_{PZC} is non-negligible. Consequently (and in contrast to conventional EWOD), increasing the potential relative to 0 V increases the contact angle of the liquid droplet; thus, it is possible to electrodedewet a droplet under these circumstances.

Here, we outline the fabrication of these EGaIn electrodes, characterize their electrowetting behavior, describe the wetting of drops of water when short-circuited with the electrode, and demonstrate the robustness of the electrowetting while stretching of the underlying substrate.

4.2 Results

We fabricate the electrodes by dragging a 100 μ L droplet of EGaIn along the length of a glass slide using a custom-built slot die coater. This process establishes a thin and shiny film of EGaIn, as seen in Figure 4.1a-c. A strip of copper tape under the liquid metal forms an electrical connection. The entire apparatus rests on the stage of a contact angle goniometer (Figure 4.1d).

The electrode supports a droplet of de-ionized water (DI H₂O) with 1 wt% sodium dodecyl sulfate (SDS), which is submerged in a solution of dodecane containing 0.2 wt% sorbitan trioleate (a non-ionic surfactant). A stainless steel electrode connects to the top of the droplet, as shown in Figure 4.1e. Surfactants are typically used in electrowetting to lower the energetic penalty associated with increasing meniscus surface area (spreading, wetting) and

therefore increase the responsiveness of the liquid to voltage. Previous studies show that sorbitan trioleate forms a lipid bilayer between the drop of water and substrate¹⁶, which is evidenced here by the lack of wetting between the liquid and substrate. In this case, the lipid bilayer lowers the interfacial surface tension of the SDS/water solution to a very low level of ~ 0.2 mN/m, based on pendant drop analysis. This low interfacial surface tension is a requirement to induce a large change in the contact angle. Using higher surface tensions would result in more modest changes in contact angle for a given voltage; the maximum voltage is set by the breakdown strength of the dielectric.

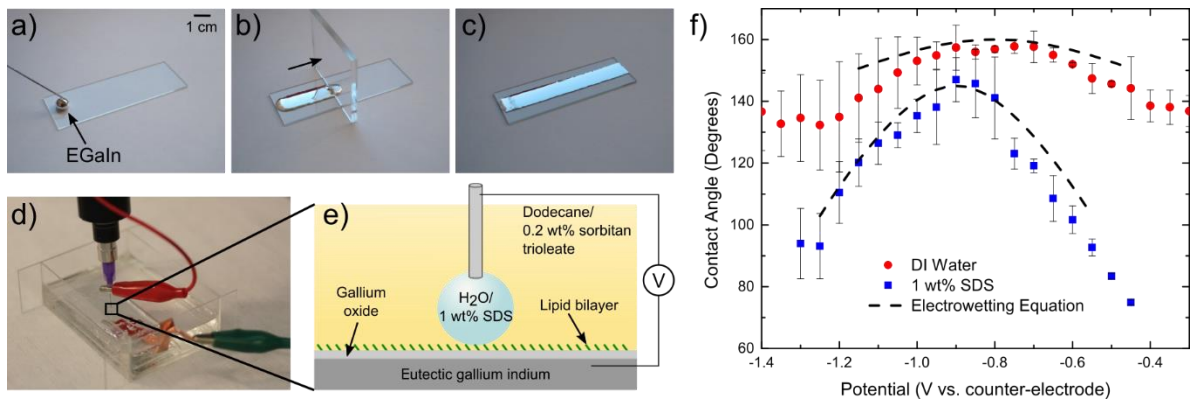


Figure 4.1: Preparation of the ‘paint on’ liquid metal electrodes for low-voltage electrowetting. (a,b,c) 100 μ L drop of EGaIn is placed on a glass substrate and spread as a film across the surface. (d,e) A DI H₂O/1 wt% SDS drop is submerged in dodecane/0.2 wt% sorbitan trioleate solution and voltage is applied across a top electrode (a stainless steel dispensing needle) and the EGaIn layer. (f) DC electrowetting curve of DI H₂O and H₂O/1 wt% SDS, including theoretical curves. Error bars represent s.d.

The experimental configuration in Figure 4.1 is representative of a typical EWOD system. Here, the dielectric is the gallium oxide that forms spontaneously on the surface of the liquid metal along with the lipid bilayer that self-assembles on the oxide.

Figure 4.1f shows the electrowetting curve for an applied DC potential. These curves show dramatic contact angle changes (70° - 80° changes over 400 mV for a solution of DI H₂O/1 wt% SDS), with the parabolic shapes indicating classic electrowetting behavior. Importantly, the curve reaches a maximum away from zero volts (approximately -900 mV) for both fluids. This maximum of contact angle identifies the potential of zero charge (V_{PZC}). The largest changes in contact angle occurs at -1.3 V and -0.5 V, which are approximately 0.4 V from the V_{PZC} . At these terminal potentials, satellite droplets emerge from the contact line of water and lipid bilayer, which has also been observed at occurrence of electrowetting saturation.^{1,21} These values also agree well with the theoretical curves given by Equation 4.1, plotted using the experimentally measured capacitance. In each case, the droplets showed full reversibility, dewetting from the substrate and beading up into a spherical shape upon removal of the potential. The wetting behavior continues to be fully switchable even after dielectric breakdown occurs. This recovery is due to the self-healing nature of the oxide layer of the liquid metal and subsequent reassembly of the lipid bilayer.

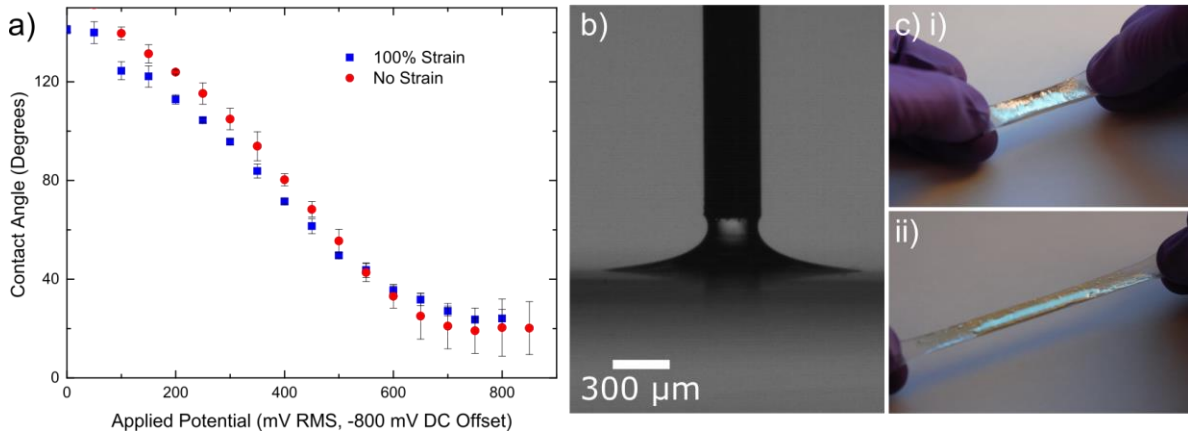


Figure 4.2: Electrowetting on a stretchable substrate. (a) AC electrowetting curve on EGeIn, with both no strain and 100% strain of the underlying substrate. (b) Minimum reversible contact angle achieved (7°) with AC electrowetting at -800 mV RMS applied. (c) Photographs of i) EGeIn film on a substrate made of silicone elastomer. ii) Liquid metal conforms to the elastomer and elongates when the substrate is stretched.

AC potentials are known to increase the stability of the contact line in electrowetting by preventing either charge trapping or degradation²¹, and thereby improve reproducibility and minimize dielectric breakdown. In addition to exploring the DC behavior, we also employed an AC potential with a -800 mV DC offset to account for the potential of zero charge. This offset centers the electrowetting curve about zero volts, as shown in the electrowetting curve plotted in **Figure 4.2a**. The contact angle shows a substantial decrease ($\sim 130^\circ$ change) with the application of only 700 mV RMS. Furthermore, we observe contact angle saturation²² at an average value of 20° with a minimum observed value of 7° , as shown in Figure 4.2b. The low value of saturation is desirable, as saturation occurs near 60° - 80° for traditional aqueous EWOD systems²³, with lower values (15° - 30°)²⁴ being observed with ionic liquids. As expected, the AC electrowetting results show significantly less variance than the DC electrowetting, and the contact line remained stable over the duration of the tests (up to several

hours), with no observed satellite droplets. In addition, sequentially increasing and decreasing the amplitude of the AC potential provided no signs of contact angle hysteresis in the system. The lack of hysteresis with use of AC potential is consistent with results both theoretically and experimentally proven by Mugele and colleagues.²⁵

The formation of the oxide layer on the liquid metal surface provides several advantages that have been utilized for this work. In addition to stabilizing the film of liquid metal (such that it does not bead up into a sphere due to surface tension of the metal), the oxide also allows EGaIn to adhere to a variety of substrates (e.g. glass, silicon, polymers). Here, we utilize a stretchable, silicone-based elastomer (Ecoflex, Smooth-on, Inc) to test electrowetting with a strained electrode. Previous work has shown electrowetting on curved and flexible²⁶ substrates but, to the best of our knowledge, none have shown electrowetting on a stretchable material. Most of the conductors and dielectrics used in EWOD are comprised of rigid materials that crack at small strains; in contrast, the liquid metal forms an inherently stretchable electrode. Figure 4.2c shows photographs of a film of EGaIn on an elastomeric substrate. We elongated the substrate to 100% tensile strain and performed electrowetting. The liquid metal on stretched Ecoflex shows similar electrowetting behavior as liquid metal on a glass substrate. The drawback, however, was minor swelling that occurred over time in the Ecoflex due to the dodecane immersion fluid.

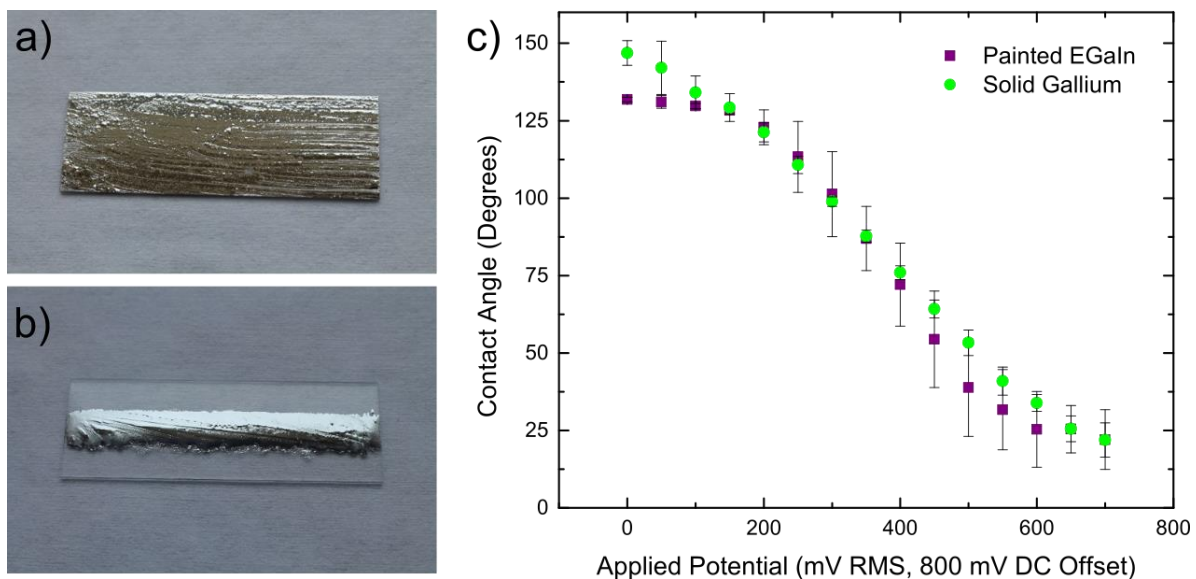


Figure 4.3: Electrowetting on metal with various fabrication techniques. a) “Painted” EGaIn film that was brushed roughly across substrate. b) Solid gallium film prepared by spreading liquid Ga with a slot-die and then frozen. c) Electrowetting curve that shows similar behavior between these films and “pristine” liquid metal surface.

Until now, all the reported experiments were performed on smooth liquid metal surfaces for consistency and simplicity of analysis. However, EWOD on gallium-based alloys does not require a pristine surface with a smooth liquid interface. Applications may instead call for thin films of the liquid metal or solid surfaces. **Figure 4.3a** and **4.3b** show a thin film of liquid EGaIn and a film of solidified gallium, respectively. The EGaIn was prepared by brushing a 20 μL drop across the surface of a glass slide. The gallium was prepared in the same manner as demonstrated in **Figure 4.1** and then allowed to freeze at room temperature (m.p. $\sim 30^\circ\text{C}$). In spite of the surface heterogeneity present on the EGaIn film, the difference in contact angle change from the pristine EGaIn surface was negligible (albeit with more variance). Similar

results were seen with solidified gallium, indicating that the electrowetting is dependent on the surface properties of the gallium oxide, rather than the phase of the underlying electrode.

Perhaps the most interesting aspect of the liquid metal electrodes is that V_{PZC} is approximately -800 to -900 mV (vs. the stainless steel counter-electrode); this value is also consistent with the measured open circuit potential, which generally measured in the range of -800 mV to -1.0 V. Because of the low voltages needed to induce electrowetting, the V_{PZC} must be taken into account.^{18,27} As a consequence of this offset, simply closing the circuit between the EGaIn and top electrode causes significant droplet wetting by effectively bringing the system ~800 mV away from the V_{PZC} (**Figure 4.4**). This wetting is reversible; opening the circuit causes the droplet to dewet the substrate. This process may be cycled between the short circuit (wetting) and the open circuit potential (dewetting) for thousands of cycles, although leaving the system short-circuited for extended periods of time results in thickening of the oxide. An implication of this phenomenon is that applying a potential (relative to a shorted system) causes dewetting, as evident by the electrowetting curve (cf. Figure 4.1f).

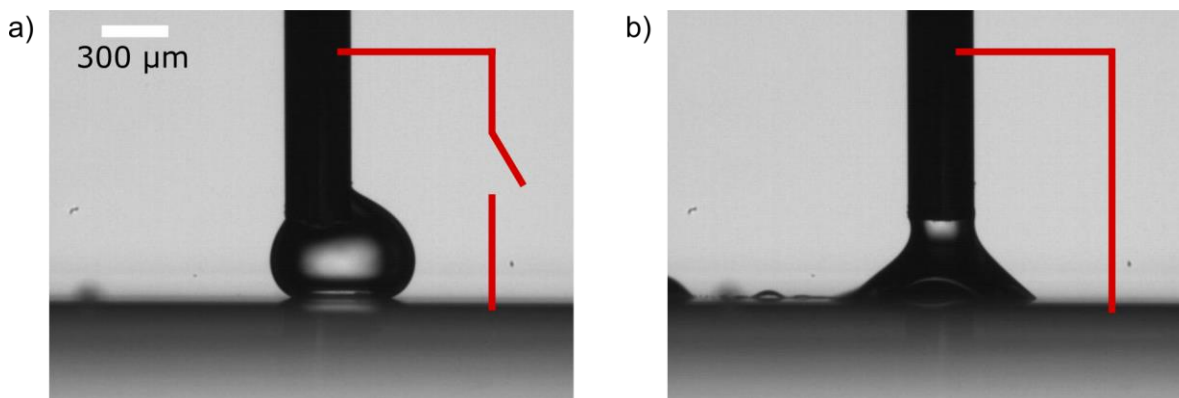


Figure 4.4: Wetting of a droplet on EGaIn without externally applied potentials. (a) At open circuit, the droplet maintains a large contact angle with the substrate. (b) When the circuit is closed, the drop rapidly (and reversibly) wets the substrate due to the offset from the V_{pzc} .

The ability to induce wetting without an external voltage source is due to the non-negligible V_{PZC} . Previous work has shown that the V_{PZC} is a function of the surface potential, electrolyte composition, and the composition of the top and bottom electrodes.²⁷ Since the V_{PZC} appears to occur at the same value for DI water and SDS solutions, we instead varied the metal used in the top electrode to shift the V_{PZC} . We utilized both solid and liquid conductors for the top electrode, including stainless steel, copper, platinum, solid gallium, and EGaIn while measuring the resulting electrowetting curve (**Figure 4.5a**) by linearly sweeping the potential at 1 mV/s using DI water. In each case, the shape of the electrowetting curve remains similar, but each one shows a distinct offset of the peak. Furthermore, a symmetric system (with either EGaIn or gallium as the top electrode) shows an apex approaching zero volts. The results here imply that simply changing the materials of construction of the top electrode is a simple way to shift the electrowetting behavior. The current profiles (**Figure 4.5b**) align with the key features in the electrowetting curves (**Figure 4.5a**); there is no current at the apex for each electrowetting curve, while there is current from dielectric breakdown at the potentials where

contact angle begins to saturate. Replicating the electrowetting curve with a Ag/AgCl reference electrode inserted into the solution causes the apex of the respective curves to center near a single value (approximately -0.6 V vs. Ag/AgCl) (Figure 4.5c). This collapse occurs because the Ag/AgCl reference electrode replaces the role of the top electrode in defining the V_{PZC} . Moreover, the current profiles in Figure 4.5d indicate that current only occurs away from the apex of the curves.

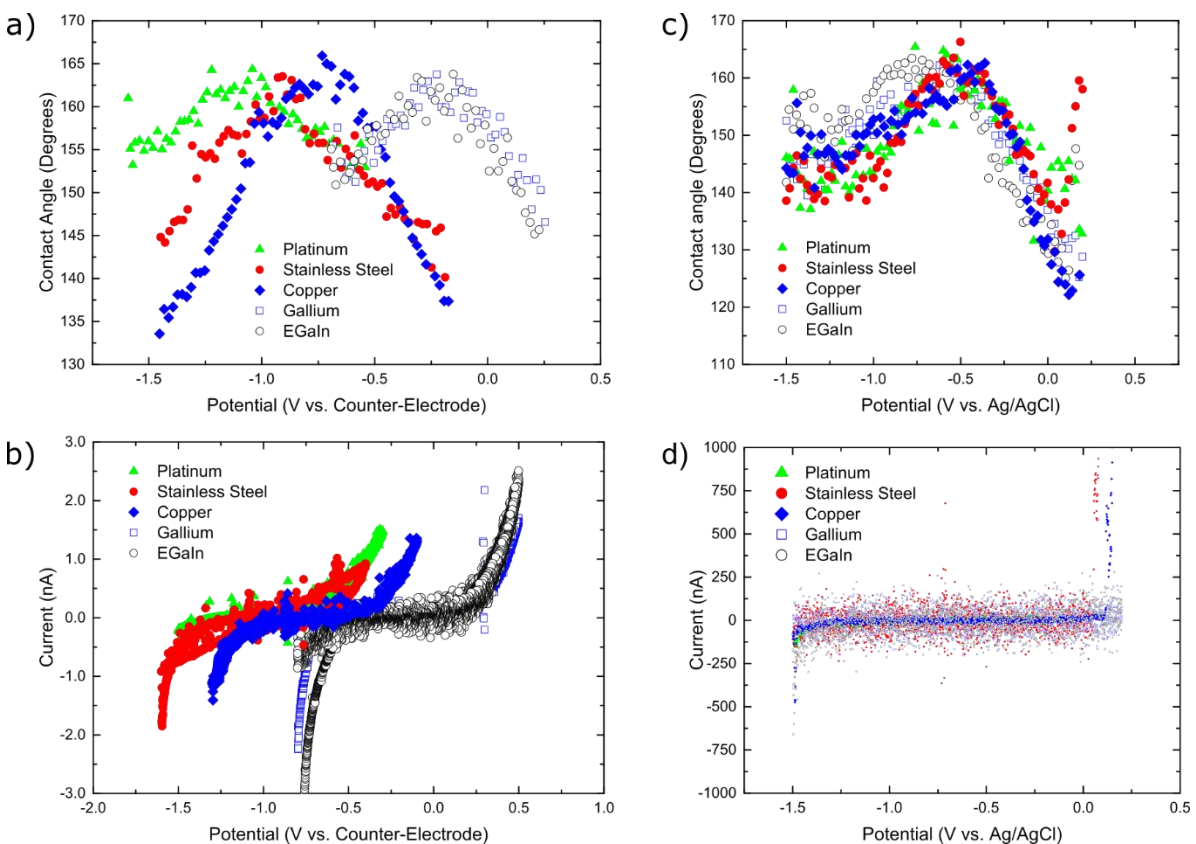


Figure 4.5: The point of zero charge varies with materials of construction. (a) Electrowetting curve of DI water with platinum, stainless steel, copper, gallium, and EGaln top electrodes. EGaln film serves as the substrate electrode for electrowetting. (b) Linear sweep voltammogram of two-electrode system at 1 mV/s. (c) Electrowetting curve of DI water with varied top electrodes and Ag/AgCl reference electrode. (d) Linear sweep voltammogram of three-electrode system at 1 mV/s.

4.3 Conclusions

We have demonstrated a robust system for electrowetting-on-dielectric that is simple to fabricate, self-healing, stretchable, reversible, and operates at low voltages. It is also capable of wetting without an external potential due to the non-zero ‘potential of zero charge’ arising from the materials of construction of the electrodes. Applying a potential relative to this shorted configuration results in electrodedewetting. The combined simplicity of this system and its ability to electrowet without externally applied voltage provides a simple strategy to manipulate liquid droplets for microsystems and lab on a chip systems. These unconventional electrodes may also enable or facilitate electrowetting in new places, such as microfluidics (e.g. injectable electrodes), rough surfaces, and stretchable substrates.

4.4 Methods and Materials

Substrate Fabrication: We fabricated the electrodes by first constructing a spreader tool (similar to a slot die with a gap of 50 μm) out of polymethylmethacrylate (PMMA) using a laser cutter. Dragging the spreader along the length of the 3” x 1” glass slide established a thin and shiny film from a 100 μL drop of EGaIn. The film was spread across a piece of copper tape on the substrate, to form an electrical connection. This method was also used for the gallium electrode, with the gallium placed in a freezer until it solidified. For the rough film, a 20 μL drop was brushed across the glass surface with a cloth until a continuous film was established across the entire surface.

DC Electrowetting: The contact angle of the water drop is recorded at equilibrium upon applying a DC voltage. A contact angle goniometer (manufactured by First Ten Angstroms 32)

records the contact angle of the droplet. De-ionized water or a solution of water and 1 wt% sodium dodecyl sulfate were dispensed within the oil with a 30 gauge stainless steel syringe needle. Electrical experiments were performed with Agilent E3612A power source. Electrical connections were made to the copper tape on the substrate, and to the syringe needle. The positive terminal of the power source is connected to the stainless steel syringe tip. Meanwhile, the negative terminal is connected to the Cu tape. The negative terminal is also grounded to the source meter. A Fluke multimeter connected in parallel to the Agilent power source was used to verify the applied voltage. Potential was applied from -1.40 V to -0.30 V for the DI water, and -1.30 V to -0.45 V for the SDS/water, in 50 mV increments. The results shown in Figure 2 represent the average contact angle at the respective voltage from three trials. The error bars show the standard deviation of contact angle from the three trials. Beyond -1.1 V, the water droplet cannot achieve an equilibrium contact angle due to dielectric breakdown. In the breakdown regime, the water droplet moves spatially, which results in asymmetric contact angle between left and right side of droplet. The asymmetry of the drop is the cause for high standard deviation of contact angle beyond -1.1 V. All drops were imaged in a First Ten Angstroms 1000B contact angle goniometer.

AC Electrowetting: All AC electrowetting experiments were two-electrode, performed with a -800 mV DC offset with respect to the stainless steel counter-electrode, and a 100 Hz sine wave. The experiments were performed from 0 mV RMS to 800 mV RMS, in 50 mV increments; they were also performed in both directions, to test for hysteresis. The potential was left on for at least one minute, to make sure that the contact angle reached equilibrium.

Stretchable Electrowetting: The stretchable substrates were prepared in the same manner as the glass slides. The EGaIn was spread across a 3 cm x 1.25 cm piece of Ecoflex. The Ecoflex was then stretched to 6 cm, and clipped down to a glass slide to hold the strain in place.

Self-Wetting: The self-wetting experiments were performed by directly connecting the copper tape attached to the substrate and the stainless steel syringe needle.

Variable Electrodes: 23 gauge polypropylene syringe tips were used to dispense DI water. The top electrode material was inserted into the plastic above the syringe tip (to make a connection to the water), and connected to the potentiostat. EGaIn and gallium were injected into Tygon® tubing and then sealed above the tip in the same manner. The potential was then swept at 1 mV/s from -1.5 V to -0.2 V with respect to the counter-electrode for the case of platinum, stainless steel, and copper. For gallium and EGaIn, the potential was swept from -0.5 V to 0.5 V with respect to the counter-electrode, and the resulting contact angle and current were measured.

This method was then repeated, with a reference electrode, along with the counter-electrode. To fabricate the reference electrode, a silver wire was inserted into Tygon tubing that was filled with an agar hydrogel. The hydrogel was made by placing 2 wt% agar into a solution of saturated silver chloride in 3.5 M potassium chloride, heating the solution, and then injecting into the Tygon. Once the reference and counter-electrode were inserted, a linear sweep was performed at 1 mV/s for each metal, from -1.5 V to -0.2 V with respect to the Ag/AgCl reference. From this, the contact angle and current were simultaneously measured.

4.5 References

1. Mugele, F. & Baret, J. C. Electrowetting: From basics to applications. *J. Phys.-Condens. Matter* 17, R705–R774 (2005).
2. Shamaï, R., Andelman, D., Berge, B. & Hayes, R. Water, electricity, and between... On electrowetting and its applications. *Soft Matter* 4, 38–45 (2007).
3. Kuiper, S. & Hendriks, B. H. W. Variable-focus liquid lens for miniature cameras. *Appl. Phys. Lett.* 85, 1128–1130 (2004).
4. Hayes, R. A. & Feenstra, B. J. Video-speed electronic paper based on electrowetting. *Nature* 425, 383–385 (2003).
5. Sun, B., Zhou, K., Lao, Y., Heikenfeld, J. & Cheng, W. Scalable fabrication of electrowetting displays with self-assembled oil dosing. *Appl. Phys. Lett.* 91, 11106-11106–3 (2007).
6. Cho, S. K., Moon, H. J. & Kim, C. J. Creating, transporting, cutting, and merging liquid droplets by electrowetting-based actuation for digital microfluidic circuits. *J. Microelectromechanical Syst.* 12, 70–80 (2003).
7. Chang, Y.-H., Lee, G.-B., Huang, F.-C., Chen, Y.-Y. & Lin, J.-L. Integrated polymerase chain reaction chips utilizing digital microfluidics. *Biomed. Microdevices* 8, 215–225 (2006).
8. Grahame, D. C. The Electrical Double Layer and the Theory of Electrocapillarity. *Chem. Rev.* 41, 441–501 (1947).
9. Arscott, S. Electrowetting at a liquid metal-oxide-semiconductor junction. *Appl. Phys. Lett.* 103, 144101 (2013).

10. Moon, H., Cho, S. K., Garrell, R. L. & Kim, C.-J. 'CJ'. Low voltage electrowetting-on-dielectric. *J. Appl. Phys.* 92, 4080 (2002).
11. Schultz, A., Chevalliot, S., Kuiper, S. & Heikenfeld, J. Detailed analysis of defect reduction in electrowetting dielectrics through a two-layer 'barrier' approach. *Thin Solid Films* 534, 348–355 (2013).
12. Dhindsa, M., Heikenfeld, J., Weekamp, W. & Kuiper, S. Electrowetting without Electrolysis on Self-Healing Dielectrics. *Langmuir* 27, 5665–5670 (2011).
13. Kornyshev, A. A. et al. Ultra-Low-Voltage Electrowetting. *J. Phys. Chem. C* 114, 14885–14890 (2010).
14. Dickey, M. D. et al. Eutectic Gallium-Indium (EGaIn): A Liquid Metal Alloy for the Formation of Stable Structures in Microchannels at Room Temperature. *Adv. Funct. Mater.* 18, 1097–1104 (2008).
15. Regan, M. J. et al. X-ray study of the oxidation of liquid-gallium surfaces. *Phys. Rev. B Condens. Matter* 55, 10786–10790 (1997).
16. Guha, I. F., Kedzierski, J. & Abedian, B. Low-voltage electrowetting on a lipid bilayer formed on hafnium oxide. *Appl. Phys. Lett.* 99, 24105 (2011).
17. Kedzierski, J. T., Batra, R., Berry, S., Guha, I. & Abedian, B. Validation of the trapped charge model of electrowetting contact angle saturation on lipid bilayers. *J. Appl. Phys.* 114, 24901 (2013).
18. Lomax, D. J. et al. Ultra-low voltage electrowetting using graphite surfaces. *Soft Matter* (2016). doi:10.1039/C6SM01565D

19. Seyrat, E. & Hayes, R. A. Amorphous fluoropolymers as insulators for reversible low-voltage electrowetting. *J. Appl. Phys.* 90, 1383–1386 (2001).
20. Verheijen, H. J. J. & Prins, M. W. J. Reversible Electrowetting and Trapping of Charge: Model and Experiments. *Langmuir* 15, 6616–6620 (1999).
21. Chevalliot, S., Kuiper, S. & Heikenfeld, J. Experimental Validation of the Invariance of Electrowetting Contact Angle Saturation. *J. Adhes. Sci. Technol.* 26, 1909–1930 (2012).
22. Mugele, F. Fundamental challenges in electrowetting: from equilibrium shapes to contact angle saturation and drop dynamics. *Soft Matter* 5, 3377 (2009).
23. Quinn, A., Sedev, R. & Ralston, J. Contact Angle Saturation in Electrowetting. *J. Phys. Chem. B* 109, 6268–6275 (2005).
24. Paneru, M., Priest, C., Sedev, R. & Ralston, J. Static and Dynamic Electrowetting of an Ionic Liquid in a Solid/Liquid/Liquid System. *J. Am. Chem. Soc.* 132, 8301–8308 (2010).
25. Li, F. & Mugele, F. How to make sticky surfaces slippery: Contact angle hysteresis in electrowetting with alternating voltage. *Appl. Phys. Lett.* 92, 244108 (2008).
26. Tan, X., Zhou, Z. & Cheng, M. M.-C. Electrowetting on dielectric experiments using graphene. *Nanotechnology* 23, 375501 (2012).
27. Kedzierski, J. & Berry, S. Engineering the Electrocapillary Behavior of Electrolyte Droplets on Thin Fluoropolymer Films. *Langmuir* 22, 5690–5696 (2006).

Conclusions and Outlook

By applying an electrochemical potential to a gallium-based liquid metal alloy in solution, we have demonstrated a variety of novel features. We have shown dramatic and reversible shape change by tuning the thickness of an anodic oxide layer; we have demonstrated directional control, stable liquid metal fibers, and reconfigurable microfluidic devices. Furthermore, we have utilized this oxidation process to discover a new universality class of fingering instabilities. Finally, we have shown that this metal can serve as the substrate in electrowetting-on-dielectric, allowing for a simple fabrication and electrowetting without an applied potential.

The preceding work has left several lingering questions regarding both the nature of the liquid metal and its oxide. This section discusses the outlook and future work for research involving EGaIn from the work described in this thesis, including possible new research paths and questions that have arisen from these projects. There are both fundamental scientific questions and potential applications.

Many of the pressing questions still remaining from this work revolve around the oxide layer on the surface, under both ambient and anodizing conditions. First and foremost, future work will involve quantifying the interfacial tension between the liquid metal and its oxide under ambient conditions. While it is possible to easily measure the interfacial tension in acid, base, or de-oxygenated solutions with traditional methods, measuring the effective interfacial tension of the liquid metal in ambient air presents a much greater challenge. Most of these methods rely on measuring the equilibrium geometry of a liquid in its environment; however,

in this case, the mechanical stability provided by the oxide allows the metal to be deformed into shapes that do not minimize interfacial energy. Rather than having a single interface between the liquid metal and the environment, EGaIn in ambient air has two: the liquid/oxide interface and the oxide/environment interface. Work from Chapter 2 suggests that the oxide acts as a surfactant, indicating that the interfacial tension between the metal and its oxide is low; we have substantial evidence to back this assertion. However, more research will need to be undertaken to quantify the value of the interfacial tension at this surface.

Further questions remain regarding the oxide layer, particularly its composition and thickness in solution and under anodic potential. While we have provided a crude estimate of the oxide thickness in Chapter 3, based on a simple mathematical model, we have not attempted to directly measure changing thickness as a function of time and voltage. Ascertaining more information about the growing oxide could provide a better understanding of the dynamic forces involved when the liquid metal drop is spreading and forming fingering instabilities. We have considered a variety of techniques that would help us better understand the thickness, structure, and composition, including optical spectroscopy, direct measurement of the change in mass as a function of time and potential through a quartz crystal microbalance, and measuring the dissolution rates of the oxide in various media by measuring the concentration change of gallium and indium in solution. Additionally, through rheological techniques, we may be able to measure the dynamic mechanical properties of the oxide layer under an oxidative potential.

One area that has not been carefully explored is the formation of liquid metal fibers (shown briefly in Chapter 2). These fibers present an interesting topic for characterization, as

they have not been well-studied. Future research could examine the relationship between flow rate, voltage, and capillary diameter of these fibers. Interestingly, these fibers appear to remain stable well-beyond their instability limit, possibly owing to the mechanical effects of the oxide. Thus far, we have not seen drops of the liquid metal break up in a Rayleigh instability, as is observed with Newtonian fluids; we have demonstrated stable wires of over 1 foot in length.

Finally, most of the work from Chapter 4 has focused on characterizing the electrowetting behavior of the liquid metal substrate. However, the field of electrowetting has a vast array of applications, and many of these could benefit from a substrate with as many advantages as EGaIn or gallium. One future direction could focus on utilizing the simple patterning of the metal for functional and biocompatible lab-on-a-chip devices.